Multi-Birefringence Effects in the Diluted Magnetic Semiconductor Cadmium Manganese Telluride: Applications from Microwave to Terahertz

by

Chia-Chu Chen

A dissertation submitted in partial fulfillment
of the requirements for the degree of
Doctor of Philosophy
(Electrical Engineering)
in The University of Michigan
2010

Doctoral Committee:

Adjunct Professor John F Whitaker, Chair
Professor Steven M Yalisove
Assistant Professor Anthony Grbic
Assistant Professor Mona Jarrahi

Acknowledgement

I would like to thank my mentor Dr. John Whitaker for his guidance, inspiration, support, and patience during my time as a graduate student. John allowed me to work independently on a wide range of projects, only a few of which made it into this thesis.

I also wish to extend my thanks to Dr. Tresa Pollack: without her support through the use of her tube furnace, none of my Terahertz work would have been possible. In addition Drs. Steve Yalisove, Anthony Grbic, Mona Jarrahi and Chris Feak, have graciously provided feedback.

I am extremely thankful to my fellow research group members: Matt Crites, J Bianca Jackson and Dong-Joon Lee for lending me their ears, both personally and professionally when I needed it. I also want to thank my colleagues at the Center of Ultrafast and Optical Science: Chuck Divin, James Easter and Tsai-Wei Wu. They helped me throughout the last two years in my graduate studies when I am the only graduate student in my lab.

Last, but not least, I would like to thank my parents, Chih-Wei Lee and Chien-Ta Chen, for your love and encouragement. They always believed in me, even if they didn't understand what I was doing. I would like to thank my wife Tien-Yi for your love, encouragement, and patience through all the long nights, and extended writing. Without your encouragement, I never could have finished.

Contents

List of Figures

Chapter 1
Introduction

1.1 Background

Nondestructive evaluation tools unite physics and engineering in order to extract information about a material, component or an electronic device that would result in design improvement, conservation, or replacement. Nondestructive evaluation is desirable because it can prevent costly or destructive consequences of failure of a material or device of components. The information extracted from nondestructive measurement can provide or evaluate the characteristic of an electronic device, i.e. electromagnetic compatibility, interference, or radiating field strength and direction. In addition, nondestructive evaluation can also play a role in the real-time monitoring or inspection of a system to determine its composition or flaws during manufacture or construction.

Nondestructive evaluation techniques are often chosen depending on the quantity and quality of the data that can be extracted from a measurement, in addition to the financial cost and time required to make the measurement. Localized, or single point, measurements of components of interest can provide specific, often highly quantified details about a material or system. On the other hand, large area measurements may provide fast, highly qualitative, but essential, information. Combining measurement techniques can make up for the limitations of a single method, however the ideal is a single cost-effective measurement system that is versatile and results in multiple kinds of system assessments.

A nondestructive evaluation not only can save the cost for examining a product quality but also can prevent a disaster caused by a system failure. For instance, on February 1, 2003, the space shuttle Columbia disintegrated over Texas during re-entry into the earth's atmosphere. All seven crew members were lost because the thermal protection system, which protects the space shuttle from the heat generated by the atmosphere during re-

entry, was damaged. If a nondestructive evaluation tool had been available to identify flows in the thermal protection system, this tragedy might have been prevented. Such a detection system would also prevent future disasters. In this thesis, terahertz (THz) electromagnetic waves are used to nondestructively evaluate and monitor the health of a thermal protection system.[1] This THz nondestructive evaluation method leads to diagnostics that predict the failure of turbine-blade and gas engine coatings. This would allow thermal protection system replacement to be based on THz assessment rather than on a fixed timetable, thus offering savings for the government, airlines, and other industries.

Noninvasive measurements also hold the promise of providing valuable diagnostic test and evaluation feedback in the microwave electromagnetic wave region, for example, for measurements of electric and magnetic signals on the basis of near field-mapping over the internal nodes of microwave devices. Given the growing use of microwave devices in both the military and civilian realm, it is becoming increasingly important to have detailed information on the characteristics and potential effects of local electromagnetic radiation. Such information can shed light on a range of issues such as electromagnetic interference in a microwave system. While the far-field pattern is of primary concern, near-field region measurements are particularly useful in testing for electromagnetic compatibility and interference in microwave integrated circuits. This electromagnetic interference information can lead to the diagnosis of failures or calibration of the compact circuits, military and civilian applications. [2, 3] Questions such as those surrounding the impact of mobile phone radiation on the brain can also be addressed by measuring the near-field specific absorption rate, resolving concerns of high-power microwave exposure on humans.[4]

Among the demonstrated noninvasive probing techniques, electro-optic (EO) and magneto-optic (MO) sensing offer a high degree of flexibility, while exhibiting minimal intrusiveness, since they do not require the electrical conductors to be incorporated as part of their probe structure.[5, 6] Although EO sensing is reasonably well-developed as a diagnostic for electric fields and voltages, MO sensing has somewhat lagged as a means to extract magnetic-field and current information.[7] This is because magnetic fields and

current information can usually be derived from the measured electric field and Maxwell equations. However, magnetic fields and current information cannot be derived from Maxwell equations in the near field region because the propagation direction, electric field and magnetic field are not orthogonal to each other. In addition, due to the demonstration of a variety of high-frequency measurements, MO field extraction is now being viewed as a complement to EO sensing and thus has been attracting increased attention.[8, 9]

EO and MO sensing techniques are similar in that they require an anisotropic crystal to detect the field. When an external electric or magnetic field is applied to this anisotropic crystal, the refractive index of the crystal changes according to the strength and direction of the field. Anisotropic crystals that have different indices of refraction along different crystal axes are known as birefringent crystals. When ultrashort probe pulses pass through a birefrigent crystal, changes in the polarization of the laser pulses that result from differences in the refractive index will lead to changes in optical power after an analyzing polarizer. When the arrival time of the laser pulse is varied to achieve sequential sampling of a repetitive signal, a full waveform of the applied electric or magnetic field can then be obtained. For each relative time delay setting, the signal obtained can be averaged over many pulses, so that noise is averaged out and reasonably high sensitivity is achieved.[10, 11]

Although the sensing techniques are the same, the specific anisotropic crystals used as the EO or MO sensing medium differ. The most commonly used EO crystals are lithium tantalate ($LiTaO_3$) and Zinc Telluride (ZnTe) at a probe pulse wavelength of 800nm. These crystals are used because $LiTaO_3$ has a very large EO coefficient and ZnTe has the longest coherence length. Among MO crystals, terbium gallium garnet (TGG) is the most commonly used crystal because of its large Verdet constant.[8, 12, 13] However, none of these crystals can be used for both EO and MO sensing because they do not simultaneously possess linear and circular birefringence. To overcome this single birefringence issue, the research presented in this thesis uses cadmium manganese telluride (CMT) for both EO and MO sensing. This crystal is well suited because of its multiple birefringence characteristics, allowing both electric and magnetic field to be

obtained. Utilizing this characteristic, three-dimensional distribution of electric and magnetic field components can be measured. Furthermore, when CMT is used, the Poynting vector of a microwave device can be subsequently mapped out without the need for transformational calculation. In addition to measuring electromagnetic waves in the microwave region, CMT is also applied as an EO crystal in the THz region because of its broad measurement bandwidth.

1.2 Electro-optic sampling

One relatively new technique for the near field measurement of electronic devices is electro-optic sampling (EOS). The advantages of using EOS are its wide bandwidth and low invasiveness, as well as its fine temporal and spatial resolution.[14] The EOS technique uses the birefringence induced in a noncentrosymmetric crystal by an applied electric field via the Pockels effect to transfer an electromagnetic wave signal to an optical beam. The applied electric field changes the dimension and orientation of the index ellipsoid of the sensing crystal. Taking a CMT crystal as an example, the equation of the index ellipsoid given the applied electric field components, E_x, E_y and E_z, can be written as

$$\frac{x^2+y^2+z^2}{n^2} + 2r_{41}\left(yzE_z + xzE_y + xyE_z\right) = 1 \quad (1)$$

where x, y and z are the unperturbed principal axes of the laboratory coordinate system, n is the original refractive index of CMT before application of the field, and the r_{41} represents the CMT EO coefficients.[15, 16] The change in index ellipsoid causes the sensing crystal to become birefringent. The new refractive indices with an applied electric field along the z direction, for instance, will be

$$n_{x'} = n - \frac{1}{2}n^3 r_{41} E \quad (2)$$

$$n_{y'} = n + \frac{1}{2}n^3 r_{41} E \quad (3)$$

$$n_{z'} = n \quad (4)$$

where (x', y', z') are new principal coordinates. The sampling optical beam can be considered to be split into two orthogonal components within the birefringent crystal. If the optical beam is propagating along the y' direction, the orthogonal polarization components are parallel to the x' and z' direction of the EO crystal. The polarization components traveling along the major axes experience different indices of refraction and retardation in the birefringent crystal, thus causing a phase shift between the two. Consequently, this phase retardation caused by the birefringence leads to a change in the polarization status of the optical beam after propagating through the crystal.

In general, the phase retardation, Γ, can be expressed as

$$\Gamma = \frac{2\pi}{\lambda}(n_e - n_o)L \tag{5}$$

where λ is the wavelength of the probe pulse, n_e and n_o are the refractive indices for the polarization perpendicular (ordinary) and parallel (extraordinary) to the birefringent axis, and L is the distance that the probe beam travels inside the crystal. If CMT is the sensing crystal and the optical beam propagates along the y' direction, the phase retardation of an applied electric field along the z direction is

$$\Gamma = \frac{2\pi}{\lambda}(n_{z'} - n_{x'})L \tag{6}$$

$$\Gamma = \frac{\pi}{\lambda}n^3 r_{41} EL \tag{7}$$

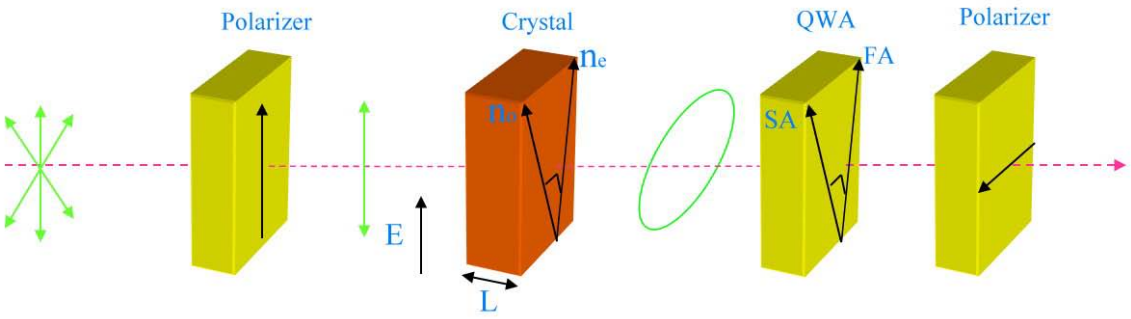

Figure 1 A typical electro-optic amplitude modulator. FA and SA represent the fast and slow axis of the quarter wave plate, QWA, respectively.

In order to analyze the applied electric field strength, the sensing crystal is placed between two crossed polarizers and a quarterwave plate as shown in Figure 1. This optical setup converts the polarization rotation of the optical beam, i.e. phase modulation, into a change in intensity. Following the Jones matrix calculation, the optical electric field of the transmitted probe beam, E', is obtained as follows:

$$\mathrm{E}' = \begin{bmatrix} 1 & 0 \\ 0 & 0 \end{bmatrix} \frac{1}{\sqrt{2}} \begin{bmatrix} 1 & -i \\ -i & 1 \end{bmatrix} \begin{bmatrix} \cos\frac{\Gamma}{2} & -i\sin\frac{\Gamma}{2} \\ -i\sin\frac{\Gamma}{2} & \cos\frac{\Gamma}{2} \end{bmatrix} \begin{bmatrix} 0 \\ 1 \end{bmatrix} \tag{8}$$

$$\mathrm{E}' = \frac{-i}{\sqrt{2}} \begin{bmatrix} \sin\left(\frac{\Gamma}{2}\right) + \cos\left(\frac{\Gamma}{2}\right) \\ 0 \end{bmatrix} \tag{9}$$

Each matrix in Equation 8 represents one optical element in Figure 1. Using the result in Equation 9, the transmitted light intensity, I, can be expressed as

$$\mathrm{I} = \frac{\mathrm{I}_0}{2}(1 + \sin\Gamma) \tag{10}$$

Due to the trigonometric identities, Equation 10 becomes

$$\mathrm{I} = \mathrm{I}_0 \sin^2\left(\frac{\pi}{4} + \frac{\Gamma}{2}\right) \tag{11}$$

where I_0 is the incident probe beam intensity.[17]

Figure 2 depicts how a sinusoidal input waveform induces a change in output intensity according to Equation 11. It is clear that if a quarter wave plate is not used, the transmission cannot operate at the linear region, i.e. the operation point will be at the zero transmission causing the intensity variation to be distorted. In addition, the modulation depth of the transmitted intensity depends on the phase retardation; therefore, n^3r_{41} is usually defined as the figure of merit in an EO crystal in $\bar{4}3m$ symmetry-group. In general, crystals with a good figure of merit can approach a dynamic range up to 100 dB and allow an intensity change on the order of 10^{-6} to be detected.

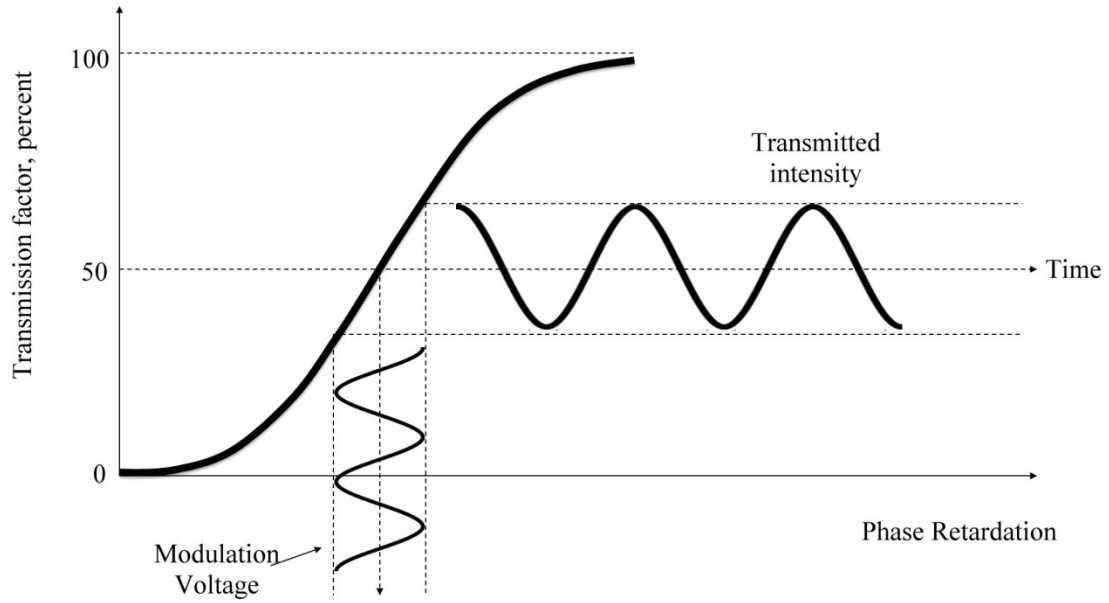

Figure 2 Transmission factor of a cross-polarized electro-optical modulator as a function of applied voltage.

1.3 Magneto-optic sampling

The noninvasive MO-sampling (MOS) technique can locally probe the transient magnetic field at different positions on the device under test (DUT), and the field information can be used to calculate the accurate value of the current.[9] The principle of MOS is similar to EOS. Specifically, the applied magnetic field perturbs the spin system of the crystal causing waves to be decomposed into two circularly polarized rays that propagate at different speeds, a property known as circular birefringence. The rays recombine upon emergence from the MO crystal. However owing to the difference in propagation speed, a linearly polarized probe beam passing through the crystal will experience a small rotation in its plane of polarization. This is called the Faraday effect and the rotation angle, θ_F, can be expressed as

$$\theta_F = \mathrm{VBL} \tag{12}$$

where V is the Verdet constant, B is the magnetic flux density applied in the direction of light propagation and L is the length of the path on which the probe beam and magnetic field interact. One of the best examples employing Faraday effect is the Faraday isolator

which is used to protect optical systems from retro-reflections. This is achieved by placing the MO crystal in a strong dc magnetic field, and hence the optical beam passing through the crystal will rotate by an angle of 45 degree. If a linear polarizer is attached in the front of the crystal, any backward reflection will be blocked since the reflected light will rotate another 45 degree and cause the linear polarization to be perpendicular to the transmission axis of the polarizer.

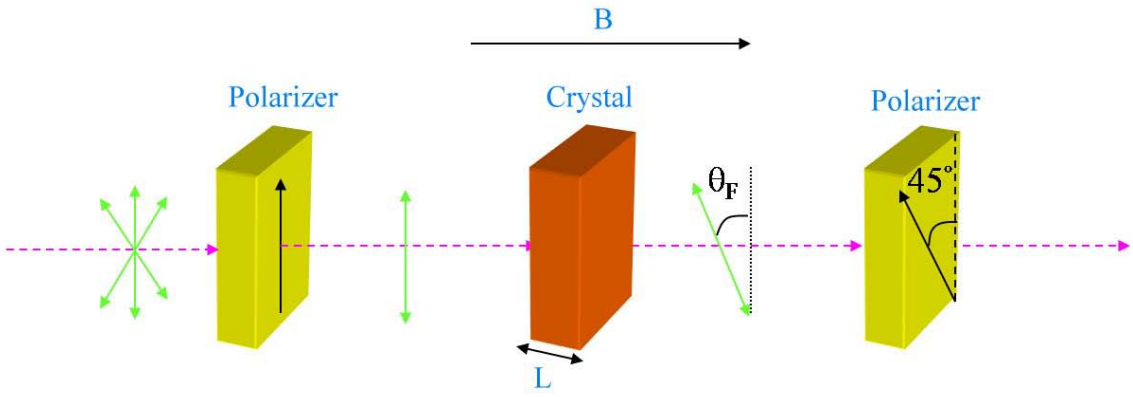

Figure 3 A typical magneto-optic amplitude modulator.

Unlike the optical setup in EOS, the MOS technique places the MO crystal between two polarizers, which have transmission axes at angles of 45 degrees relative to each other, as shown in Figure 3. This configuration converts the phase modulation to an intensity modulation. Following the Jones matrix calculation, the electric field of the transmitted probe beam is obtained as follows:

$$E' = \frac{1}{2}\begin{bmatrix}1 & 1\\ 1 & 1\end{bmatrix}\begin{bmatrix}\cos\theta_F & -\sin\theta_F\\ \sin\theta_F & \cos\theta_F\end{bmatrix}\begin{bmatrix}0\\ 1\end{bmatrix} \tag{13}$$

$$E' = \frac{1}{2}\begin{bmatrix}\cos\theta_F - \sin\theta_F\\ \cos\theta_F - \sin\theta_F\end{bmatrix} \tag{14}$$

The transmitted probe beam intensity is expressed as

$$I(\theta_F) = \frac{I_0}{2}(1 - \sin 2\theta_F) \tag{15}$$

Due to the trigonometric identities, Equation 15 becomes

$$I(\theta_F) = I_0 \cos^2(45 + \theta_F) \tag{16}$$

Equation 16 is also called Malus' law. Similar to the EOS technique, the transmitted intensity in Equation 16 is modulated at a 50 percent transmission point, which is the linear region on the $\cos^2$ curve, as shown in Figure 4.

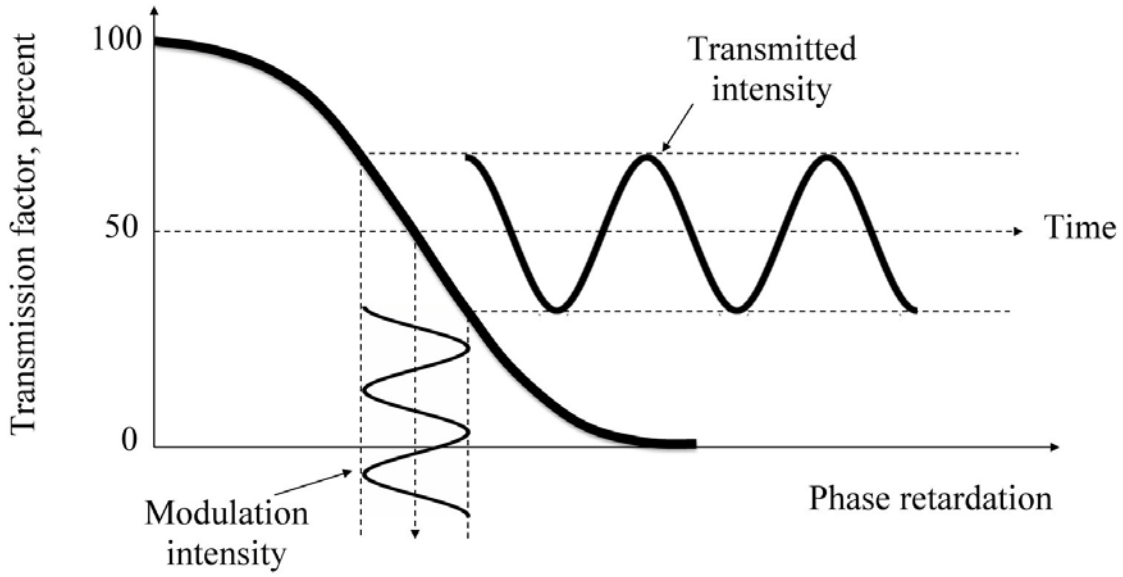

Figure 4 Transmission factor of a cross polarized magneto-optical modulator as a function of applied voltage.

Using an MO crystal in the EOS optical setup, the electric field of the transmitted probe beam is obtained as follows:

$$E' = \begin{bmatrix} 1 & 0 \\ 0 & 0 \end{bmatrix} \frac{1}{\sqrt{2}} \begin{bmatrix} 1 & -i \\ -i & 1 \end{bmatrix} \begin{bmatrix} \cos\theta_F & -\sin\theta_F \\ \sin\theta_F & \cos\theta_F \end{bmatrix} \begin{bmatrix} 0 \\ 1 \end{bmatrix} \tag{16}$$

$$E' = \frac{-i}{2} \begin{bmatrix} \cos\theta_F + i\sin\theta_F \\ 0 \end{bmatrix} \tag{17}$$

The transmitted probe beam intensity is expressed as

$$I(\theta_F) = I_0 \left(\frac{1}{2} - \sin^2\theta_F \right) \tag{18}$$

According to Equation 18, the transmitted intensity is modulated at a 0 percent transmission point, as Figure 2 shows. However, because the rotation angle θ_F of the Faraday effect is usually less than 1 degree, using an MO crystal in an EOS setup will result in an extremely small and distorted signal. Therefore, polarization control is the most important factor in the EOS or MOS technique.

1.4 Electro-optic and magneto-optic sampling system

Section 1.2 and 1.3 briefly introduced the mechanisms of the EOS and MOS techniques. This section discusses the two most commonly used sampling systems for these techniques. The first system is harmonic mixing, which extracts the amplitude and phase of the radio frequency (RF) signal by synchronizing a single laser pulse train with a continuous wave (cw) RF signal. Consequently, this system can map out the characteristics of an electric or magnetic field pattern in space. The second is a time-domain pump-probe sampling system, which acquires a time-domain transient waveform by varying the time delay between the excitation and probe laser pulse trains. One advantage of using this time-domain sampling system is that detection is coherent and the signal is proportional to the true electric field. Thus, both amplitude and phase information of the signal in the time-domain are preserved. These two different sampling systems are described in the following subsection.

1.4.1 Harmonic Mixing

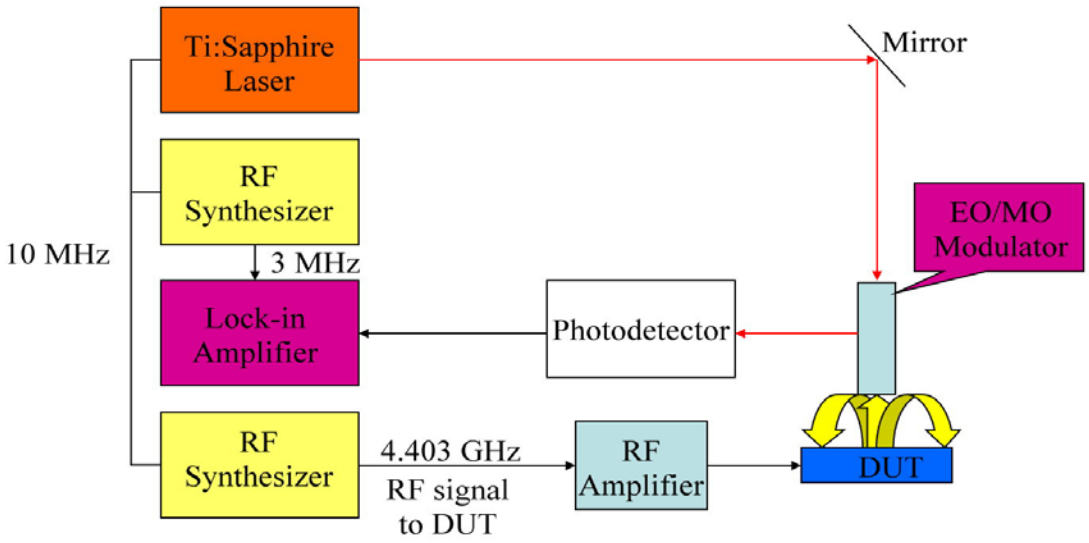

Figure 5 Electro-optic field-mapping system schematic.

As shown in Figure 5, harmonic-mixing is basically a synchronous sampling, where the DUT is driven by a radio-frequency (RF) or microwave CW synthesizer. The 80 MHz repetition rate of the laser is divided down to create a 10 MHz signal that can typically be used as a reference by two RF synthesizers to synchronize the phases of the optical pulse and electrical signals. One of these synthesizers provides an input microwave signal to the device under test (DUT), while the other supplies a constant-phase reference signal, at an intermediate frequency Δf, to a lock-in amplifier that will receive the photodiode output signal corresponding to the EO modulation. The detailed optical setup for either an EO or MO modulator was shown in the previous section in Figure 1 and 3.

The harmonic-mixing technique utilizes higher-order harmonics of the repetition rate in a pulsed laser as a local oscillator sideband on the optical carrier to mix with the RF signal from the DUT in the nonlinear EO or MO crystal.[7] In other words, the input microwave signal, RF_{DUT}, is set at an integer multiple, *N*, of the laser repetition frequency plus the intermediate frequency as Equation 19 shows.

$$RF_{DUT} = (N \times 80) + \Delta f \tag{19}$$

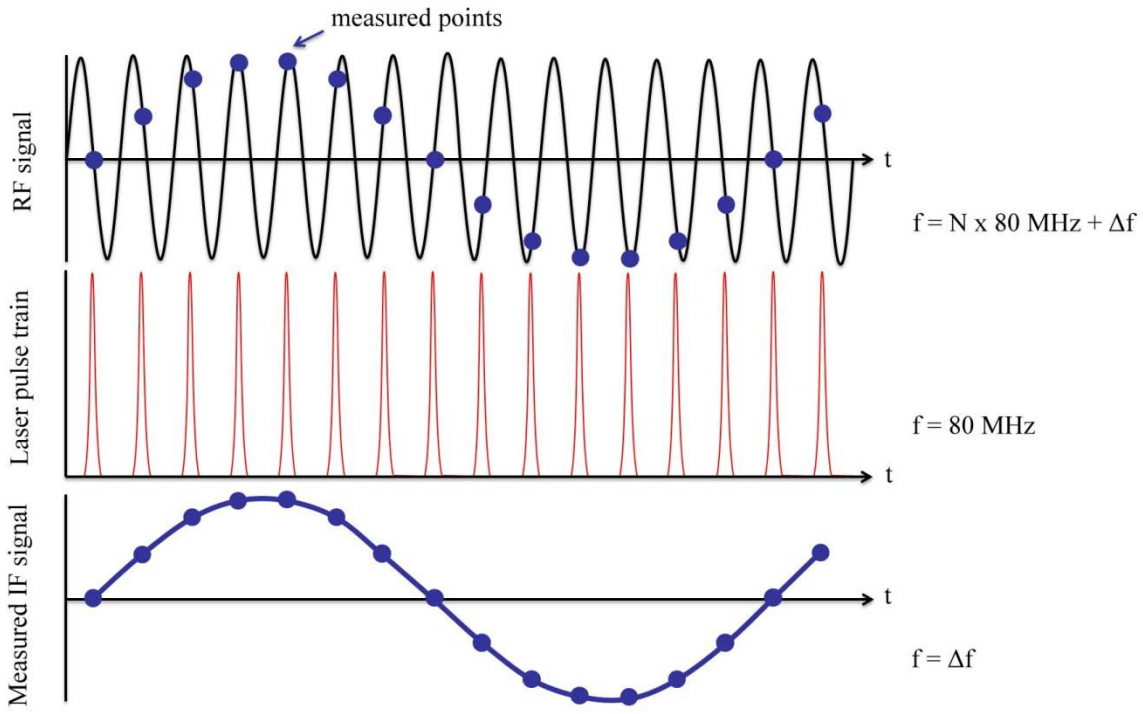

Figure 6 Harmonic mixing concept for the electro-optic detection of the amplitude and phase of a cw RF signal. The laser pulse train and its harmonics are used like a local

oscillator to down-convert a high-frequency electrical signal to a low-frequency IF signal that can be measured in a lock-in amplifier.

Figure 6 displays the laser pulse train, the RF_{DUT} signal, and the measured intermediate frequency signal as a function of time. Since the pulse repetition frequency of the laser is much smaller than the operating frequency of the microwave or millimeter wave DUT, there always exists an integer multiple of the repetition rate that is close to the RF_{DUT}. If the RF_{DUT} is exactly a multiple of the laser repetition frequency, i.e., the output does not possess any intermediate frequency (IF), then the laser pulses will always sample the exact same position on the RF signal. In this case, the measured signal would be a uniform value with respect to time. However, with the IF, each laser pulse detects a slightly different position on the RF signal due to the addition of the slight time delay from the frequency difference. Although the IF can be selected independently of the RF_{DUT}, an odd-number multiple of the IF is usually intentionally selected. This is because most electronic equipment is operated by an even number multiple of the frequency power source (60 Hz), and thus the possibility of noise from the AC line voltage can be minimized.

With the cw RF signal from the DUT synchronized to the laser pulses, both the amplitude and phase of the RF signal from the DUT can be captured by the lock-in amplifier. The lock-in amplifier is not only able to detect high frequency RF_{DUT} signal information, which is otherwise out of its detection range, by mixing it down to the intermediate frequency level, but when the laser pulses and sensing crystal detect the field at different spatial locations, the lock-in also allows accurate sensing of the electric field as its phase changes. This is because the lock-in amplifier is able to compare these phases with the fixed phase of the reference signal, 10 MHz. Because many microwave devices operate under CW conditions, in this thesis, the harmonic-mixing technique is used for all the RF field-mapping experiments.

1.4.2 Time-domain pump-probe sampling system

The schematic of an EOS sampling system is shown in Figure 7. The laser pulse train is first divided into two beams using an appropriate beam splitter. The pump beam is represented by the red line in Figure 7. When the gap of the photoconductive switch is

illuminated, a very short duration transients is generated by the ultrafast pulses. This transient changes the refractive index of the EO crystal, and hence the polarization of the linear polarized probe beam, the blue line in Figure 7, changes accordingly. The probe beam is reflected back from the bottom of the EO crystal due to the high-reflection coating. After passing through the quarterwave plate, the probe beam is split by the Wollaston prism into two orthogonal linear polarizations.

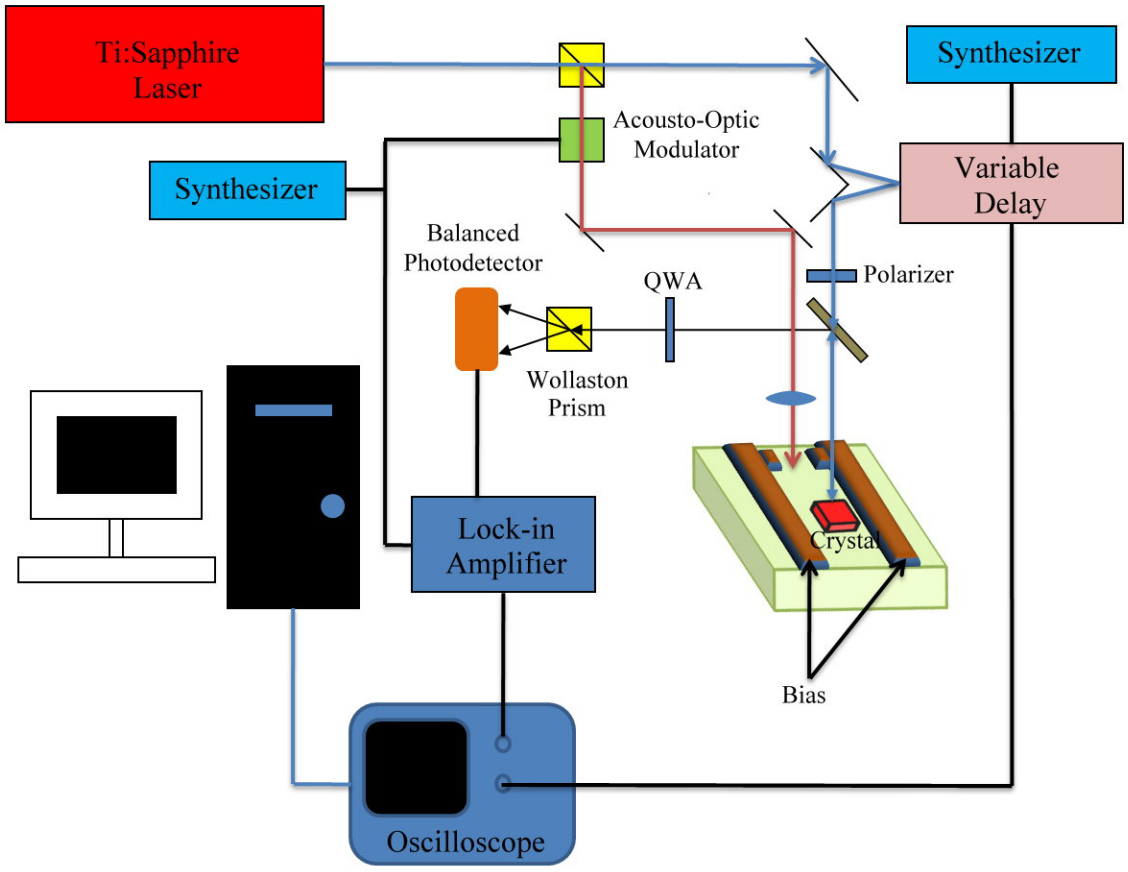

Figure 7 Schematic of a time-domain electro-optic sampling system.

The probe optical beam, split from the pump beam, passes through a variable delay so that the electrical signal generated by the photoconductive switch can be "swept through" the optical sampling pulses. The delay rail, usually a stepper motor, stops periodically at each of many positions to allow the probe beam to dwell at constant intervals in time along the electric waveform. The signals from the balanced photodetector, usually p-i-n photodiodes, at the output of the Wollaston prism can be integrated by the detection electronics at each of the delay-rail positions to improve the signal-to noise ratio. The

output of the diodes, ($I_o/2+\Delta_{intensity}$+noise) and ($I_o/2-\Delta_{intensity}$+noise), are subtracted in the differential amplifier to give $2\Delta_{intensity}$, further improving the signal-to-noise ratio by 3dB. Note that the $\Delta_{intensity}$ is the change in intensity resulting from the birefringence change in the EO crystal as shown in Equation 11.

The acousto-optic modulator in Figure 7 is placed in the pump beam path in order for the probe beam leaving the EO crystal to become modulated. The lock-in amplifier, which detects signals only at this modulation frequency, is used to gain further immunity from the 1/f noise present in the system and to integrate the signal from the slow detectors at each interval that the acousto-optic modulator is switched on. Finally, the output from the lock-in amplifier is sent to the oscilloscope, where multiple traces of the sampled waveform can be averaged together and plot the waveform in the time-domain on the screen by using the delay time from the variable delay rail as the reference time scale.

1.5 Dissertation outline

In Chapter 2, the multiple birefringence characteristics of CMT are analyzed on the basis of the Maxwell equations. The analyzed results combined with the Jones matrix calculation can be used to derive the power transfer function when a CMT crystal is employed as either an EO or MO sensing medium. Both theory and experimental results demonstrate that a diluted-magnetic-semiconductor CMT crystal exhibits both Faraday rotation and electric-field-induced linear birefringence. Utilizing this characteristic, a single probe that is capable of sensing both electric and magnetic fields independently has been developed. A higher field sensitivity and greater accuracy are observed for the CMT crystal when both compared to a lithium tantalate electro-optic crystal and terbium gallium garnet magneto-optic crystal. The linear electro-optic coefficient, r_{41} for CMT has been calculated from electric-field measurements to be 3.5 ± 0.2 pm/V.

In Chapter 3, the ability to measure the electric or magnetic field components is exploited to develop a Poynting vector sensor that does not require any further transformational calculation or physical information of the device. A map of the microwave Poynting vector along a 50-Ω microstrip was experimentally determined. The open termination microstrip shows no energy flow, according to both amplitude and

phase information, whereas the matched-load microstrip shows consistent energy flow along the microstrip transmission line. These results demonstrate that the Poynting vector can be measured with the components of an electric and a magnetic field by utilizing a single <110> CMT crystal that exhibits both the Pockels and Faraday effects.

Chapter 4 shifts the focus from the microwave to terahertz (THz) electromagnetic-wave region. Background on generating and detecting THz through a photoconductive switch or through an EO crystal is given at the beginning of the chapter. Next, a THz time-domain reflectometry system is built by applying a photoconductive switch as the THz source and CMT as an EO sensing crystal. The surface defects of a thermal barrier coating beyond the diffraction limit are investigated and identified by using this THz time-domain reflectometry system. In addition, the current applications of applying THz as a nondestructive evaluation tool are also discussed.

In Chapter 5, terahertz time-domain reflectometry is used to monitor the progress of a thermally grown oxide layer and stress-induced, air-filled voids at the interface of an Yttria-stabilized-zirconia ceramic thermal-barrier coating and a metal surface. The thicknesses of these internal layers, observed in scanning-electron-microscope images to increase with thermal-exposure time, have been resolved – even if on the order of only a few micrometers – by distinguishing not only increased delays in the arrival times of the terahertz pulses reflected from this multilayer structure, but also changes in the width and shape of the pulses. These unique features can be used to predict the lifetime of thermal-barrier coatings and to indicate or provide a warning of imminent spallation conditions. The THz pulse delay time of the experimental results are also confirmed through Fresnel-reflection time-domain simulations.

Finally, chapter 6 summarizes the main results of the preceding chapters as well as present ideas for systematic improvements and future experiments.

Chapter 2
Cadmium Manganese Telluride with Multiple Birefringence

In this chapter, a <110>-oriented cadmium manganese telluride (CMT) crystal was investigated as a sensor of the amplitudes and phases of the vector components of both the electric and magnetic fields in the microwave range. The multiple birefringence characteristics of CMT were carefully examined both theoretically and experimentally, it has been demonstrated that this crystal can be used for both EO or MO sensing by controlling the polarization of the probe beam.

2.1 Diluted magnetic semiconductor

CMT is a diluted magnetic semiconductor that is created from the II-VI compound, cadmium telluride (CdTe), by substituting the original cations, Te for the transition metal ions, manganese (Mn), A diluted magnetic semiconductor may be considered as containing two interacting subsystems. The first of these is the system of delocalized conduction and valence band electrons. The second is the random, diluted system of localized magnetic moments associated with the magnetic atoms. The fact that both the structure and the electronic properties of the host crystal, CdTe, are well known means that CdTe is perfect for studying the basic mechanisms of the magnetic interactions coupling the spins of the band carriers and the localized spins of the CMT crystal magnetic ions.[18]

For semiconductor materials such as CdTe, spin-orbit splitting is an essential characteristic of the electronic band structure. This characteristic arises from the interaction of the intrinsic magnetic moment of the electron spin with the magnetic field generated by electron motion. The magnitude of spin-orbit splitting is known to affect the location of the lowest hole levels in the valence band of a crystal. In a cubic crystal such as a zinc-blende structure, the three valence bands (J, M_J) = (3/2, ±3/2), (3/2, ±1/2), and (1/2, ±1/2) are referred to as the heavy-hole, light-hole, and split-off hole subbands,

respectively (where J is angular momentum and M_J is the energy level). The doubly degenerate heavy-hole, light-hole, and a lower nondegenerate split-off hole-band are separated by the spin-orbit splitting. In other words, when an external field is applied to a cubic crystal, the field splits the degenerate valence band, J = 3/2, into two bands, one with $M_J = \pm 3/2$ and the other with $M_J = \pm 1/2$. [19, 20] Optical transitions are made from these bands to a conduction band $(J, M_J) = (1/2, \pm 1/2)$. Transitions from $M_J = \pm 1/2$ are allowed for light polarized by the electric vector both parallel and perpendicular to the applied field direction, while transitions from the $M_J = \pm 3/2$ valence band can occur only for light polarized by the electric vector perpendicular to the field. Therefore, it is obvious that the splitting of the valence band under the applied external field would lead to the linear birefringence of the crystal. As described in section 1.2, the induced linear birefringence will yield EO effects, such as Pockels effect, when the optical probe beam passes through the EO crystal under an applied external field.

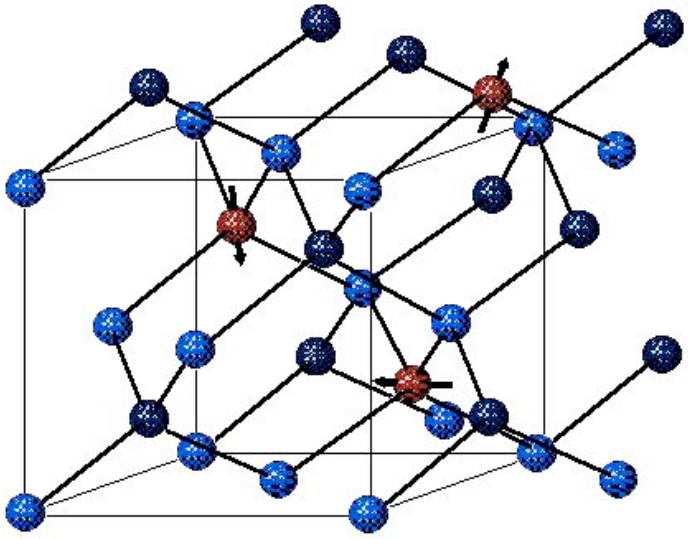

Figure 8 Zinc-blende structure of CMT. The atom of cadmium, telluride and manganese are represented by blue, dark blue, and red, respectively. The arrow on manganese denotes the dipole direction.

CMT shares this zinc-blende structure with its host semiconductor CdTe as shown in Figure 8. The coupling between the localized moments results in the existence of various magnetic phases, such as paramagnets, spin glasses and antiferromagnets. For example,

at room temperature, CMT is paramagnetic. Constituent atoms or molecules of paramagnetic materials have permanent magnetic dipoles, even in the absence of an external applied field. This generally occurs due to the spin of unpaired electrons in the electron orbitals. In paramagnetic materials, the dipoles do not interact with one another without an external field and are randomly oriented because of thermal agitation, resulting in zero net magnetic moment. As Figure 8 shows, the manganese substitutes some of the telluride atoms, and shows a zero net magnetic moment without an applied magnetic field. However, with an external applied magnetic field, the dipoles will tend to align with the field, resulting in a net magnetic moment in the direction of the applied field. This is because an anomalously strong exchange interaction exists between the delocalized band carrier states of sp-band electrons and the localized d electrons of Mn^{2+}.[21, 22] In addition, this net magnetic moment will create a large MO effect, such as the Faraday effect, when the optical probe beam passes through the MO crystal under an applied external field.

Another MO effect is magnetic circular dichroism (MCD) which works as the most powerful tool for detecting s,p-d exchange interactions in diluted magnetic semiconductors. MCD can be used to detect the difference in optical absorption or reflection for left and right circularly polarized light caused by Zeeman splitting.[23] Since the Zeeman splitting is strongly enhanced by the s,p-d exchange interaction, the MCD signal of CMT is much more pronounced than the host semiconductor CdTe.

In summary, the Pockels effect is an electric-field induced, linear birefringence, and the Faraday effect relies on a magnetic-field induced, circular birefringence. The Pockels and Faraday effects are the two physical phenomena used to capture information on RF electric and magnetic fields, respectively, during EO and MO sensing. In this chapter, CMT is employed alternately as an EO and an MO sensor while maintaining an identical geometrical relationship between the crystal, optical probe beam, and field source. That is, as a cubic crystal with zinc-blende structure like its host crystal CdTe, CMT exhibits the Pockels effect, allowing a linear birefringence to be induced on an appropriately polarized input optical beam. As a diluted magnetic semiconductor with a strong exchange interaction between the d spins of its manganese ions and its electrons, a

circular birefringence can also be induced on an optical beam due to relatively strong Zeeman splitting caused by a small applied magnetic field.[24, 25]

2.2 Power transfer function of electro-optic and magneto-optic sensing

Section 2.1 introduces that the CMT crystal possesses both the Pockels and Faraday effects. In order to utilize these two effects independently, this section focuses on finding the 2x2 Jones matrix to represent the CMT crystal, and then uses this matrix to develop the power transfer function with a proper arrangement of polarizers and waveplates, allowing one to distinguish between the two nonlinear optical effects.

To find the Jones matrix to represent a CMT crystal, the dielectric constant, ε, of CMT should first be obtained. This is because the electromagnetic wave propagation properties of any medium can always be described in terms of an effective dielectric constant.[26] Following this argument, the dielectric tensor **[ε]** of any crystal perturbed by multiple physical effects, such as an electromagnetic field, current, voltage, or pressure can be expressed in terms of these effects. For a given complex dielectric tensor, the displacement vector D in an anisotropic medium possessing both linear birefringence and circular birefringence is related to the electric field vector E as

$$D = [\varepsilon]E \tag{20}$$

where

$$[\varepsilon] = [\varepsilon'] + i\varepsilon_{00}[G] \tag{21}$$

Here ε_{00} is the permittivity of the vacuum, [ε'] is the dielectric tensor with no induced circular birefringence or optical activity, and [G] is the gyration tensor expressed by a vector product G x E **(G,** gyration vector). [27]

Using x, y, and z as the laboratory system, the dielectric tensor of an unperturbed crystal can be expressed as

$$\begin{bmatrix} \varepsilon_x & 0 & 0 \\ 0 & \varepsilon_y & 0 \\ 0 & 0 & \varepsilon_z \end{bmatrix} \tag{22}$$

where these three dielectric axes of the crystal corresponding to x, y, and z are called the principal axes, X, Y, and Z, of the crystal. If the optical beam propagation is along the z axis, which coincides with the principal axis Z of the crystal, it usually exists an angle θ_0 between the x lab axis and X principal axes. This angle θ_0 is defined by the x axis in the counterclockwise direction from the X axis and is in the range between 0 and 180 degree. In this case the new dielectric tensor becomes

$$[\varepsilon_0] = A_0 \begin{bmatrix} \varepsilon_x & 0 & 0 \\ 0 & \varepsilon_y & 0 \\ 0 & 0 & \varepsilon_z \end{bmatrix} A_0^{-1} \tag{23}$$

$$[\varepsilon_0] = \begin{bmatrix} \varepsilon_x \cos^2\theta_0 + \varepsilon_y \sin^2\theta_0 & \frac{(\varepsilon_y - \varepsilon_x)}{2} \sin^2\theta_0 & 0 \\ \frac{(\varepsilon_y - \varepsilon_x)}{2} \sin^2\theta_0 & \varepsilon_x \cos^2\theta_0 + \varepsilon_y \sin^2\theta_0 & 0 \\ 0 & 0 & \varepsilon_z \end{bmatrix} \tag{24}$$

where A_0 is a coordinate rotation matrix and is given by

$$[A_0] = \begin{bmatrix} \cos\theta_0 & \sin\theta_0 & 0 \\ -\sin\theta_0 & \cos\theta_0 & 0 \\ 0 & 0 & 1 \end{bmatrix} \tag{25}$$

When a small external electric or magnetic field perturbation is applied to a CMT crystal, the perturbed dielectric constant tensor is often expressed as the sum of the unperturbed term $[\varepsilon_0]$ and the perturbation term $[\Delta\varepsilon]$. $[\Delta\varepsilon]$ can be split into two terms, one due to linear birefringence and the other due to circular birefringence.[28] The perturbed dielectric tensor can be written as

$$[\varepsilon] = [\varepsilon_0] + [\Delta\varepsilon_l] + [\Delta\varepsilon_c] \tag{26}$$

The perturbation term from the induced linear birefringence, $[\Delta\varepsilon_l]$, is given by

$$[\Delta\varepsilon_l] = A_n \begin{bmatrix} \frac{\Delta\varepsilon_l}{2} & 0 & 0 \\ 0 & -\frac{\Delta\varepsilon_l}{2} & 0 \\ 0 & 0 & 0 \end{bmatrix} A_n^{-1} \tag{27}$$

where

$$[A_n] = \begin{bmatrix} \cos\theta_n & \sin\theta_n & 0 \\ -\sin\theta_n & \cos\theta_n & 0 \\ 0 & 0 & 1 \end{bmatrix} \tag{28}$$

Giving

$$[\Delta\varepsilon_l] = \begin{bmatrix} \frac{\Delta\varepsilon_l}{2}\cos 2\theta_n & -\frac{\Delta\varepsilon_l}{2}\sin 2\theta_n & 0 \\ -\frac{\Delta\varepsilon_l}{2}\sin 2\theta_n & -\frac{\Delta\varepsilon_l}{2}\cos 2\theta_n & 0 \\ 0 & 0 & 0 \end{bmatrix} \tag{29}$$

where θ_n is the angle between the x axis and the slow axis of the linear birefringence and

$$\Delta\varepsilon_l = \frac{2\Gamma\varepsilon_0}{k_0 L n_0} \tag{30}$$

Substituting Equation 7 into 30,

$$\Delta\varepsilon_l = 2\varepsilon_0 n_0^2 r_{41} E \tag{31}$$

Similarly, the perturbation term from the induced circular birefringence, $[\Delta\varepsilon_c]$, is given by

$$[\Delta\varepsilon_c] = \begin{bmatrix} 0 & \Delta\varepsilon_c & 0 \\ -\Delta\varepsilon_c & 0 & 0 \\ 0 & 0 & 0 \end{bmatrix} \tag{32}$$

where $\Delta\varepsilon_c$ is

$$\Delta\varepsilon_c = \frac{2i\theta_F\varepsilon_0}{k_0 L n_0} = \frac{2iVB\varepsilon_0}{k_0 n_0} \tag{33}$$

Based on the Equations 29 and 32, the perturbed dielectric tensor of CMT can be expressed as

$$[\varepsilon] = \begin{bmatrix} \varepsilon_{xx} & \varepsilon_{xy} & 0 \\ \varepsilon_{yx} & \varepsilon_{yy} & 0 \\ 0 & 0 & \varepsilon_{zz} \end{bmatrix} \tag{34}$$

where

$$\varepsilon_{xx} = \varepsilon_x \cos^2\theta_0 + \varepsilon_y \sin^2\theta_0 + \frac{\Delta\varepsilon_l}{2}\cos 2\theta_n \tag{35}$$

$$\varepsilon_{yy} = \varepsilon_x \cos^2\theta_0 + \varepsilon_y \sin^2\theta_0 - \frac{\Delta\varepsilon_l}{2}\cos 2\theta_n \tag{36}$$

$$\varepsilon_{xy} = (\varepsilon_y - \varepsilon_x)\cos\theta_0 \sin\theta_0 - \frac{\Delta\varepsilon_l}{2}\sin 2\theta_n + \Delta\varepsilon_c = \varepsilon_{yx}^* \tag{37}$$

Assuming an electromagnetic plane wave propagates along the z axis through the CMT crystal, where the principal axes Z and X of CMT are at angles 0 and Θ degrees with respect to the fixed laboratory axes z and x, respectively, the derived dielectric tensor and Maxwell equations can be used to express the wave equation as

$$\nabla \times \nabla \times E + \omega^2 \mu[\varepsilon]E = 0 \tag{38}$$

where E is the electric field, and with the arbitrary amplitude E_0, E can be expressed as

$$E = E_0 e^{i(\omega t - kz)} \tag{39}$$

Substituting Equation 34 and 39 into 38,

$$\begin{bmatrix} \omega^2\mu\varepsilon_{xx} - k^2 & \omega^2\mu\varepsilon_{xy} & 0 \\ \omega^2\mu\varepsilon_{yx} & \omega^2\mu\varepsilon_{yy} - k^2 & 0 \\ 0 & 0 & \omega^2\mu\varepsilon_{zz} \end{bmatrix} \begin{bmatrix} E_x \\ E_y \\ E_z \end{bmatrix} = 0 \tag{40}$$

where $\mu = \mu_r \mu_0$ is the magnetic permeability (μ_0 is the permeability of free space), ω is the angular frequency, and k is the propagation constant along the z axis. To obtain the nontrivial solution of Equation 40, the determinant should be zero. Thus, the two solutions for k are

$$k_{\pm}^2 = \frac{\omega^2\mu}{2}\left[(\varepsilon_{xx} + \varepsilon_{yy}) \pm \sqrt{(\varepsilon_{xx} - \varepsilon_{yy})^2 + 4\varepsilon_{xy}\varepsilon_{yx}}\right] \tag{41}$$

Two sets of normal modes can be found after substituting Equation 41 into 40. These normal modes are expressed as

$$\begin{bmatrix} E_x' \\ E_y' \\ E_z' \end{bmatrix} = E_0' \begin{bmatrix} 1 \\ P_+ \\ 0 \end{bmatrix} e^{i(\omega t - k_+ z)} \tag{42}$$

$$\begin{bmatrix} E_x'' \\ E_y'' \\ E_z'' \end{bmatrix} = E_0'' \begin{bmatrix} 1 \\ P_- \\ 0 \end{bmatrix} e^{i(\omega t - k_- z)} \tag{43}$$

where

$$P_\pm = \left[(\varepsilon_{yy} - \varepsilon_{xx}) \pm \sqrt{(\varepsilon_{yy} - \varepsilon_{xx})^2 + 4\varepsilon_{xy}\varepsilon_{yx}} \right] / 2\varepsilon_{xy} \tag{44}$$

and E_0' and E_0'' are arbitrary amplitudes.

Combining Equations 42, 43 and 44, and then transforming these two normal modes into the laboratory coordinates, the matrix representation of CMT that will give the relative phase and amplitude of the x and y electric field at any point z along the axis of propagation can be written as

$$\begin{bmatrix} E_x(z) \\ E_y(z) \end{bmatrix} = \begin{bmatrix} A & B \\ C & D \end{bmatrix} \begin{bmatrix} E_x(0) \\ E_y(0) \end{bmatrix} \tag{45}$$

where

$$A = \cos\phi - i \left[(\varepsilon_{yy} - \varepsilon_{xx}) / \sqrt{(\varepsilon_{yy} - \varepsilon_{xx})^2 + 4\varepsilon_{xy}\varepsilon_{yx}} \right] \sin\phi = D^* \tag{46}$$

$$B = \left(2i\varepsilon_{xy} / \sqrt{(\varepsilon_{yy} - \varepsilon_{xx})^2 + 4\varepsilon_{xy}\varepsilon_{yx}} \right) \sin\phi \tag{47}$$

$$C = \left(2i\varepsilon_{yx} / \sqrt{(\varepsilon_{yy} - \varepsilon_{xx})^2 + 4\varepsilon_{xy}\varepsilon_{yx}} \right) \sin\phi \tag{48}$$

$$\phi = (k_- - k_+) z / 2 \tag{49}$$

From the matrix derivation, it is clear that the matrix elements include both induced linear and circular birefringence. To distinguish the effects from linear or circular birefringence, methods need to be established because independently measuring the electric or magnetic field is mandatory for extracting accurate information of a DUT. For EO sensing, the method follows the Jones matrix calculation in section 1.2, and the electric field of the transmitted probe beam is obtained as follows

$$\mathrm{E}' = \begin{bmatrix} 1 & 0 \\ 0 & 0 \end{bmatrix} \frac{1}{\sqrt{2}} \begin{bmatrix} 1 & -i \\ -i & 1 \end{bmatrix} \begin{bmatrix} \mathrm{A} & \mathrm{B} \\ \mathrm{C} & \mathrm{D} \end{bmatrix} \begin{bmatrix} 0 \\ 1 \end{bmatrix} \tag{50}$$

$$\mathrm{E}' = \frac{1}{\sqrt{2}} \begin{bmatrix} \mathrm{B} - i\mathrm{D} \\ 0 \end{bmatrix} \tag{51}$$

Using the result in Equation 51, the power transfer function can be expressed as

$$\frac{\mathrm{P}_\perp}{\mathrm{P}_{\mathrm{in}}} = \frac{1}{2}[\mathrm{D}^*\mathrm{D} + \mathrm{B}\mathrm{B}^* - i(\mathrm{B}^*\mathrm{D} - \mathrm{B}\mathrm{D}^*)] \tag{52}$$

where $\mathrm{P}_\perp/\mathrm{P}_{\mathrm{in}}$ indicates that the polarizers are crossed. Substituting the Equation 46 and 47 into 52, the power transfer function becomes

$$\frac{\mathrm{P}_\perp}{\mathrm{P}_{\mathrm{in}}} = \frac{1}{2}\left\{1 - \left[\frac{(\varepsilon_{xy}^* + \varepsilon_{xy})\sin 2\phi}{\sqrt{(\varepsilon_{yy} - \varepsilon_{xx})^2 + 4\varepsilon_{xy}\,\varepsilon_{yx}}} + \frac{2i(\varepsilon_{xy}^* - \varepsilon_{xy})(\varepsilon_{yy} - \varepsilon_{xx})\sin^2\phi}{(\varepsilon_{yy} - \varepsilon_{xx})^2 + 4\varepsilon_{xy}\,\varepsilon_{yx}}\right]\right\} \tag{53}$$

In a cubic crystal, the value of ε_x, ε_y, and ε_z are the same, therefore Equations 35, 36, and 37 becomes

$$\varepsilon_{xx} = \varepsilon_0 + \frac{\Delta\varepsilon_l}{2}\cos 2\theta_n \tag{54}$$

$$\varepsilon_{yy} = \varepsilon_0 - \frac{\Delta\varepsilon_l}{2}\cos 2\theta_n \tag{55}$$

$$\varepsilon_{xy} = -\frac{\Delta\varepsilon_l}{2}\sin 2\theta_n + \Delta\varepsilon_c = \varepsilon_{yx}^* \tag{56}$$

Assuming that for a small angle $\sin\phi \approx \phi$, the equation 53 becomes

$$\frac{\mathrm{P}_\perp}{\mathrm{P}_{\mathrm{in}}} = \frac{1}{2}[1 + \Gamma(1 + \sin 2\theta_n + 2\cos 2\theta_n \cdot \theta_F)] \tag{57}$$

In Equation 57, if the angle θ_n is 45 degrees, only the Pockels effect term remains, and the power transfer function becomes directly proportional to the EO phase retardation.

As for MO sensing, the method follows the Jones matrix calculation described in section 1.3, and the electric field of the transmitted probe beam is obtained as follows

$$E' = \frac{1}{2}\begin{bmatrix}1 & 1\\ 1 & 1\end{bmatrix}\begin{bmatrix}A & B\\ C & D\end{bmatrix}\begin{bmatrix}0\\ 1\end{bmatrix} \tag{58}$$

$$E' = \frac{1}{2}\begin{bmatrix}B + D\\ B + D\end{bmatrix} \tag{59}$$

Similar to the EO power transfer function approach, the power transfer function of the MOS optical setup can be expressed as

$$\frac{P_{45}}{P_{in}} = \frac{1}{2}\left\{1 + \left[\frac{2(\varepsilon_{yy} - \varepsilon_{xx})(\varepsilon_{xy} + \varepsilon_{yx})\sin^2\phi}{(\varepsilon_{yy} - \varepsilon_{xx})^2 + 4\varepsilon_{xy}\,\varepsilon_{yx}} + i\,\frac{(\varepsilon_{xy} - \varepsilon_{yx})\sin 2\phi}{\sqrt{(\varepsilon_{yy} - \varepsilon_{xx})^2 + 4\varepsilon_{xy}\,\varepsilon_{yx}}}\right]\right\} \tag{60}$$

$$\frac{P_{45}}{P_{in}} = \frac{1}{2}\left[1 + \frac{1}{4}\Gamma^2 \sin 4\theta_n - 2\theta_F\right] \tag{61}$$

In Equation 61, if the angle θ_n is 0 degrees, only the Faraday effect term remains, and the power transfer function becomes directly proportional to the MO phase retardation. [28]

In summary, to distinguish an MO modulation from an EO modulation, the linearly polarized incident light was made parallel to one of the CMT principal axes. Therefore, no phase retardation could be caused by linear birefringence, and only the effect of the Faraday rotation was revealed. In other words, for MO sensing, a half-waveplate and linear polarizer needs to be used before the CMT to change the input linear polarization angle, and the analyzer was placed after the CMT at 45 degrees relative to the polarizer, allowing the MO signal to be maximized according to Malus' Law and eliminating the induced linear birefringence. On the other hand, for EO sensing, a quarter-waveplate with its slow axis oriented 45 degrees relative to a crossed input polarizer and output analyzer needs to be used to eliminate the induced circular birefringence and set the output to the middle of the typical $\sin^2$, EO-intensity-modulation curve.

2.3 Multiple birefringence measurements

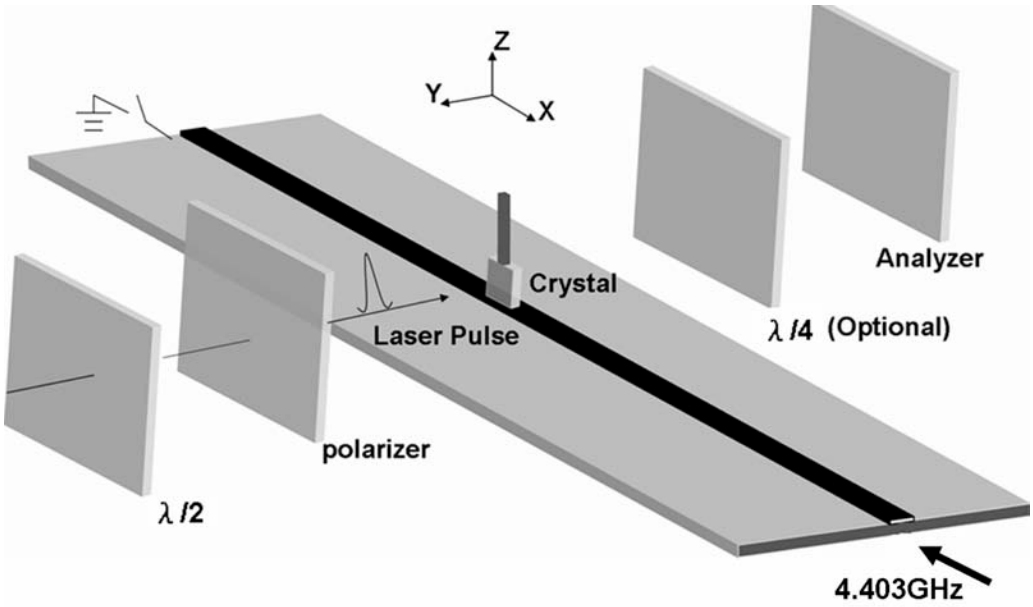

Figure 9 Schematic of the optical setup for the electric and magnetic field sensing measurement. HWP and QWP are half and quarter waveplates, respectively.

A schematic of the optical configuration used to confirm the analysis of combined EO/MO sensing is shown in Figure 9. A single, <110>-oriented CMT crystal doped with 25% manganese ($Cd_{0.75}Mn_{0.25}Te$, zinc blende structure) was employed as the sensing medium. The DUT (and source of the electromagnetic fields) was an open-terminated microstrip transmission line. The 50-Ω microstrip was 14 cm long and constructed from a 4-mm-wide copper electrode on an epoxy resin substrate. The microstrip was scanned using a computer-controlled translation stage, while the CMT remained stationary with its c-axis oriented vertically above the microstrip. The free-space probe beam of 150-fs pulses from a mode-locked Ti:sapphire laser was focused through the crystal within 1 mm of the microstrip surface. The bottom of the CMT was 500 μm above the center of the transmission line, and measurements of the standing-wave patterns from the fringing EM fields were taken every 50 μm. Each scan is 5 cm long, and the RF input frequency is 4.403 GHz. A harmonic-mixing technique as described in section 1.4 is used as the detection method to determine the signal amplitude and phase for all measurements described.

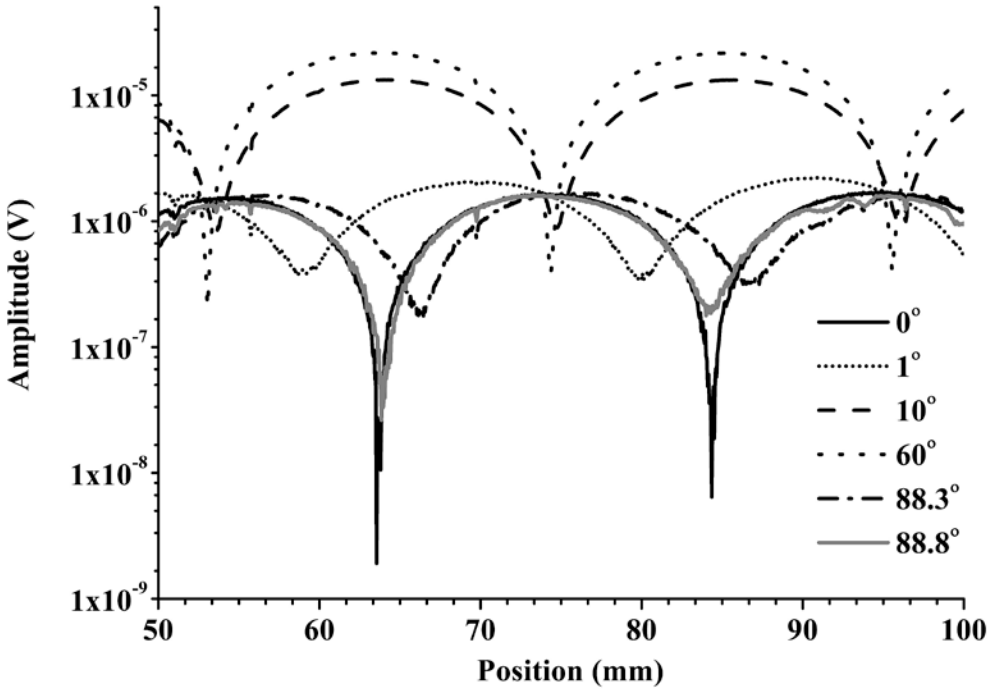

Figure 10 The measured field pattern using the CMT crystal is shifted from magnetic field to electrical field when the polarization angle of the incident light is changed.

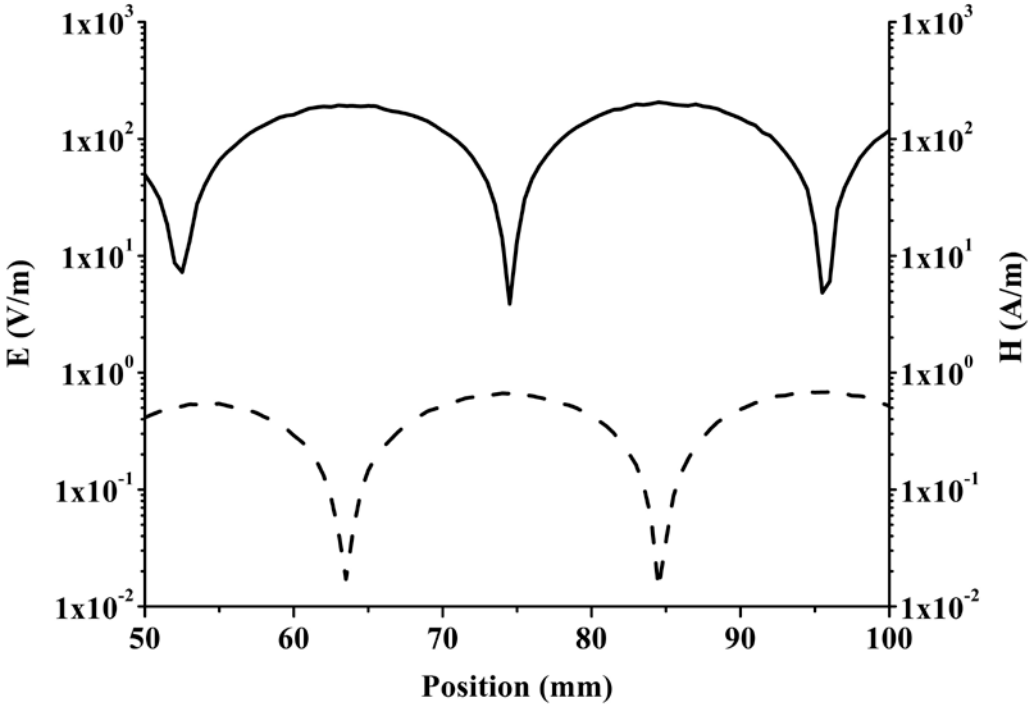

Figure 11 Simulation result of the electric (solid line) and magnetic (dash line) field standing-wave patterns over an open-terminated microstrip center transmission line.

The CMT crystal was found to add no static birefringence, but an induced linear and circular birefringence occurred when an external electrical field was applied with a vector component parallel to the crystal c-axis. Figure 10 shows the experimental results for the intended MO-sensing measurement, which involved a halfwave plate, a polarizer and a analyzer at 45 degrees relative to the polarizer. As the input polarization angle was rotated from 0 to 90 degrees, the measured field patterns were found to be identical at 0 and 88.8 degrees, with the minimum-amplitude points at 63.55 and 84.35 mm. The position of these minima shifted when the input polarization angle was changed. After being simulated with Ansoft HFSS 10, a full-wave EM-field solver, the electric and magnetic field patterns along the open-terminated microstrip transmission line can be visualized (Figure 11), the field components would observed experimentally correspond to E_z and H_y. The valleys where the electric field has minimum signal intensity correspond to the peak values of the magnetic field due to the standing-wave pattern induced by the open termination.

Compared to the experimental results in Figure 10, the simulated magnetic field has minimum points at 63.5 and 84.5 mm, implying that the measured fields at 0 and 88.8 degrees are magnetic field. The two identical field minima indicate that the linear polarization of the pulsed laser probe beam is parallel to the orthogonal principal axes of the CMT crystal at those points, and hence, there is no EO effect and only magnetic field is measured. However, according to Equation 61, even when the linear input optical polarization angle is changed by small amounts, so that it deviates only slightly from one of the principal axes, i.e., at values such as 0.5 and 88.3 degrees, the field pattern changes so that it appears to be a combination of EO and MO effects. This combination can also be proven by the positions of the minimum signal intensities for the linear polarization angles falling between the valleys, which indicates the presence of pure electric or magnetic field. The electric field sensitivity quickly dominates over the magnetic field sensitivity when the linear polarization angle moves away from 0 and 88.8 degrees. Although the signal contains both EO and MO components, the valley positions of 10 and 60 degrees at 53.1 mm, 74.5 mm and 95.5 mm closely mimic the simulation result for E_z in Figure 11. This is because the MO phase retardation is negligible compared to the EO effect. The flexibility afforded by CMT for independently measuring either

electric or magnetic field is thus demonstrated for the case where the linear polarization angle of the laser pulses can be changed precisely.

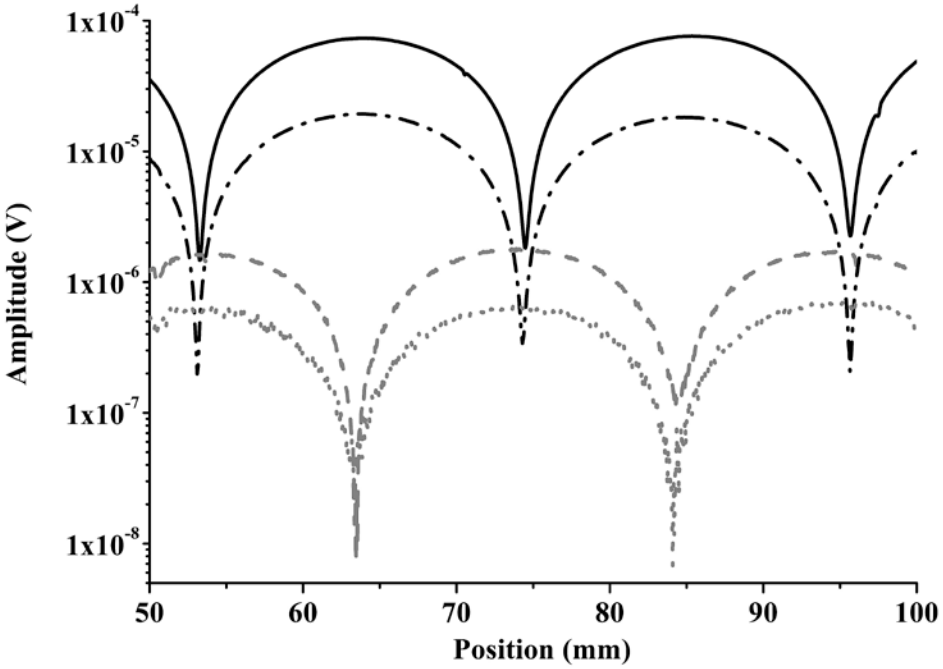

Figure 12 Experimental results for the field patterns over the center of the open-terminated microstrip transmission line measured by three crystals. The electric field is indicated by the black solid line (—) and dash dot line (– •) as measured by the CMT and $LiTaO_3$ crystals, respectively. The magnetic field is indicated by the gray dash line (--) and dot line (••) as measured by the CMT and TGG crystals, respectively.

To reinforce the dual nature of the field sensitivity of the CMT probe, the intensity and accuracy of the signals in Figure 10 are compared with measurements from two crystals that exhibit sensitivity exclusively to either electric or magnetic fields: $LiTaO_3$ and TGG, respectively. The thickness of $LiTaO_3$, TGG and CMT were 0.6 mm, 1 mm and 1 mm respectively. The optic axis of $LiTaO_3$ was along the z-axis, and the induced principal axis of CMT was in the x-z plane, based on the previous measurement. Again, for MO sensing, a halfwave plate, a polarizer and an analyzer at 45 degrees relative to the polarizer were used. However, for EO sensing, a quarter-waveplate with its slow axis oriented 45 degrees relative to a crossed input polarizer and an output analyzer was used. The input optical polarization is set 45º relative to the in-plane principal axes of the EO crystal.

Figure 12 shows the measured electric and magnetic field patterns for the three crystals. As can be seen, the valley positions of the electric field measured by CMT are 53.25, 74.5, and 95.7 mm, demonstrating outstanding agreement with the valley positions, 53.1, 74.3, and 95.7 mm, of the electric-field standing wave measured by $LiTaO_3$. Similarly, the valley positions of the magnetic-field standing-wave measured by the CMT are 63.4 and 84.2 mm, matching well with those measured with TGG (63.3 and 84.1 mm).

In regards to signal magnitude, the peak values of both EO and MO modulated signal intensity for CMT are 6 dB higher than for $LiTaO_3$ and TGG. The contrast ratios for the EO and MO signal intensity of CMT are 16 and 25 dB, respectively. Although the contrast ratio for the EO signal intensity of CMT is 4 dB less than that of $LiTaO_3$, the contrast ratio for the MO signal intensity of CMT is 5 dB higher than with TGG. Given the same thickness of 1 mm, CMT definitely shows an advantage over TGG as an MO crystal sensor due to its higher Verdet constant at the 800-nm wavelength employed (2.2 vs 0.29 min/Gs-cm).

Finally, by using Equation 57 and the experimental results shown in Figure 12, the linear EO coefficient r_{41} of CMT can also be calculated for the first time. Comparing the signal-intensity difference with the EO phase retardation between $LiTaO_3$ and CMT, the r_{41} is found to be 3.5 ± 0.2 pm/V.

2.4 Conclusions

In conclusion, this Chapter began by describing the physics of the multiple birefringences in a diluted magnetic semiconductor. The induced linear birefringence of CMT is inherent from its host semiconductor, CdTe, and the induced circular birefringence is generated from the strong exchange interaction between the d spins of the manganese ions and electrons in CMT crystal. In addition to the physical mechanism, a mathematical representation in the matrix form of a crystal with multiple birefringence is also derived from the basic Maxwell equations. With this matrix, the power transfer functions for EO and MO sensing can be calculated. The use of the calculated power transfer functions shows that a CMT crystal may be used to make independent measurements of electric and magnetic fields if the polarization is precisely controlled. If the polarization of the probe beam is not controlled, the electromagnetic field pattern

measured by CMT becomes a mixture of electric and magnetic effects. However, if the linearly polarized incident light is made parallel to one of the CMT principal axes, then CMT measures only magnetic fields. Moreover, if a quarter-waveplate with its slow axis oriented 45 degrees relative to a crossed input polarizer and output analyzer is used, then CMT measures only electric fields.

By rotating the linear polarization angle of the incident laser pulses with the optical setup used for MO sensing, the measured field pattern of a single microstrip transmission line appears to be a mixture of electric and magnetic field. Furthermore, the experimental data are compared with the reference EO and MO crystals. The comparison proves that the CMT crystal possesses both induced circular and linear birefringences, as compared to other work that appears to have overlooked electric-field sensitivity through the use of a different crystal orientation.[29]

Chapter 3
Poynting Vector Sensor

Since the capability of CMT to measure both electric and magnetic fields has been demonstrated, it should be possible to combine amplitude and phase information from orthogonal components of these fields in order to produce an experimental magnitude and direction of the Poynting vector of a signal. In this Chapter, the <110>-oriented CMT crystal discussed in Chapter 2 is again employed as a sensing medium in the microwave region. Using the multiple birefringence characteristic of this CMT crystal, a Poynting vector sensor is developed. The feasibility of this application is demonstrated by comparing the measured energy flow of a single microstrip transmission line under open-termination and matched-load conditions.

3.1 Introduction

In recent years, near-field electromagnetic (EM) wave behavior, often involving the evanescently decaying waves common to plasmonic devices, has attracted considerable attention as efforts to understand and improve metamaterial structures has increased. Moreover, given appropriate knowledge of the EM-wave behavior, some applications, like invisibility cloaking and superlensing, have been realized through controlling propagation of the Poynting vector.[30, 31] Currently, the most commonly used numerical methods to study the Poynting vector propagation are the finite-difference time-domain (FDTD) technique and the finite-element method (FEM).[32-34] These methods, however, usually exhibit discrepancies between the simulation and the behavior of real devices. Thus, experimental measurement of the Poynting vector remains an active research topic for any device that radiates energy. [35, 36]

Even without considering their intrusiveness, one serious limitation of current field-measurement techniques is that they only detect the electric-field component, and hence

further transformational calculation, which requires the substitution of the measured electric field into Equation 63 for obtaining the magnetic field, is necessary to estimate the real Poynting vector of a signal.[37-39] In particular, when one is in the near field where the electric and magnetic fields are not orthogonal, it is not sufficient to determine the Poynting vector solely through knowledge of either the electric or magnetic field, but rather it is necessary to know the characteristics of both. In this Chapter, I describe the development of a noninvasive Poynting vector probe which does not require knowledge of the physical properties of a DUT, in contrast with typical measurement techniques that require the permittivity or dimensions of the DUT for the transformational calculations.

Here, CMT has been used to extract Poynting-vector maps at microwave frequencies in proximity to a microstrip transmission line without the need for transformational calculations. Recalling the results of Chapter 2, both the Pockels effect and Faraday effect exist within CMT to the extent that they are effective at sensing electromagnetic fields. That is CMT may be used to independently measure either electric or magnetic fields if the linear polarization angle of an incident optical beam can be adjusted precisely.[40] Considering the definition of the Poynting vector, if both electric and magnetic fields can be measured by a single sensor, it is possible to experimentally obtain the energy flow on a local scale and in the near field.

3.2 Calculation of the Poynting vector from its constituent fields

The definition of the Poynting Vector can be derived from Maxwell's equations,

$$\vec{\nabla} \times \vec{\mathrm{H}} = \vec{\mathrm{J}} + \varepsilon \frac{\partial \vec{\mathrm{E}}}{\partial \mathrm{t}} \tag{62}$$

$$\vec{\nabla} \times \vec{\mathrm{E}} = -\mu \frac{\partial \vec{\mathrm{H}}}{\partial \mathrm{t}} \tag{63}$$

where J is the total current density. Substituting Equations 62 and 63 into the vector identity as expressed in Equation 64,

$$\nabla \cdot \left(\vec{\mathrm{E}} \times \vec{\mathrm{H}}\right) = \vec{\mathrm{H}} \cdot \left(\nabla \times \vec{\mathrm{E}}\right) - \vec{\mathrm{E}} \cdot \left(\nabla \times \vec{\mathrm{H}}\right) \tag{64}$$

Equation 64 becomes

$$\nabla \cdot \left(\vec{E} \times \vec{H}\right) = -\vec{H} \cdot \mu \frac{\partial \vec{H}}{\partial t} - \vec{E} \cdot \vec{J} - \vec{E} \cdot \varepsilon \frac{\partial \vec{E}}{\partial t} \tag{65}$$

$$\nabla \cdot \left(\vec{E} \times \vec{H}\right) = -\frac{\partial}{\partial t}\left(\frac{1}{2}\mu H^2 + \frac{1}{2}\varepsilon E^2\right) - \vec{E} \cdot \vec{J} \tag{66}$$

Equation 66 can be rewritten in an integral form by integrating both sides over the volume, v, of concern

$$\oint_s \left(\vec{E} \times \vec{H}\right) d\vec{s} = -\frac{\partial}{\partial t}\int_v \left(\frac{1}{2}\mu H^2 + \frac{1}{2}\varepsilon E^2\right) dv - \int_v \vec{E} \cdot \vec{J} dv \tag{67}$$

where the divergence theorem has been applied to convert the volume integral of $\nabla \cdot \left(\vec{E} \times \vec{H}\right)$ to the closed surface (s) integral of $\vec{E} \times \vec{H}$.[41] Equation 67 is referred to as Poynting's theorem. The first integral on the right hand side of Equation 67 represents the time-rate of change of the energy stored in the electric and magnetic field. The second integral on the right hand side of Equation 67 represents the instantaneous ohmic power dissipated in the volume v. The right hand side of the equation 67 can, therefore, be interpreted as the rate of decrease in the electric and magnetic energies stored, minus the ohmic power dissipated as heat in the volume v. To be consistent with the law of energy conservation, the left hand side of the Equation 67 must be the rate of energy leaving the volume through its surface. Thus, the Poynting vector represents the power flow per unit area, which is defined as

$$\vec{P} = \vec{E} \times \vec{H} \tag{68}$$

In phasor form, the Poynting vector is expressed as

$$\vec{P} = \frac{1}{2}\vec{E} \times \vec{H}^* \tag{69}$$

Equation 69 shows that only mutually perpendicular components of E and H contribute to the power flow; the direction of the flow is normal to the plane containing E and H. Thus, in rectangular coordinates, the complex Poynting vector per unit area normal to the y-z plane can be written as

$$P_x = \frac{1}{2}\left(E_z H_y^* - E_y H_z^*\right) \tag{70}$$

According to Equation 69, if the CMT can be used to independently measure the components of the electric and magnetic fields, then this will allow the relative poynting vector of the DUT to be mapped out. Moreover, the actual Poynting vector value can be found by utilizing the same crystal, CMT, to obtain the electric and magnetic field strengths, which can then be multiplied by a constant, the refractive index of CMT at the operating frequency of the DUT. This is because

$$E_{CMT} = \frac{E_{air}}{\sqrt{n}} \tag{71}$$

where Equation 71 assumes that there are no reflection and refraction losses when the field enters the CMT.[42] Therefore, from Equation 71, it is obvious that the measured electric field is less than the actual radiating electric field in the air by a factor of the square root of n. Since the magnetic field is also perturbed by the CMT crystal following the same trend as the electric field, the measured Poynting vector is less than the actual Poynting vector by a factor of n. In addition, Equation 71 also explains that separately measuring the electric and magnetic field by using different crystals may not give an accurate Poynting vector value. This error can arise due to different field perturbations arising when the refractive indices of the crystals differ, such as when using ZnTe and TGG to measure the electric and magnetic fields, respectively.

3.3 Poynting vector measurement

3.3.1 CMT without high reflection coating

In order to confirm the feasibility of acquiring the Poynting vector from its constituent fields, the first part of the experimental investigation used the setup from Figure 9 in Chapter 2. The bottom of the CMT was suspended 500 μm above the center of the transmission line, and the measurements from the fringing EM fields were periodically obtained during a raster scan at 400 μm intervals. Each scan is 5 cm by 2 cm, and 4.403 GHz is used as the RF input. Again, the harmonic-wave-mixing technique described in section 1.4 employing a short-pulse laser is used as the detection method to measure the signal amplitude and phase for all measurements described. Both open-termination and matched-load conditions for the DUT are used during the measurements for comparison,

as it is expected that the Poynting vectors should exhibit differences in amplitude and phase.

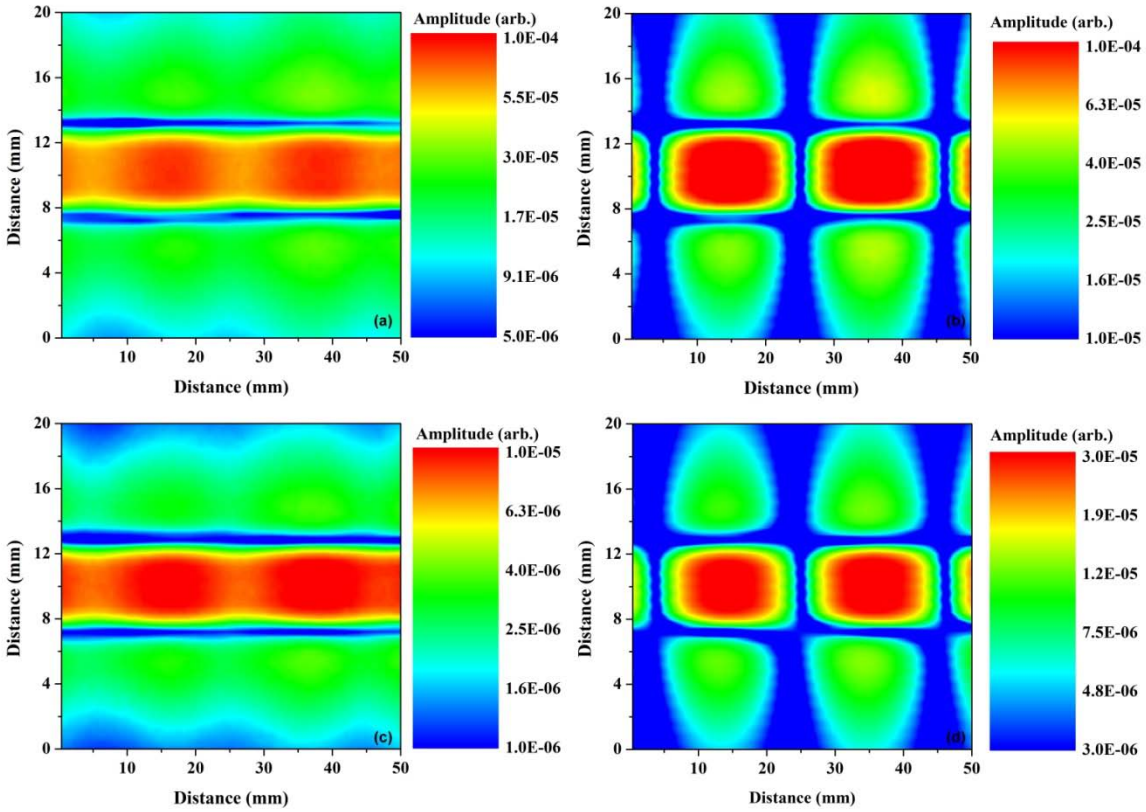

Figure 13 Near field patterns of E_z electric field of a microstrip transmission line (a) with a 50-Ω load, and (b) with an open termination, using a ZnTe crystal; (c) with a 50-Ω load and (d) with an open termination, using a CMT crystal.

For EO sensing, a quarter waveplate with its slow axis oriented 45 degrees relative to a crossed input polarizer and output analyzer is used, and the input optical polarization is set 45 degrees relative to the in-plane crystal principal axes. As discussed in section 2.2, under the EO-sensing optical configuration, CMT measures only the E_z field of the transmission line. Figure 13 shows the measured electric-field patterns of this component for a microstrip transmission line. A typical EO sensing crystal, ZnTe is used as a reference for comparison, as shown in Figure 13(a) and (b), where Figure 13(a) shows the field pattern of the DUT terminated for a 50-Ω load, and Figure 13(b) shows the field pattern for an open termination. Compared to the electric-field measurements from ZnTe,

Figure 13(c) and (d) demonstrate the measured field patterns of the DUT for a 50-Ω load and with an open termination, respectively, using a CMT crystal. The measured field amplitude for the ZnTe crystal is higher than that using CMT because the n^3r figure for merit of ZnTe is larger than that for CMT at an 800nm wavelength. However, the positions of the peaks and valleys of the measured field pattern are the same for both ZnTe and CMT, which proves that the electric field can be accurately measured by employing CMT as an EO sensing crystal.

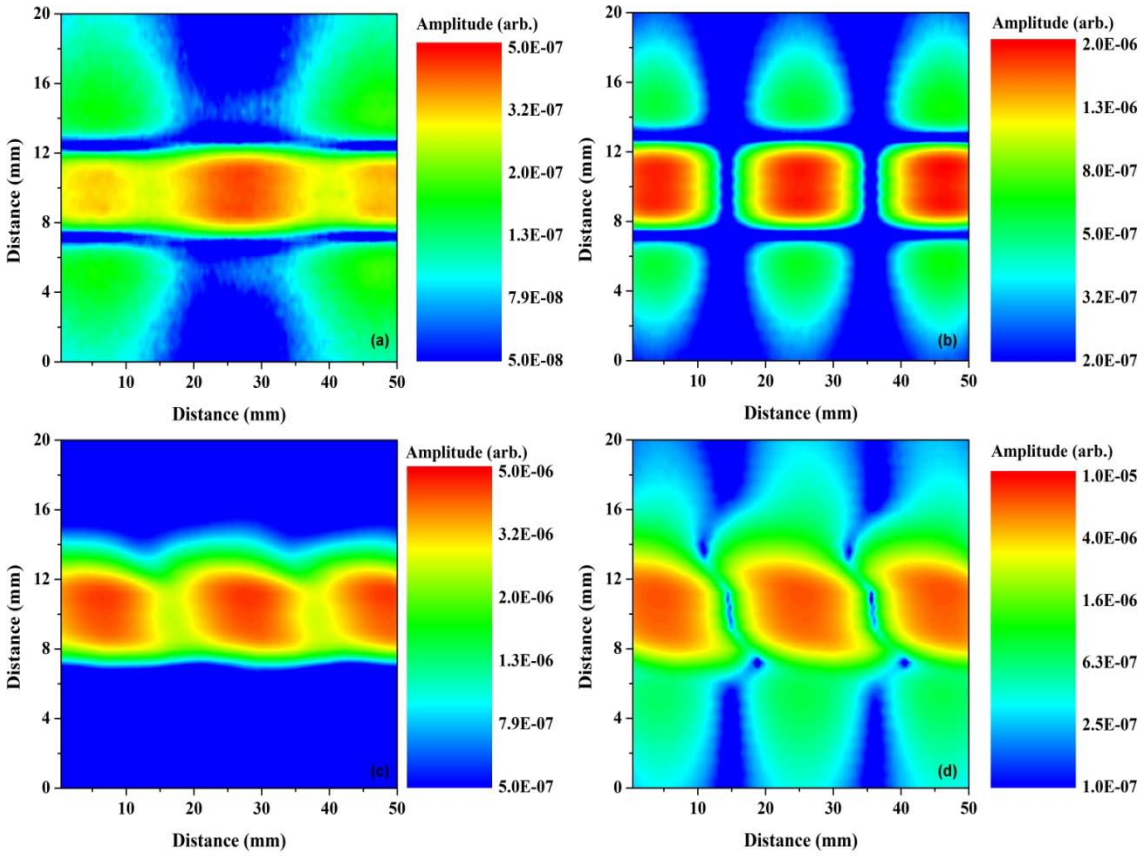

Figure 14 Near field patterns of H_y magnetic field of a microstrip transmission line (a) with a 50-Ω load, and (b) with an open termination, using a TGG crystal; (c) with a 50-Ω load and (d) with an open termination, using a CMT crystal.

For MO sensing, the linear polarization angle of the laser is made parallel to the induced principal axes of the CMT, and hence the crystal measures only the H_y field of the transmission line as described in section 2.3. A reference MO crystal, TGG is used for comparison, as depicted in Figure 14(a) and (b) where Figure 14(a) shows the field

pattern of the DUT terminated with a 50-Ω load and Figure 14(b) shows the field pattern with an open termination. Compared to the magnetic field measurements from TGG, Figure 13(c) and (d) demonstrate the field pattern of the DUT with a 50-Ω load and an open termination by using a CMT crystal, respectively. The measured field amplitude for a CMT crystal is higher than that of TGG, since the Verdet constant of CMT is larger than that of TGG at 800-nm wavelength. The periodic field peaks in Figure 14(a) and (c) arise due to the imperfect match of the load to the line impedance. This imperfect match results in the residual standing wave behaving like the measurements in section 2.3, where the position of the peak of the magnetic fields is the valley of the electric fields in Figure 13. The measured magnetic fields at the edges of the transmission line in Figure 14(d) are also slightly distorted. This is because the polarization of the probe pulses is not perfectly parallel to the induced principal axes of the CMT, and hence the probe beam is extracting a mixture of magnetic and electric fields as shown in Figure 10. However, with the exception of the edge field pattern, the positions of the peaks and valleys of the measured fields are the same for both TGG and CMT, which proves that the magnetic field can be accurately measured by employing CMT as an MO crystal.

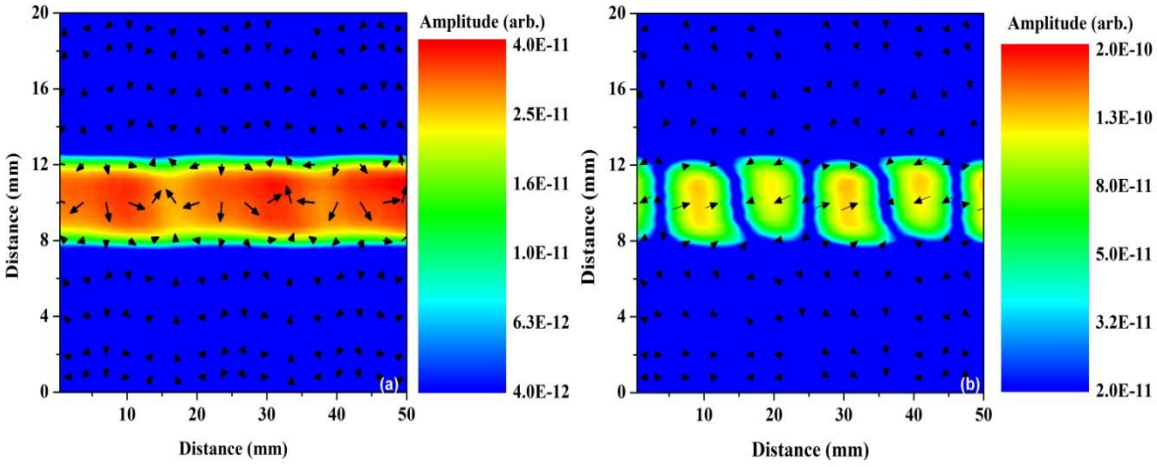

Figure 15 Experimental x-directed Poynting vector of a 4.4 GHz signal on a microstrip terminated with (a) a 50-Ω load and (b) an open circuit. The arrows represent the phase of the Poynting vector and the arrow tails, along with the color scale, represent its amplitude.

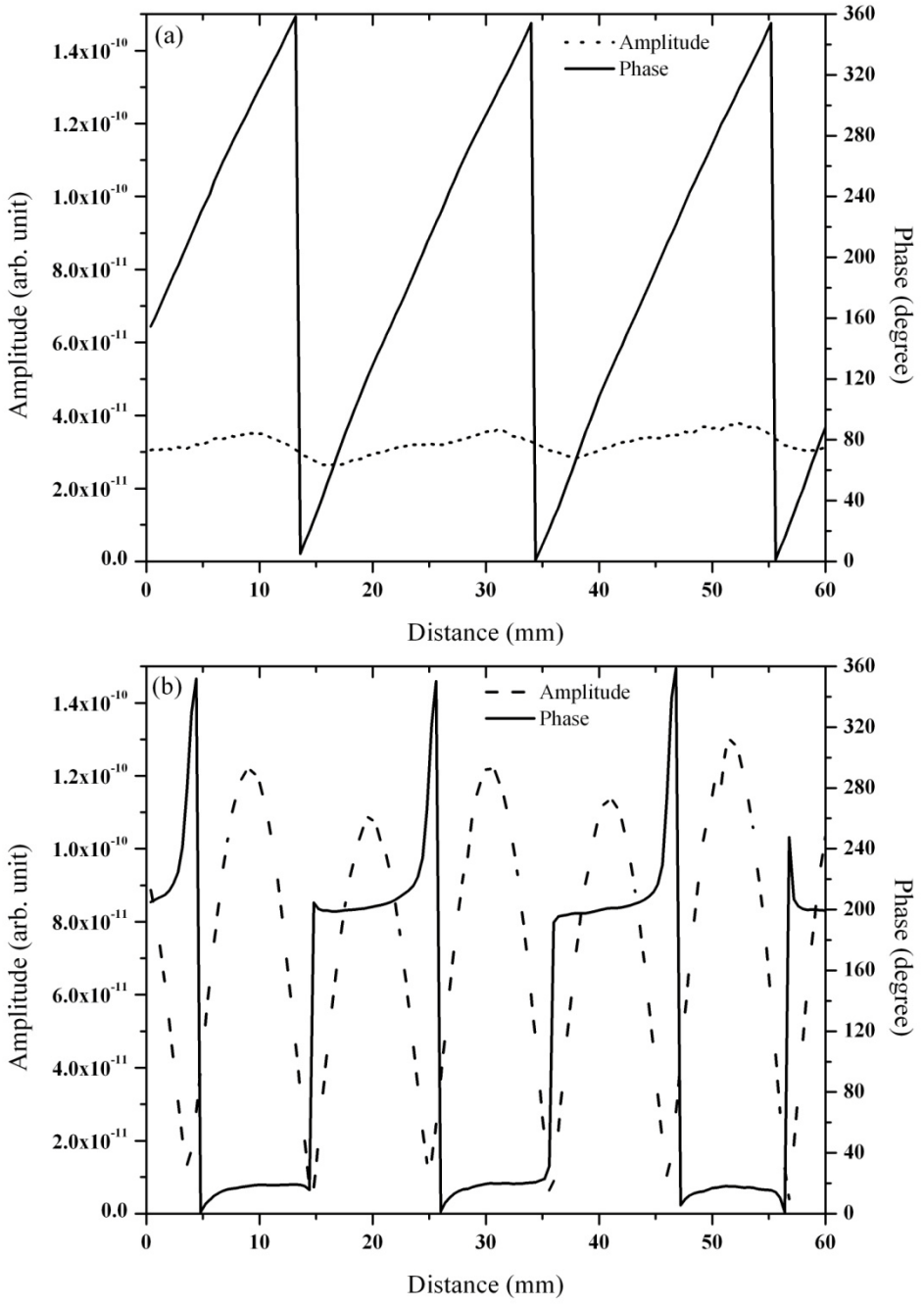

Figure 16 Experimental data showing the amplitude and phase variation of the partial Poynting vector, P_x, only using the measured H_y and E_z components versus probe position along the center of the microstrip terminated with (a) a matched load and (b) an open circuit.

Figure 15(a) shows the measured Poynting vector, P_x, determined by multiplying the amplitudes and subtracting the phases of H_y magnetic field from the E_z electric field according to the first term on the right hand side of Equation 70. Again, a very weak standing wave pattern exists due to an imperfect load match. For comparison, the Poynting vector of the same transmission line with an open termination is shown in Figure 15(b). From the amplitude distributions in Figure 15, it is clear that the 50-Ω load condition allows energy to flow along the microstrip in the x direction, whereas the open-terminated transmission line has no continuous energy flow.

In order to better quantify the Poynting-vector maps, the phase and amplitude of the quantity along the center of the microstrip line in Figure 15 were plotted in Figure 16. The phase (Figure 16(a)) demonstrates that the Poynting vector is traveling with a constantly varying phase along the x direction, as expected from a propagating signal. Figure 16(b) shows that the phase of adjacent peaks of the standing wave pattern were 180º out of phase, representative of a standing wave pattern with no energy flow along the x direction.

3.3.2 CMT with high reflection coating

This work shows the feasibility of employing a CMT crystal as a Poynting-vector sensor. However, it must be noted that the experiment measures only a partial Poynting vector. To measure all of the field components, a single, <110>-oriented CMT crystal that was doped with 25% manganese ($Cd_{0.75}Mn_{0.25}Te$) and onto which was deposited a high-reflection coating (on one side of the crystal) was employed as the sensing medium. This was done so that when the sensor crystal was oriented to measure the electric field out of the plane of the microstrip surface, as well as the magnetic field within this plane, the optical pulses could be returned to the probe-beam photodetector.

The harmonic-wave-mixing technique employing a short-pulse laser was used again as the detection method to measure the signal amplitude and phase for all measurements. The detailed experimental configuration is shown in Figure 17, where the CMT with high reflection coating can be seen to reflect the probe beam. The pellicle has a 50/50 transmission/reflection ratio. The dashed-box in Figure 17 includes the CMT and the DUT (depicted as the source of the electromagnetic (EM) fields), which was still the 50-

Ω microstrip transmission line with a matched load. In order to measure all necessary field components, the CMT is mounted in two different ways as shown in Figure 18.

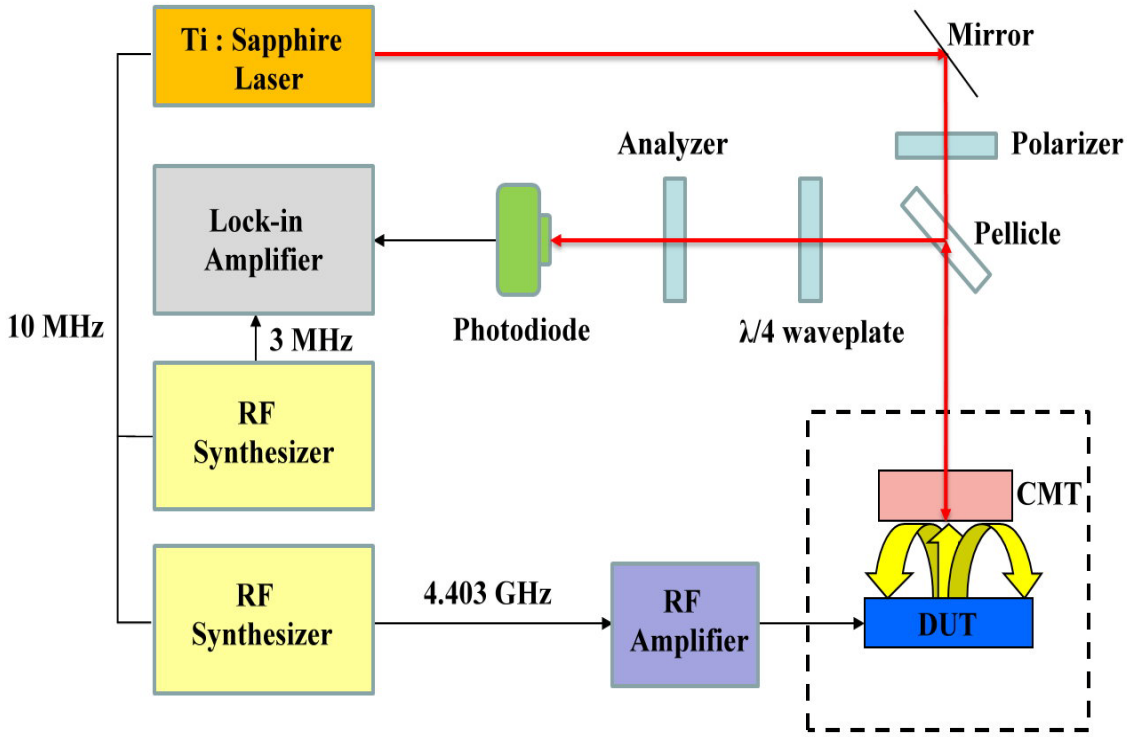

Figure 17 Experimental configuration for the Poynting Vector measurement using a CMT sensor coated with a high reflection dielectric stack.

The vertically mounted CMT in Figure 18(a) can measure the E_z or H_y field components since the <110> face is along the x-z plane. On the other hand, the horizontally mounted CMT in Figure 18(b) can measure the E_y or H_z field. Combining the results from Figure 18(a) and (b) using Equation 70 will yield the complete Poynting vector value. Since the Poynting vector should be different for the 50-Ω microstrip transmission line with an open termination and one with a matched load, both conditions are measured in Figure 18(a) and (b) to help substantiate the measurement capability.

The 50-Ω microstrip was 14 cm long and 4 mm wide and constructed from copper electrodes on an epoxy resin substrate. The microstrip was raster-scanned using a computer-controlled translation stage, while the CMT remained stationary with its c-axis oriented vertically or horizontally above the microstrip. The free-space probe beam of

80-fs pulses from a mode-locked Ti:sapphire oscillator was focused through the crystal within 1 mm of the microstrip surface. The bottom of the CMT was suspended 300 μm above the center of the transmission line, and the measurements from the fringing EM fields were periodically obtained at 100 μm intervals. Each scan is 5 cm by 2 cm with the center at the middle of the transmission line, and 4.403 GHz was used as the RF input.

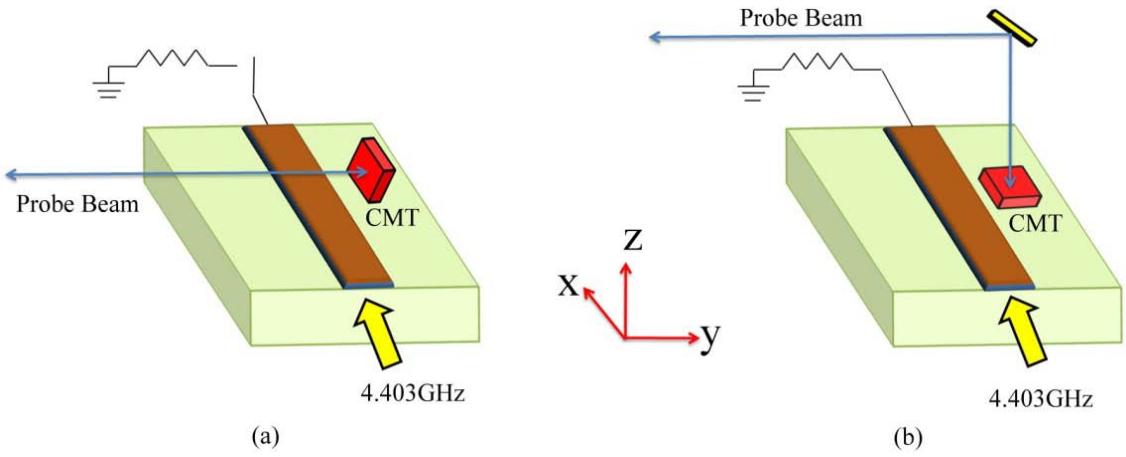

Figure 18 Experimental concept for measuring (a) the E_z or H_y field component and (b) the E_y or H_z field components of a 50-Ω microstrip transmission line using a single CMT crystal.

The polarizers and wave plate setup follows the same methods as described in section 2.2. For EO sensing, a quarter waveplate with its slow axis oriented 45 degrees relative to a crossed input polarizer and output analyzer was used, and the input optical polarization was set 45 degrees relative to the in-plane crystal principal axes; thus, CMT measures only the E_z and E_y field of the transmission line as shown in Figure 18(a) and (b), respectively. For MO sensing, the linear polarization angle of the laser was made parallel to the induced principal axes of the CMT; thus, the crystal measures only the magnetic field of the transmission line. A linear polarizer that changes the input linear polarization angle was used before the probe beam propagated through CMT. The analyzer was placed at 45 degrees relative to the polarizer after the probe beam reflected back from the CMT, allowing the MO signal to be maximized according to Malus' Law.

Figure 19 shows the measured E_z electric field when the CMT was mounted out of the plane of the microstrip, as in Figure 18(a). The E_z electric-field amplitudes for part of the area over the microstrip for both the open-termination and matched-load conditions are plotted in Figure 18(a) and (b), respectively using the same amplitude scale. Along the center strip of the transmission line, a standing-wave pattern with three nodes at 4.8 mm, 25 mm, and 46 mm can be seen in Figure 19(a), as indicated by the large periodic changes in field amplitude. A travelling wave is clearly observed in Figure 19(b), where there is little spatial variation of the electric field along the strip. The periodic small field peaks that do appear in Figure 19(b) arise from the imperfect match of the load to the line impedance.

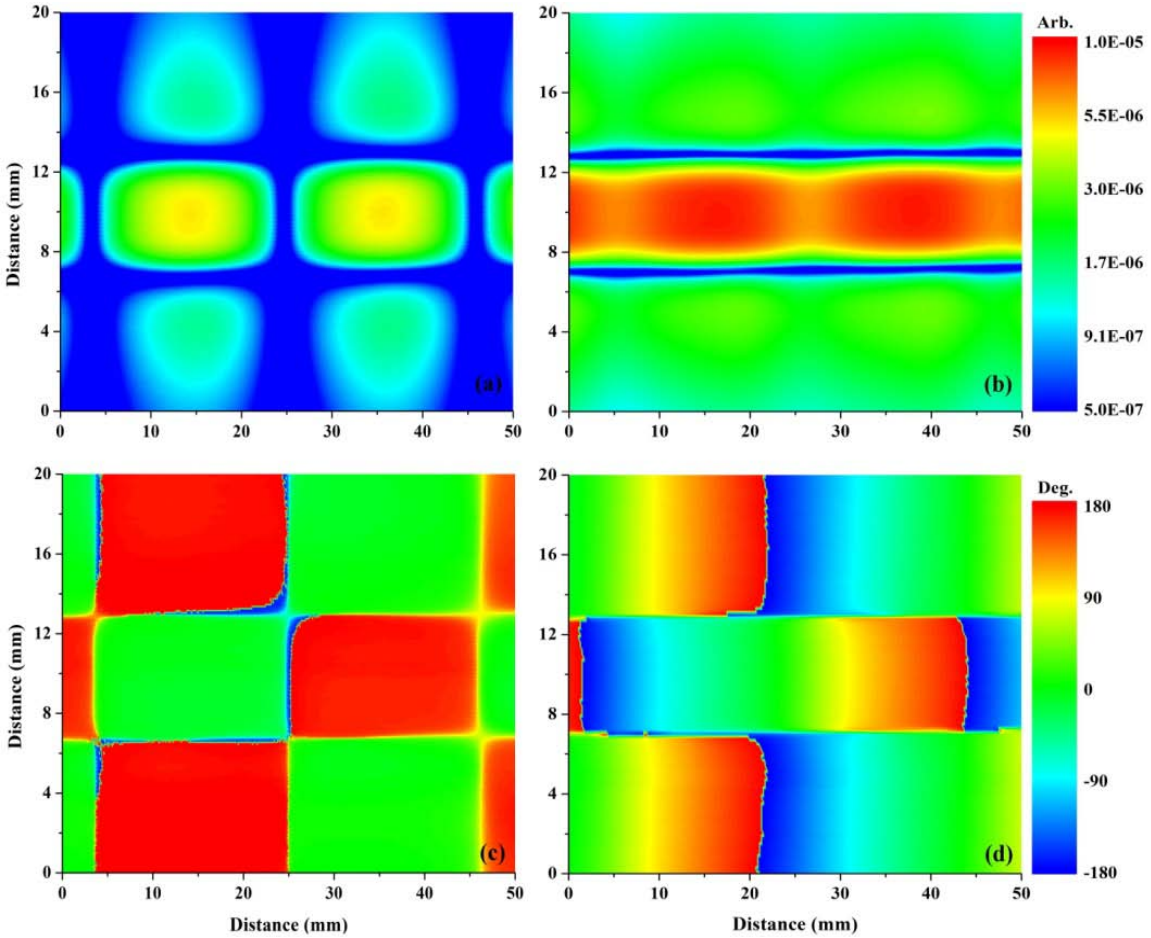

Figure 19. Experimental results of the E_z amplitude measured using the CMT for (a) open and (b) matched-load terminations. The phase of E_z is also shown for (c) open and (d) matched-load terminations.

Similarly, the E_z electric-field phase for the open-termination and matched-load conditions are plotted on a scale from -180 degrees to +180 degrees in Figure 19(c) and (d), respectively. Again looking along the center strip of the transmission line, the phase in Figure 19(c) abruptly alternates 180 degrees with the adjacent rectangular parts of the field pattern, indicating that the amplitude in Figure 19(a) represents peaks and valleys in the standing wave generated by the open termination. In contrast, the phase in Figure 19(d) varies from -180 degrees to 180 degrees continuously for both the field over the stripline as well as outside the top strip, demonstrating again that the amplitude in Figure 19(b) represents a travelling wave allowed by the matched-load termination.

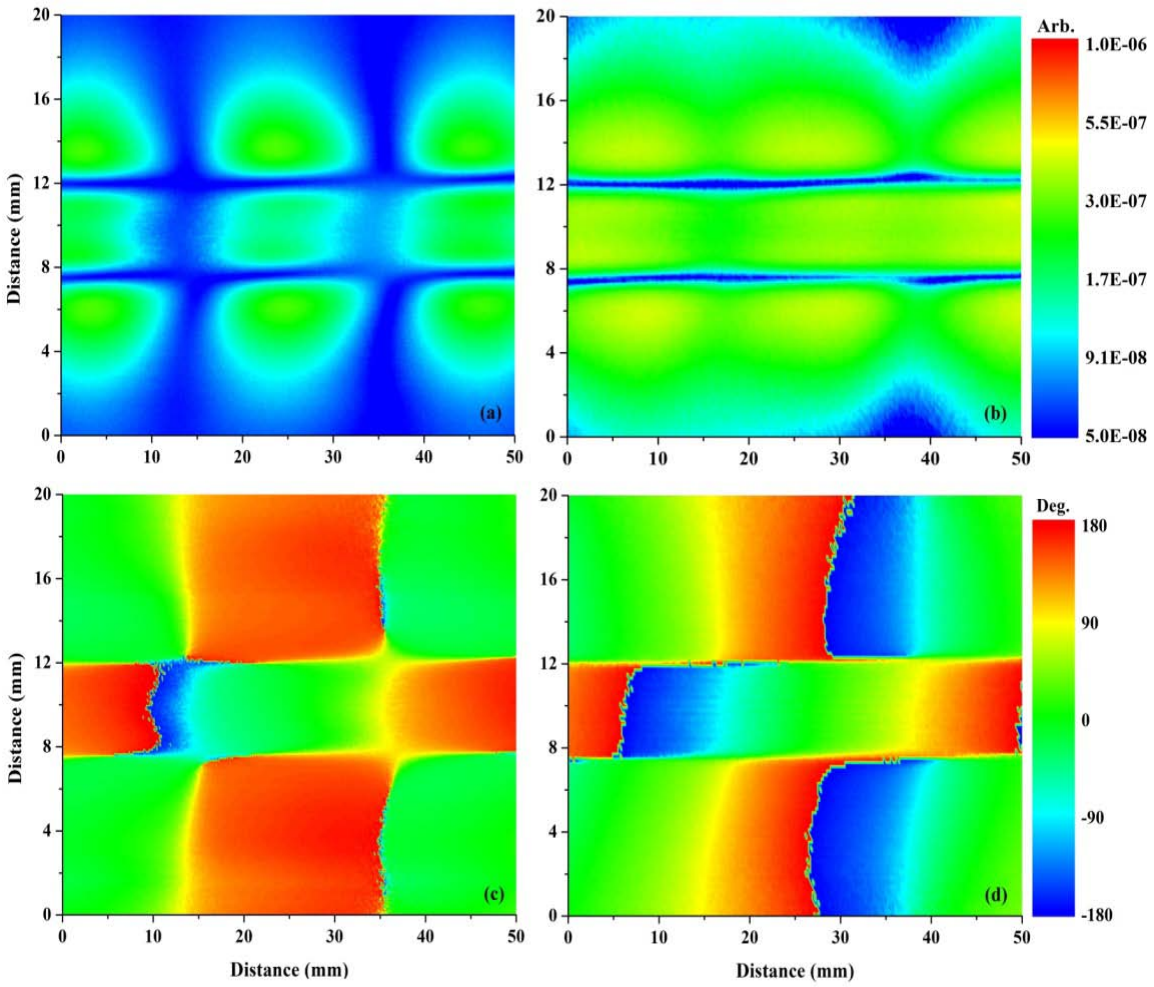

Figure 20 Experimental results of H_y amplitude measured using the CMT for (a) open and (b) matched-load terminations. The phase of H_y is also shown for (c) open and (d) matched-load terminations.

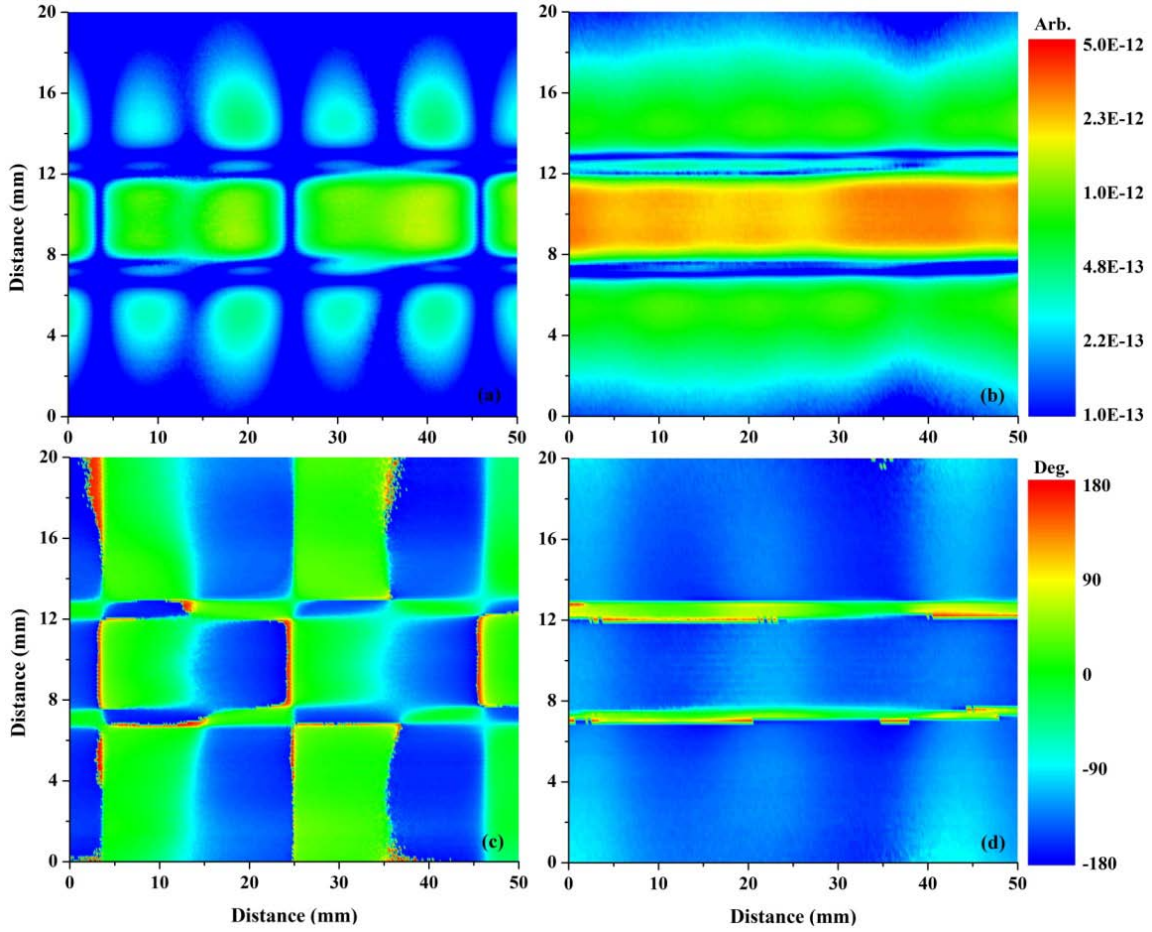

Figure 21 Experimental results of the partial Poynting-vector amplitude calculated from E_z and H_y for (a) open and (b) matched-load terminations; partial Poynting-vector phase for (c) open and (d) matched-load terminations.

Setting the conditions in Figure 18(a) to MO sensing by rotating the input linear polarization by 45 degrees and removing the quarterwave plate, the measured H_y magnetic field is obtained as shown in Figure 20. The H_y magnetic field amplitudes for the open-termination and matched-load conditions are plotted with the same amplitude scale in Figure 20(a) and (b), respectively. Here, a standing-wave pattern with two nodes at 14.8 mm and 35.4 mm can be seen in Figure 20(a), whereas a travelling wave is clearly present in Figure 20(b). Compared to Figure 19(a), Figure 20(a) can be seen to exhibit the magnetic field only, since the node positions of the magnetic field correspond to the peak positions of the electric field. The H_y magnetic-field phase for the open termination and matched load plotted in Figure 20(c) and (d), respectively, have similar behaviors

compared to Figure 19(c) and (d), where the phase changes 180 degrees from the adjacent peak for the open termination, and the phase changes continuously along the transmission line for the matched load.

Possessing the measured data of Figures 19 and 20, the first term on the right hand side of Equation 70 can be used to calculate a partial experimentally determined Poynting vector, P_x. Multiplying the amplitudes of the E_z electric field in Figures 19 and the H_y magnetic field in Figures 20, the partial P_x amplitude for the open-termination and matched-load conditions are plotted with the same amplitude scale in Figures 21 (a) and (b), respectively.

At the edge of the transmission line, for the distances 7 mm and 13 mm on the vertical scale, there is almost no electric field exhibited along the z direction, and no magnetic field existed along y direction, therefore, the partial Poynting vector shows discontinuity. Subtracting the phases of the H_y magnetic field in Figures 20 from the phase of the E_z electric field in Figures 19, the partial P_x phase for the open and matched loads are plotted from -180 degrees to 180 degrees in Figures 21(c) and (d), respectively. The phase alternates 180 degrees at the nodes of the electric and magnetic field, which further substantiates that the energy does not flow along the open-terminated transmission line. On the other hand, for the matched load, the energy appears to flow along the transmission line with a phase that remains essentially constant. The phase in Figure 21(d) does vary slightly due to the imperfect load match.

In order to measure the second term of the Poynting vector, $E_yH_z^*$, on the right hand side of Equation 70, the CMT was mounted horizontally, or parallel to the plane of the microstrip surface, as shown in Figure 18(b). Figure 22 shows the measured E_y electric field. Both the open and matched-load terminations show a minimum amplitude at the center of the transmission line, since most of the electric fields are along the z direction. On the other hand, both open and matched-load terminations show their maximum amplitude at the edges of the transmission line where E_y is the strongest.

Comparing the measured results to those of Figure 19(a), a standing wave pattern with three nodes at 4.8mm, 25mm, and 46mm can also be observed in Figure 22(a). The

phase of the measured electric field also behaves like that in Figure 19(c) and (d), where the phase of the open terminated microstrip alternates 180 degrees with the adjacent rectangular area, and the phase of the matched load continuously changes from -180 degrees to 180 degrees. Note also that the measurements capture the fact that the in-plane electric field near one side of the microstip is pointing in the opposite direction of the in plane electric field on the opposite edge of the top strip. This result in the 180 degree phase difference between the top and bottom halves of Figure 22(d).

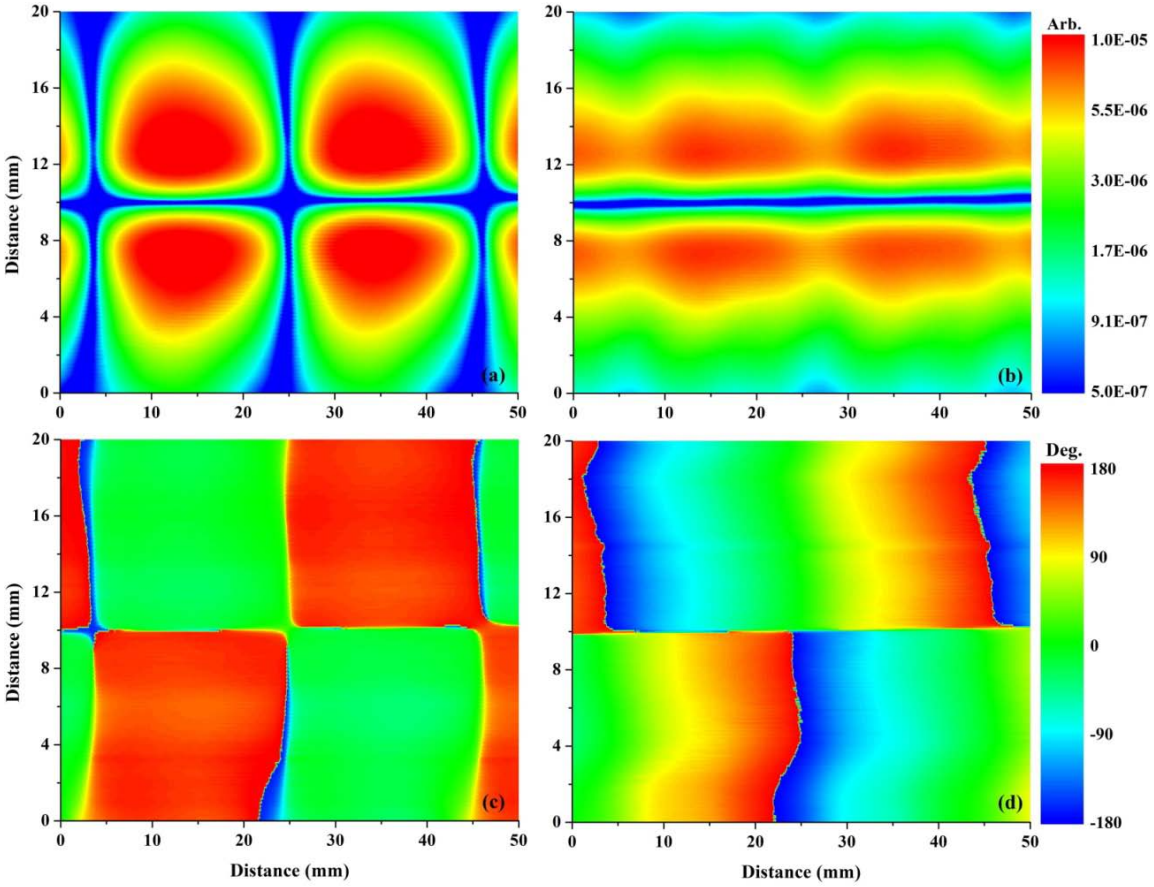

Figure 22 Experimental results of E_y amplitude for microstrip (a) open and (b) matched-load termination; E_y phase for microstrip (c) open and (d) matched-load termination.

Figure 23 shows the measured H_z magnetic field. Similar to the E_y field, both open and matched-load terminations show discontinuity since most of the magnetic fields are along the z direction. On the other hand, both open and matched-load terminations show the maximum amplitude at the edges of the transmission line where H_z is the strongest.

However, the H_z magnetic fields exist only close to the edge of the transmission line, and hence there is almost no field strength 4 mm away from the edge. This also explains why the phase patterns are noisy outside the range from 4 to 16 mm in Figure 23(c) and (d).

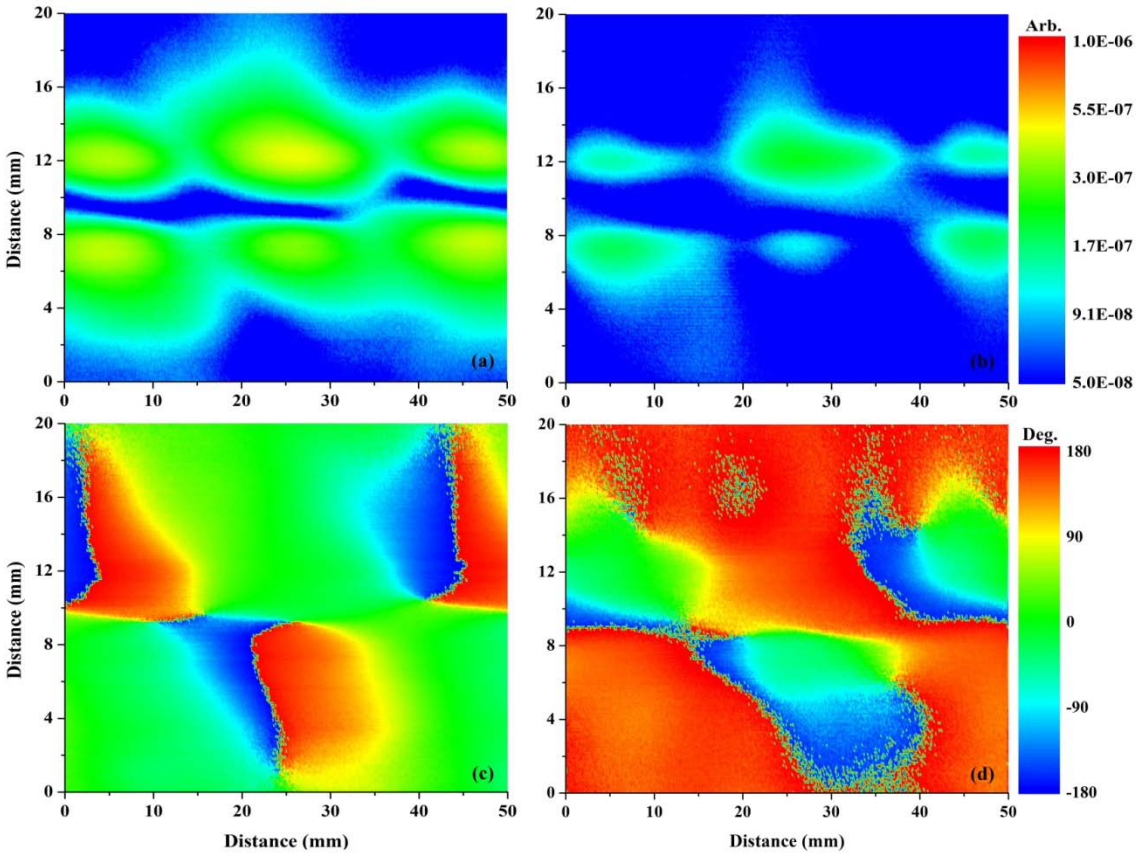

Figure 23 Experimental results of H_z amplitude for microstrip (a) open and (b) matched-load termination; H_z phase for microstrip (c) open and (d) matched-load termination.

Figure 24 shows the measured partial Poynting vector, P_x, calculated by the second term on the right hand side of Equation 70. Multiplying the amplitudes of the E_y electric field in Fig 22 and the H_z magnetic field in Fig 23, the partial P_x amplitudes for open termination and matched-load conditions are plotted in Figure 24(a) and (b), respectively. The amplitudes for the open and of matched-loads clearly show a gap at the center of transmission line. At the edges of the transmission line, the 5 nodes in the open-termination case are not as clear as in Figure 21(a) because the H_z magnetic field measurement in Figure 23(a) does not have two clear nodes at 14.8 and 35.4 mm. Moreover, the amplitude of the matched-load termination in Figure 24(b) only exists at

the edge of the transmission line, whereas Figure 21(b) shows a gap at the edge. Subtracting the phases of the H_z magnetic field in Figure 23 from those of the E_y electric field in Figure 22, the partial P_x phases for the open and matched-load terminations are plotted in Fig 24(c) and (d), respectively. The phase for the open termination again alternates 180 degrees at each node, while that for the matched load changes continuously.

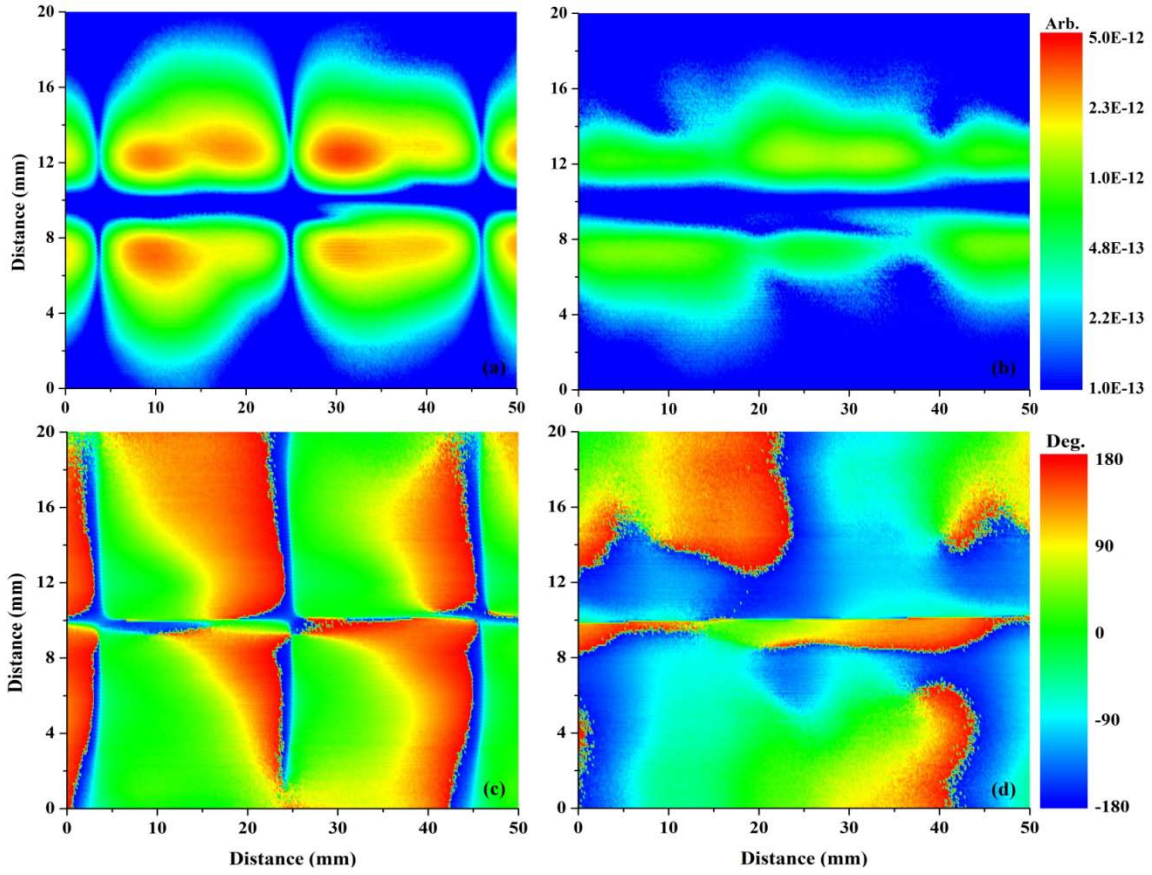

Figure 24 Experimental results of the second partial Poynting-vector amplitude for the microstrip with (a) open and (b) matched-load termination; partial Poynting-vector phase for the microstrip with (c) open and (d) matched-load termination.

The Poynting vector sum, the full P_x of Equation 70, is plotted in Figure 25 by combining the partial Poynting vectors from Figures 21 and 24. The amplitude distribution clearly indicates that the "matched" load condition in Figure 25(b) allows energy to flow along the microstrip in the x direction, whereas the open-terminated transmission line in Figure 25(a) has no continuous energy flow. The results in Figure 25

also quantitatively match an FEM simulation (run with ANSOFT HFSS software). Both simulation and experiment shows that the Poynting vector for the open-terminated line has a standing-wave pattern that is strongest at the edge of the transmission line, and the Poynting vector is continuously decreasing away from the center of the transmission line with the matched load.

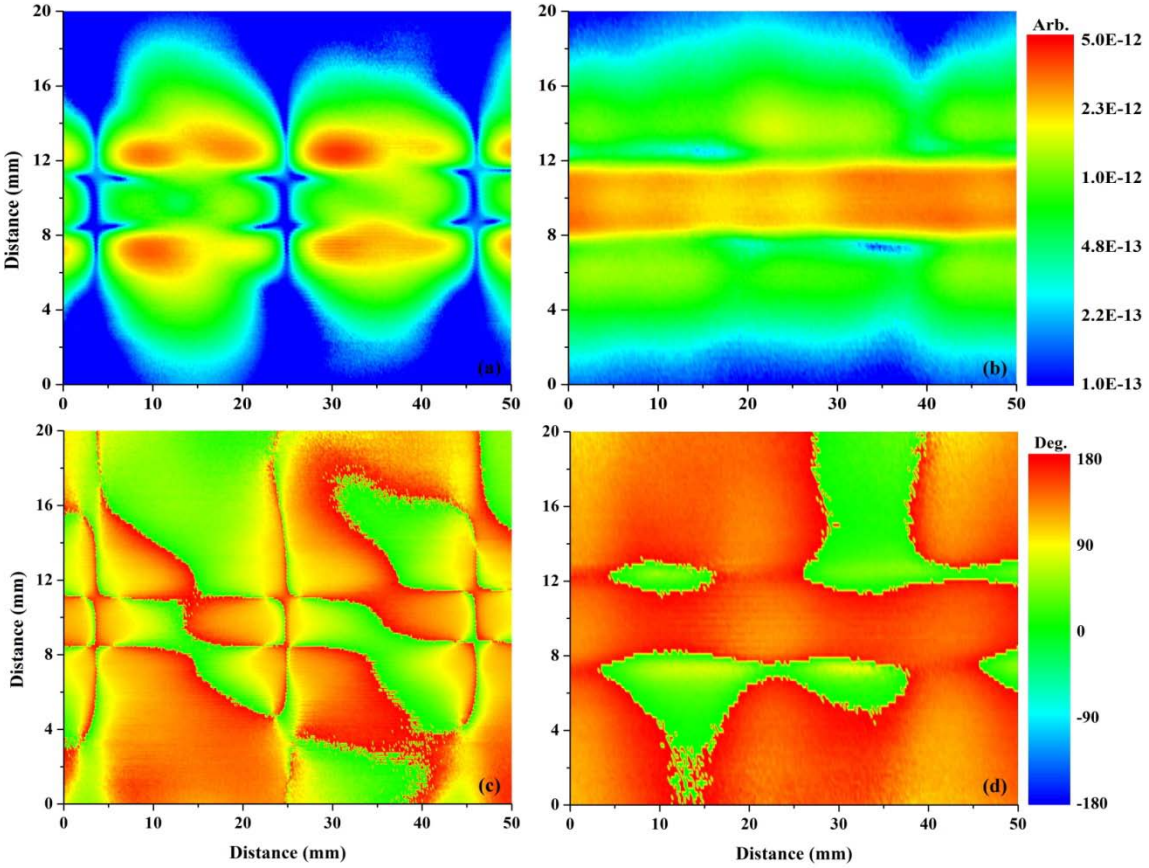

Figure 25 Complete Poynting-vector amplitude for the microstrip with (a) open and (b) matched-load termination; Complete Poynting vector phase for the microstrip with (c) open and (d) matched-load termination.

In order to better quantify the Poynting-vector maps, the phase (blue curve and circles) and amplitude (black curve and squares) along the center of the microstrip line are plotted in Figure 26. Figure 26(a) shows that the phase of the adjacent peaks of the standing wave amplitude pattern changes by 180 degrees, which is representative of a standing-wave pattern with no energy flow along the x direction. The 180º phase difference

appears at the positions of the electric and magnetic fields nodes in Figures 19 and 20. On the other hand, a propagating Poynting vector along the transmission line with a perfect matched load should have a constant phase and uniformly distributed amplitude. This is demonstrated in Figure 26(b). Due to the non-perfect matched load, the phase for the matched load termination in Figure 26(b) shows that the Poynting vector travels with a slightly varying amplitude and phase along the x direction, but still much more uniform than for the standing-wave case.

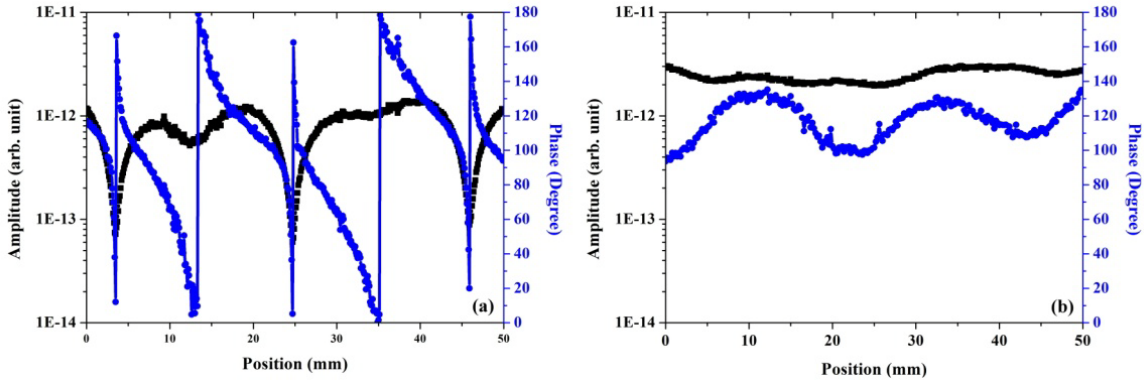

Figure 26 Experimental data showing the amplitude and phase variation of the Poynting vector versus probe position along the center of the microstrip terminated with (a) an open circuit and (b) a matched load.

3.4 Conclusions

In this chapter, a single <110> CMT crystal with a high-reflection coating on one side employed as a Poynting vector sensor is used. Compared to the reference crystals, the use of this multiple-birefringent CMT crystal demonstrates the ability to independently measure the electric and magnetic fields by precisely controlling the polarization angle of the probe beam. Properly mounting the CMT allows for the measurement of all components of an electric and a magnetic field. When all of the components of the electric and magnetic field are obtained, the energy flow of an EM wave can be subsequently mapped out without any transformational calculations based on the definition of the Poynting vector. Two different energy-flow cases for a 50-Ω microstrip transmission line, one with an open termination and the other with a matched load, have been successfully mapped out. The open-termination case shows no energy flow

according to both the acquired amplitude and phase information, whereas the matched-load case indicates energy flow along the microstrip transmission line. Refinement of this technique, such as with a fiber-based probe, could be used for the near field characterization of any device that radiates RF energy.

Chapter 4
Terahertz Electromagnetic Waves

Chapter 2 and Chapter 3 have demonstrated that CMT can be used as an EO or MO sensing medium in the microwave region. Since EOS syetem enables one to precisely resolve sub-picosecond nonlinear transient effects and characterize ultrafast electrical pulses, in this Chapter, CMT is used as an EO sensing medium in THz region.

Over the last several decades, broadband pulses of THz radiation have sparked many new forms of research due to their non-destructive and non-ionizing characteristics [43-45]. For example, terahertz time-domain spectroscopy has been widely used to investigate the physical properties of many nonpolar and nonmetallic materials such as ceramics, plastic explosives, and paintings, because they all exhibit spectral features in the terahertz region [46]. The material under study in this thesis is two ceramic samples where chapter 4 uses THz to investigate the surface defects and chapter 5 uses THz to monitor the subsurface defect growth.

4.1 Introduction to terahertz and current applications

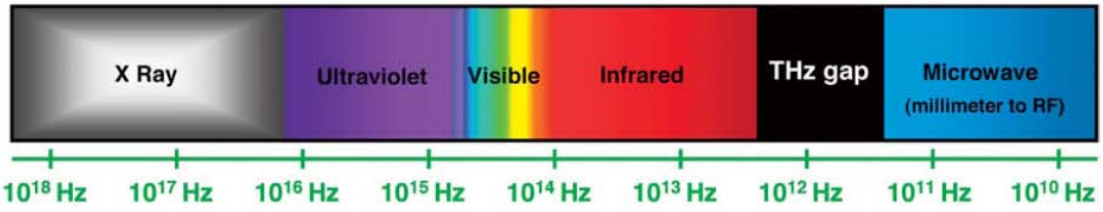

Figure 27 Representation of the electromagnetic spectrum illustrating the “THz gap” relative to the microwave and IR.[47]

The THz frequency band of radiation shown in Figure 27 lies between the far-infrared and microwave regions of the electromagnetic spectrum. The THz band is often defined from the range of 0.1 to 10 THz (1 THz = 10^{12} Hz) corresponding to a wavelength of 30

microns to 3 mm, and hence THz is sometimes referred to as the “submillimeter-wave” regime. Thus, terahertz radiation uniquely straddles the worlds of electronics and optics. Since lower frequency microwave radiation has lower photon energy, the waves cannot be measured directly, but can only be measured collectively by the electrical bias they induce in a detector. Infrared radiation, on the other hand, is optical, since its photon energy is large enough that individual photons can be measured.

In recent years, technology utilizing the THz spectral regime has significantly advanced, with widespread applications appearing in many areas, including electronic device inspection, medical diagnostics, and material science.[48] Terahertz-pulse imaging (TPI) is the technique that has drawn much attention and research effort due to its non-invasive and non-destructive characteristics. Moreover, TPI is advantageous because it utilizes a broad range of frequencies contained in a single pulse, providing spectroscopic and potentially diagnostic information that may not be found in other modalities. By analyzing the broadband absorption or reflection spectrum, layer thickness, constituents, and the refractive index of a medium can all be determined. The partially reflected THz pulses at the interfaces of different refractive-index media enable the detection of explosives, weapons, and illicit drugs beneath the clothing. In fact, THz radiation may ‘see through’ most non-metallic and non-polar media, which makes it a good safety-screening method. In this section, current TPI applications are briefly introduced.

With plastic explosives, fertilizer bombs, and biological agents becoming weapons of war and terrorism, more effective security screening to detect an increasing variety of threats is needed. By using the characteristic spectral response of many chemical substances and explosive materials in the THz region, most explosives, weapons and illicit drugs can be revealed by TPI examination.[49] These spectral features originate from molecular vibrational modes and intramolecular vibrations that cause sharp absorption peaks, allowing the material to be identified from a catalog of such “fingerpronts”.

TPI can also be utilized for improving the quality and uniformity of pharmaceutical products.[50] Many pharmaceutical materials can exist in multiple solid forms. These

polymorphic forms have the same chemical composition but different crystalline structures, and therefore exhibit different physiochemical properties such as dissolution and stability. These properties of all pharmaceutical products must be well documented and controlled for regulatory purposes, thus ensuring an ideal pharmacokinetic profile in the body can be achieved. Utilizing TPI, one pharmaceutical product with different polymorphism can be distinguished by identifying the crystalline phonon vibration. TPI can also be used to measure the thickness of tablet coatings, which have a variety of functions in the drug release process.[51] Moreover, during the tableting process, the distribution of the medicine may become nonuniform or have an incorrect structure, compromising the desired bioavailability and drug-release profile. Thus, when the thickness of a tablet is measured by TPI, the chemical map can also be obtained by looking at the spectral data set derived from the time-domain signal with a Fourier transform. Finally, the location of the chemicals in the tablet and the chemical identification can be both obtained by reconstructing a 3D chemical map.[52]

TPI can also be applied to biomedical applications. By detecting the differences in water content and density, TPI can detect epithelial cancer and teeth cavities.[53, 54] Without damaging tissue, TPI is safe, in fact safer than conventional X-ray imaging, due to the non-ionizing characteristic of its photon energies. In this chapter, TPI is employed as a non-destructive evaluation tool for detecting the surface defects of a ceramic sample where CMT is employed as the THz detector in this TPI system.

4.2 Terahertz generation and detection

4.2.1 Terahertz generation

Typical broadband THz radiation takes the shape of single-cycle pulses in the time domain. Extremely short THz pulses are usually generated by optical excitation in one of three media: a nonlinear crystal, an air-plasma, or a photoconductive switch. THz generation in a nonlinear crystal uses an optical-rectification process, which involves difference frequency mixing and occurs in an optical crystal with a large second order susceptibility, χ^2. In other words, the light of a given frequency, ω, passing through a nonlinear medium will generate the same amount of both sum and difference frequencies, corresponding to second harmonic, 2ω, and dc, ω-ω, respectively. Thus, the generated

THz pulse from the dc term is the envelope of the optical pulse. For ultrashort optical pulses that have a large bandwidth the frequency components are differenced with each other to produce bandwidths from near 0 to several THz.[55]

Terahertz wave emission from laser-induced plasmas, where the THz emission is perpendicular to the propagation of the optical pulse due to the acceleration of electrons and ions driven by ponderomotive force was observed for the first time in 1993.[56] Recently, efficient terahertz radiation has been observed when focusing a fundamental laser beam, ω, and its second harmonic, 2ω, into the air.[57] Studies show that strong terahertz radiation can be obtained through ionized air-plasma. The generation mechanism underlying this process can be explained by four-wave mixing among the ω, and 2ω beams in the plasma.[57, 58]

THz generation via optical rectification in a nonlinear crystal and four-wave mixing in ionized air-plasma can achieve higher THz power than using a photoconductive switch. However, optical rectification and four-wave mixing also require higher laser intensity and a more complicated alignment. Therefore, in this dissertation, photoconductive switching is chosen as the method to generate THz pulses.

A simplified schematic of the pulsed-THz generation process that employs a photoconductive (PC) switch is shown in Figure 28. An optically-actived semiconductor substrate, a biased coplanar-strip transmission line structure on the surface of the semiconductor, and a narrow gap between the transmission lines are the key elements in the operation of this device. The presence of the semi-insulating, semiconductor gap and the large dark resistivity of the substrate cause the nominal potential on the grounded cathode to remain well below the biased potential on the anode. However, electrons are liberated from the valence band to the conduction band in the semiconductor and the resistance across the switch is dramatically decreased if an optical pulse with appropriate photon energy is incident upon the gap. As a result, the potential on the cathode is increased and an electrical pulse is formed on the transmission line. The duration of the electrical pulse is governed by the charge carrier dynamics in the semiconductor plasma.

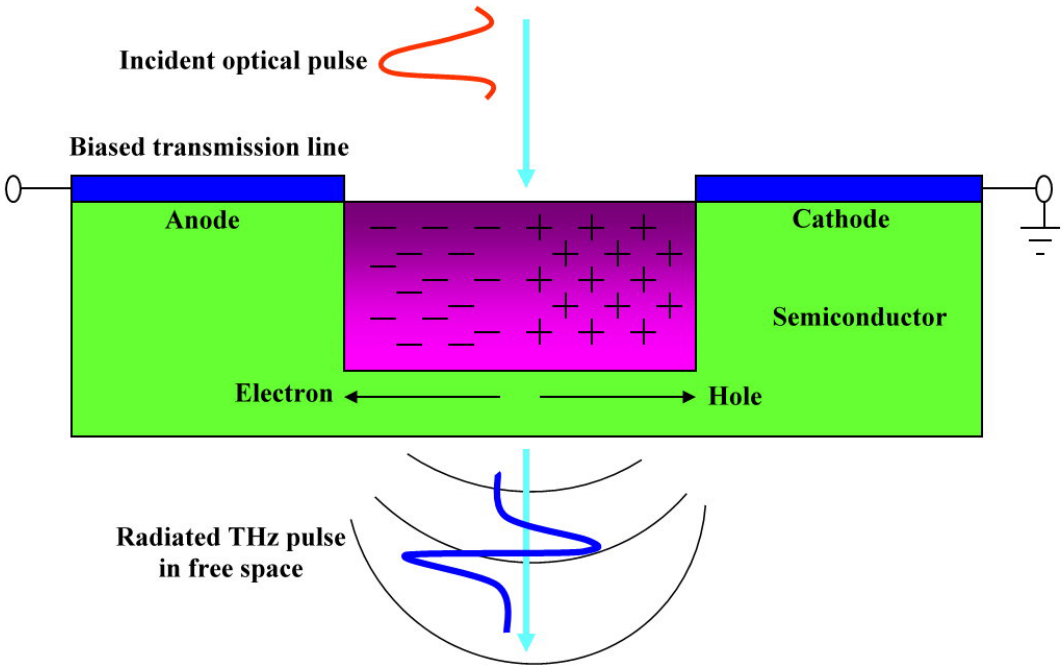

Figure 28 An ultrashort laser pulse illuminates a biased gap in a high-resistivity semiconductor within a coplanar strip transmission line (extending into and out of the page), generating an electron-hole plasma. The creation of the charge carriers along with their subsequent bias-field-induced acceleration produces a photo-current on the transmission line and a radiated electric field in the far field region of the emitter.

The carriers excited by the optical pulse recombine in the valance and conduction band or are trapped in mid-gap states (in the case of a heavily defected semiconductor like low-temperature-grown gallium arsenide), with a time constant for the latter given by the carrier trapping time, τ_c.[59] The time dependence of the carrier density, n, is given by the following equation:

$$\frac{dn}{dt} = -\frac{n}{\tau_c} + \delta(t) \tag{72}$$

where $\delta(t)$ is the rate of the carrier generation by the optical pulses. The generated carriers will be accelerated in the bias electric fields. The acceleration of electrons or holes in the semiconductor is given by

$$\frac{dv_{e,h}}{dt} = -\frac{v_{e,h}}{\tau_s} + \frac{q_{e,h}}{m_{e,h}} E \tag{73}$$

where e and h represent the electron and hole densities, respectively, $v_{e,h}$ is the average velocity of carriers, $q_{e,h}$ is the charge of an electron/hole, τ_s is the momentum relaxation time, $m_{e,h}$ is the effective mass of an electron/hole, and E is the local electric field. Due to screening effects of the space charges, the local electric field is smaller than the applied bias electric field,

$$E = E_{bias} - \frac{P}{3\varepsilon_0 \varepsilon_r} \tag{74}$$

where P is the polarization induced by the spatial separation of the electron and hole and is opposite to the external bias. In other words, after the photo-excited charge carriers separate, they produce an induced dipole moment within the bias field. The resulting space-charge distribution (due to both free and trapped carriers) serves to counter and screen E_{bias}, and the decelerating charge carriers radiate again. However, when the photoconductive gap is smaller than the center wavelength of the THz-pulse spectrum bias-field, screening becomes less significant and carrier dynamics dominate. Therefore, carriers will be accelerated as long as the local electric field and free carrier density are not zero.

Photo-excitation of the switch and the subsequent acceleration of the semiconductor charge carriers in the biased gap will create a time-varying photo-current, J. Using the Drude-Lorentz model, the photocurrent is given by:

$$J = env_e - env_h \tag{75}$$

The time derivative of this current maps itself onto the electric field in the far-field region of the emitter. If the photo-generation mechanism is fast enough, on a subpicosecond timescale for example, the frequency content of the radiated waveform can span into the THz spectrum. According to Hertzian dipole theory, the THz radiation is given by

$$E_{THz} \propto \frac{dj}{dt} = e(v_e - v_h)\frac{\partial n}{\partial t} + en(\frac{\partial v_e}{\partial t} - \frac{\partial v_h}{\partial t}) \tag{76}$$

Therefore, the first term on the right hand side of Equation 76 represents THz radiation due to the carrier-density change and the second term represents THz radiation due to the acceleration of the carrier under the electric field.[60]

For Hertzian dipole emitters, the power can be scaled up, while carrier saturation and material break down can be avoided, by increasing the size of the photoconductive region. This, however, also shifts the spectral energy of the terahertz pulse to lower frequencies. In this dissertation, an interdigitated-finger-electrode design shown in Figure 29 minimizes this spectral shift, because the active region for a pair of electrodes is 5 μm.[61] Each photoconductive gap then becomes a source of a terahertz pulse. Since the polarity of the bias field alternates with each electrode pair, the net E_{THz} amplitude approaches zero when a large area of the antenna is illuminated. However, when every other gap is shielded by a metalized opaque layer, the temporally coherent electric fields become additive, thus yielding a wider-bandwidth, higher energy THz-pulse.

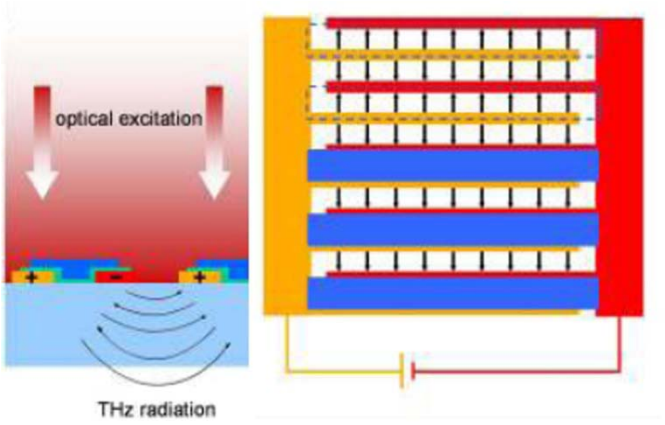

Figure 29 An interdigitated-finger electrode design for THz emitter from Gigaoptics. An optically opaque metal layer (blue) is applied between every other finger pair such that optical excitation is only possible in areas exhibiting the same electric field direction.

4.2.2 Terahertz detection

Both a Hertzian dipole PC switch and an optical anisotropic crystal were used for detecting THz radiation in this dissertation work. The mechanism of employing an optical anisotropic crystal to detect THz is described in section 1.2 and 1.3.[62, 63]

Therefore, this section will briefly discuss the mechanism of using a PC switch to detect THz radiation.

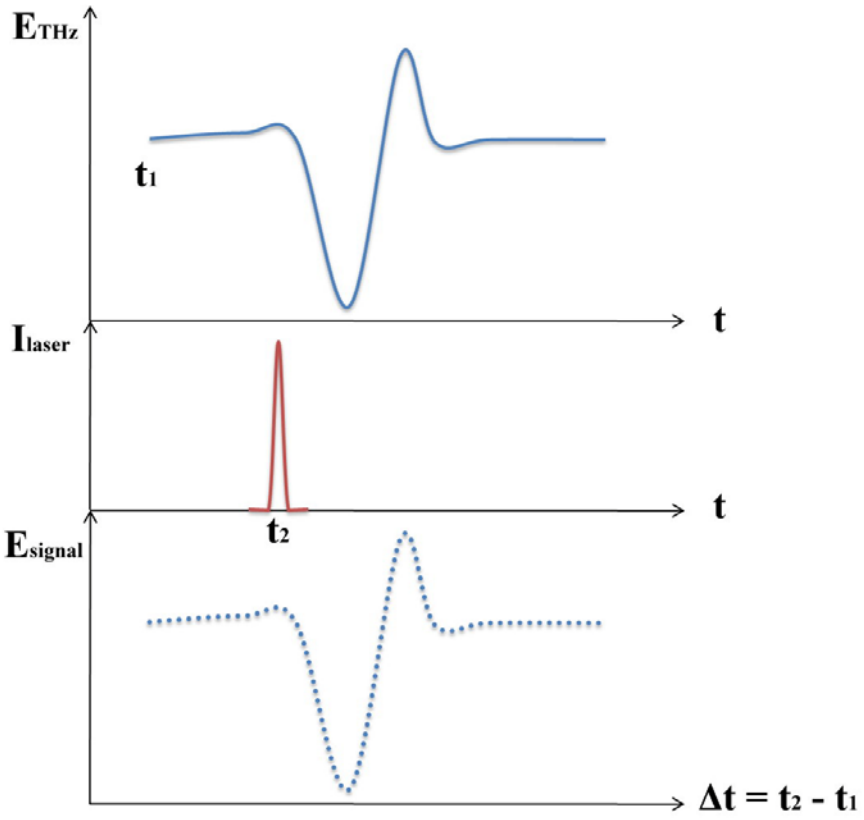

Figure 30 Time-domain THz electric field sampling via pump-probe experimental setup.

When an optical-pulse-excited PC switch is used for the THz receiver, the optical pulse generates photo-carriers in the receiver by the same photoexcitation mechanism as described in the last section. The incident electric field of the THz-pulse causes a time-varying potential to develop across the receiver, thus serving as an applied voltage bias that induces a transient photocurrent, J_d.

$$J_d(t) \propto \int_{-\infty}^{\infty} E_{THz}(t) n(t-\tau) dt \tag{77}$$

where $n(t-\tau)$ is the carrier response function of the semiconductor and is proportional to the laser optical pulse envelope. The shorter the carrier trapping time and narrower the laser pulse, the more accurate the measured terahertz signal will be, i.e., closer in

appearance to the radiated THz-pulse. There is also a presumption here that the capacitance of the sampling-gate switch-gap is not so large as to cause a limitation in the detection bandwidth.

For THz detection, a PC switch or a crystal is employed as the THz receiver for the time-domain pump-probe sampling system as described in section 1.6. The pump-probe sampling system requires the pulsed laser beam to be split into two paths, one for the pump and one for the probe, as shown in Figure 7. The THz-beam path becomes an extension of the optical pump beam path, which must both spatially and temporally overlap with the receiver. (Detailed experimental configurations will be shown in section 4.3 for crystal detection and section 5.3 for PC detection.) One of the beam paths has a variable optical delay which enables the sampling of the temporal profile of the THz-pulse by changing the optical path length, $\Delta z = \Delta t \cdot c$, where z is in the direction along the optical delay path.

4.3 Defect detection

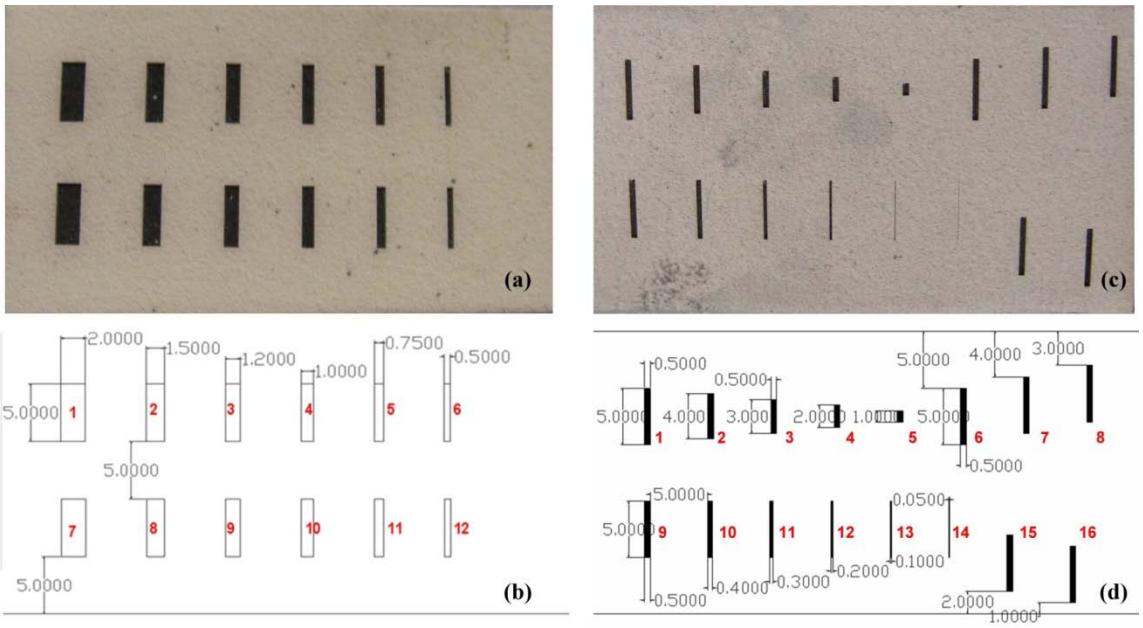

Figure 31 Two ceramic samples used for surface defect measurements: (a) optical image and (b) corresponding computer-assisted drawings of twelve laser-machined slots of equal depth and length, but decreasing width; (c) optical image and (d) corresponding

computer-assisted drawings of top row, laser-machined slots of equal depth and width, but varying length; bottom row, slots of equal length, but varying width and depth.

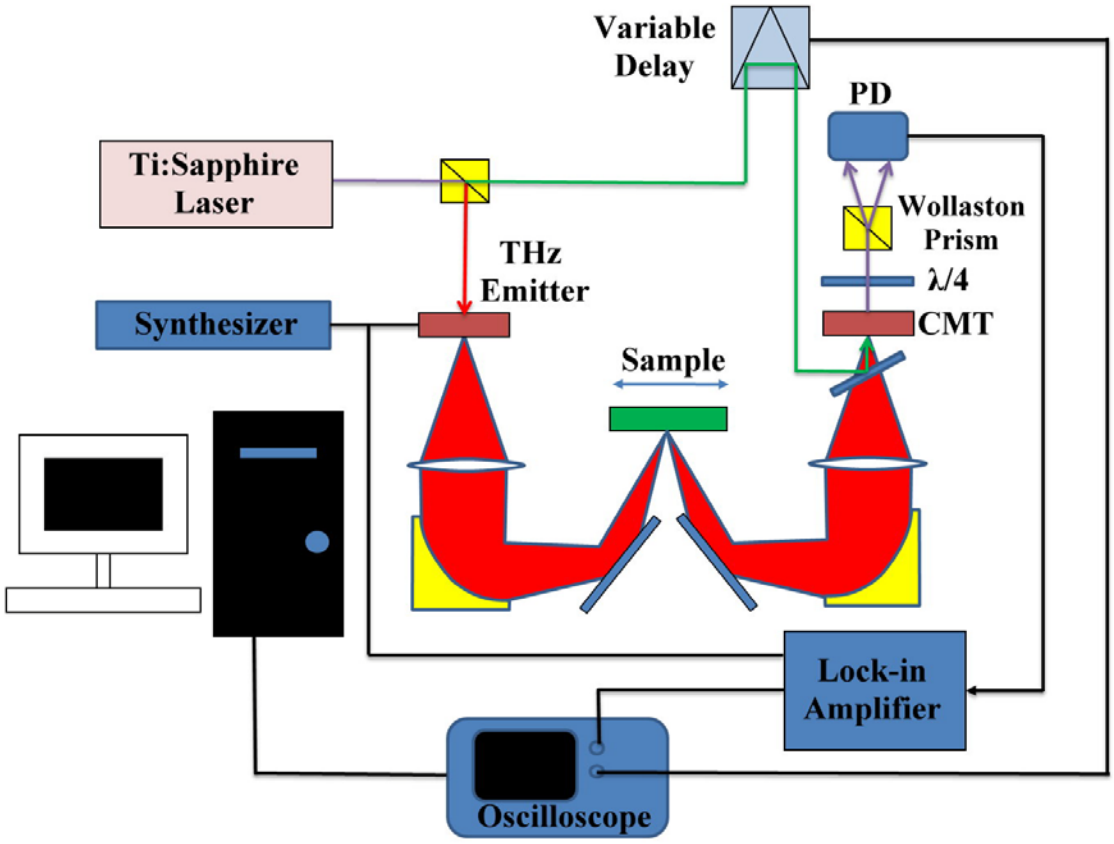

Figure 32 Schematic of a time-domain THz pump-probe sampling system. The pump path is marked in red which has equal distance as the probe path marked in green. Although both optical pump and THz beam path are marked in red, the optical pump path is represented by the line, while THz beam path is represented by the filled area.

In this section, TPI is used to examine the surface defects of two ceramic samples as shown in Figure 31. The TPI system is shown in Figure 32, where a PC switch is used as the THz emitter and a CMT crystal is used as the THz receiver. CMT is employed as an EO sensing crystal by measuring only the THz electric filed with the utilization of the Wollaston prism and quarter waveplate. The laser source is centered at 800-nm wavelength with a 100 fs pulse width (10 nm spectral bandwidth) and an approximately 80 MHz repetition rate pulse train. The variable delay is a retro-reflector oscillating up to 100 Hz, permitting a maximum 320 ps sampling window with a minimum 70 fs time

resolution. This time resolution can be problematic when attempting to identify sharp spectral fingerprints of materials. However for imaging applications, this variable delay permits fast waveform data acquisition, and in fact, it is possible to acquire up to a hundred thousand pixels per minute or the averaging of many waveforms to increase the signal to noise ratio of the terahertz signal. The lock-in amplifier detects signals only at the modulation frequency from the synthesizer that also served as the bias to the THz emitter.

The sample was translated in 100 μm increments across the focal plane of an approximately 1.7 mm FWHM terahertz beam spot. The spatial profile of the sample surface was calculated by integrating the spectrum of the front surface reflection between 0.2 and 3.0 THz.

$$\int \left| \mathcal{F}\left\{ E(t)\Big|_{t_a}^{t_b} \right\} \right|^2 dv \tag{78}$$

This method of analysis can be beneficial when the THz-beam spot size is larger than the features of the surface defect such that the local averaging of the reflected signal does not result in a detectable or significant time delay between the surface and internal layer reflections. By filtering out the lower spatial frequencies of the THz-beam spot, smaller spatial features can be resolved.

Sample 1 shown in Figure 31(a) is not in the field of interest in this Chapter because the narrowest slot width is 500 μm, which is larger than the wavelength of 1THz, and hence the slots can be easily detected, even by human eyes. However, sample 1 was oxidized at 1100 ºC and used for the subsurface defect detectiondescribed in the next chapter.

In this section, sample 2, as shown in Figure 31(c) is used to test the limitations of the TPI system resolution in the detection of surface defects. The narrowest slot width on the surface, as shown in Figure 31(d), is 50 μm, which is beyond the diffraction limit of a beam of pulses with frequency content at 1 THz. Given the diffraction limit, 300 μm, of 1 THz, one would expect that 50 μm is not resolvable by using a THz signal with low frequency. However, the experimental results in Figure 33 demonstrate that when the

time-domain and frequency-domain windows are properly chosen for the THz signal, according to Equation 78, the slots can be clearly observed. The numbered valleys correspond to the same numbered slots in Figure 31 where seven slots are clearly covered in this 4-cm-long one-dimensional scanning, and the 50-μm slot is numbered 14.

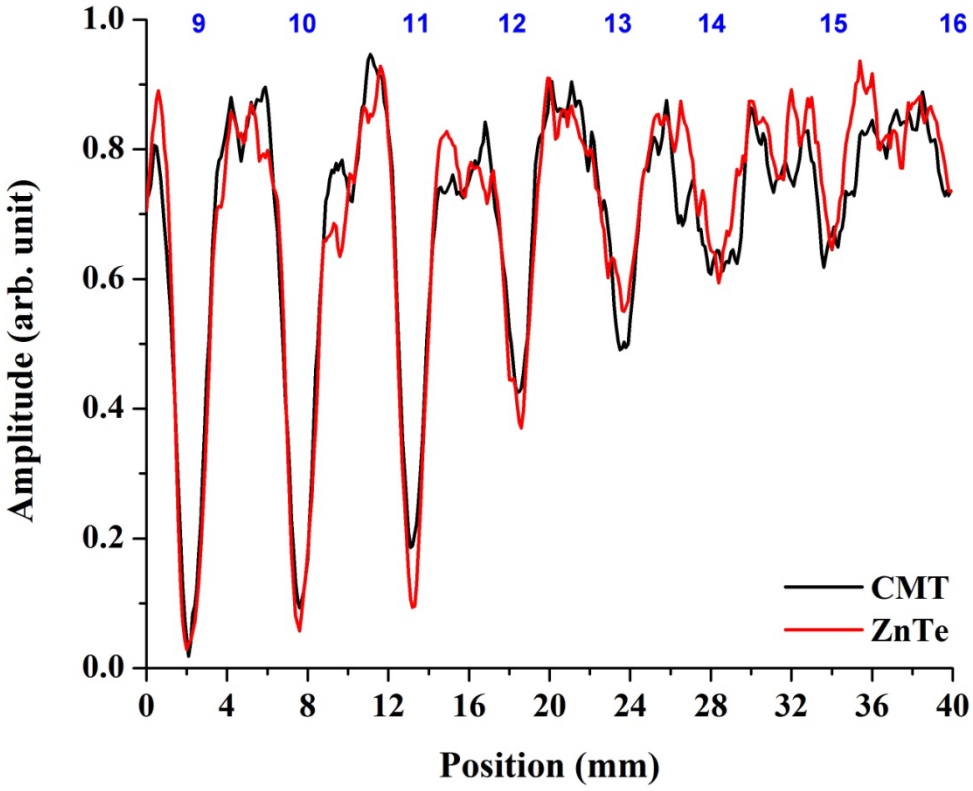

Figure 33 Experimental results of the slot positions via a one dimensional scan using the reflection-mode TPI system (for the sample in Figure 31(c) above).

Again, a reference EO crystal, ZnTe, which is commonly employed as a THz receiver at an 800-nm probe wavelength, is used to compare the data measured by the CMT crystal in Figure 33. Both crystals demonstrate the ability to clearly identify the 50 μm slot. However, the ZnTe crystal appears to show better resolution, since the measured slot width is resolved to be narrower than when using the CMT. This is because the ZnTe crystal has less absorption than the CMT crystal in the higher THz frequencies. Specifically, the CMT crystal shows less transmission at frequencies between 1 to 2 THz in Figure 34, which displays the transmission spectra of CMT and ZnTe crystals measured between 0 and 5 THz using a set-up essentially the same as that in Figure 32

(with the sample plane replaced with a metal reflector). Given that the higher frequencies are represented by shorter wavelengths, therefore, increasing shorter wavelength components also leads to better resolution.

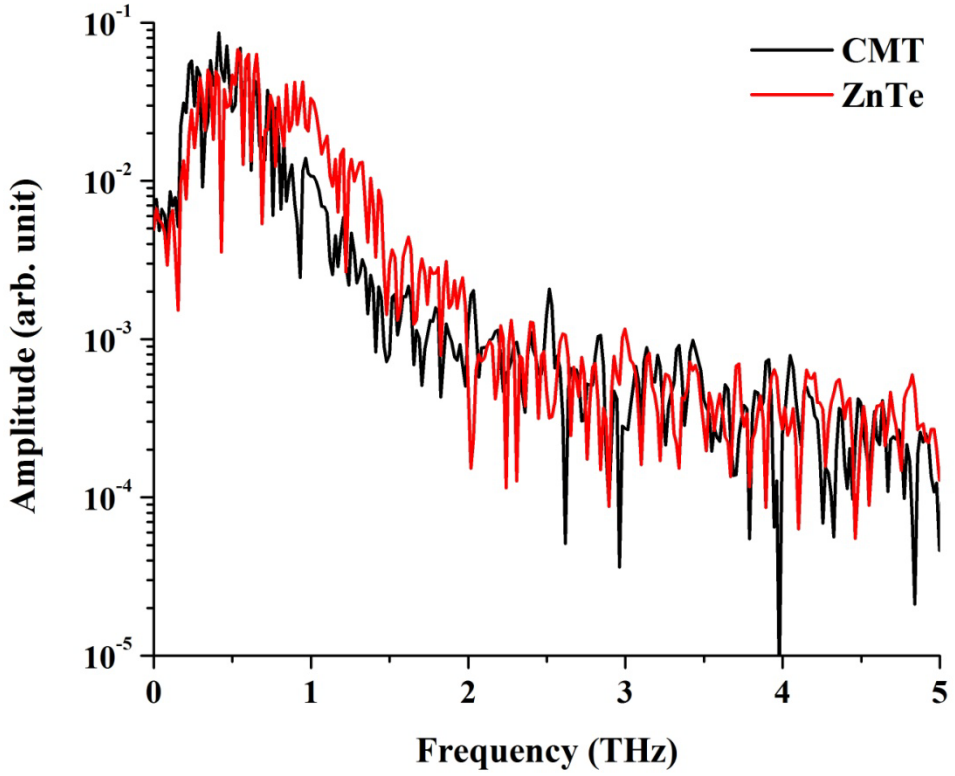

Figure 34 THz transmission spectrum of the CMT and ZnTe.

Most slots have a depth between 330 μm to 340 μm, although the slot with width less than 100 μm has a shallower depth because the laser cannot machine all the way though the ceramic to the substrate. For example, because of its narrow slot width, the depths of slots 13 and 14 are only 245 μm and 150 μm, respectively. In fact, the depth of the valley should also be reflected on the amplitude scale in Figure 33, where the lower amplitude represents a greater depth of a slot if the slot width is larger than the diffraction limit of the THz wavelength. On the other hand, the amplitude of the valley cannot reflect the true depth, if the slot width is smaller than the diffraction limit of the THz wavelength. Since the center frequency of the THz spectrum demonstrated in Figure 34 is less than 1 THz, the slot depth, with a width narrower than 300 μm, cannot be fully resolved. This is the reason that the valleys of slots 12, 13, and 14 have higher amplitudes than those of the

slots 9, 10, and 11. In addition, the valleys of slots 15 and 16 have amplitudes different from slots 9, 10, and 11 even though their depths are about the same. This is because only a small portion of the THz beam was able to cover slots 15 and 16 during the one-dimensional scan. (The eight slots are not on the same horizontal level and hence a one dimensional scan cannot include all of them within the same THz beam area.)

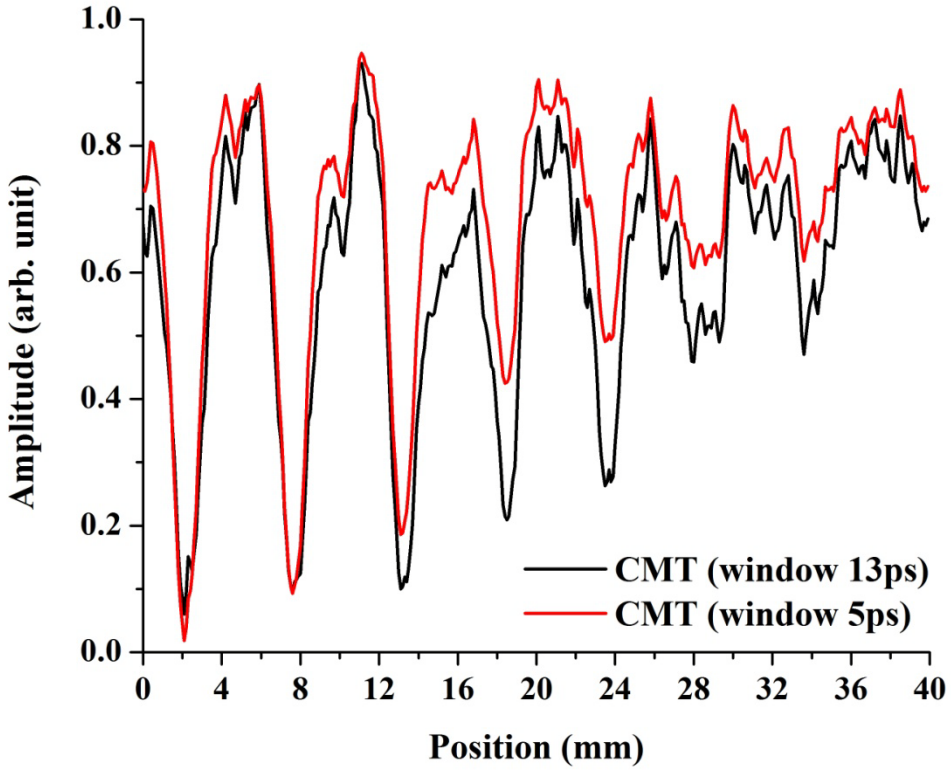

Figure 35 Experimental results of the slot positions via one dimensional scanning of TPI system with different time-domain window.

The flatness of the surface can also be measured by using the same analysis in Equation 78. Figure 35 shows the measured slot positions and surface flatness by using different time-domain windows for the post processing of the data. The 5-ps-window analysis demonstrates that the surface is relatively flat because the amplitude of the non-valley position marked in red remains at the same level, which is about 0.85. However, when a wider time-domain window, with a width of 10 ps, is used to analyze the same data, the amplitude of the non-valley position marked in black before 12 mm is higher than that after 12 mm. Therefore, the black line does not overlap with the red line. The

differences are due to the fact that the wider time-domain window includes the THz reflection from the bottom of the slots. (For a slot depth of 330 μm, the THz reflection from the bottom of the slot is delayed only 2.2 ps compared to the surface reflection.) In other words, the measured THz amplitude becomes the summation of reflections from surface and bottom of the slot, and hence it cannot be used to measure the flatness of the surface. On the other hand, a wider time-domain window has finer resolution in the frequency-domain and thus it can be used to increase the depth contrast ratio especially for the narrow slot width.

4.4 Conclusions

The TPI technique has been widely used by others for the analysis of biological materials, pharmaceutical products, and security screening due to its non-invasive, non-destructive and high resolution characteristics. Using these characteristics, a TPI system was built using a PC switch as the THz emitter and a CMT crystal as the THz receiver to measure the surface defects of a ceramic sample. The sample has different machined slot widths and varying depths. The narrowest slot width is 50 μm, and it is resolvable even though it is smaller than the diffraction limit of 1 THz. During the post-processing of the data, when a narrow time-domain window is selected, the amplitude of the THz reflection signal can be used as an indicator of the surface flatness. On the other hand, when a wider time-domain window is selected, a better depth resolution can be achieved for a slot width that is smaller than the diffraction limit of 1 THz. In addition, the THz transmission spectrum of the CMT is also measured and compared to the most commonly used EO crystal, ZnTe, at 800-nm probe wavelength. Although the results show that ZnTe has better transmission for higher THz frequencies, CMT has no phonon resonance below 2 THz and hence is a suitable EO crystal for THz sensing at moderate THz frequencies.

Chapter 5
Terahertz Time-Domain Reflectometry

If a material is measured in a reflection geometry, only a portion of the THz-pulse energy will be transmitted through the boundaries of different materials due to the differences in refractive index. The resulting reflections can be exploited to obtain spectral and spatial information about layers of materials or even elements within a system. This reflection-geometry experimental embodiment is known as terahertz time-domain reflectometry (THz-TDR), and it can be effectively used when performing spectroscopy, imaging, and ranging.

In this chapter, sample 1 introduced in chapter 4 is investigated by a THz-TDR system. Sample 1 was originally a three layers system; however, after placing it in a tube furnace for the oxidation process, new layers were formed and eventually caused the delamination of the top layer. This delamination process eventually leads to the system failure and hece the main focus of this chapter is to monitor those subsurface defect growths and use the THz-TDR system to nondestructively evaluate the sample life time.

Material thickness and refractive index are the two most common properties measured by THz-TDR. Using a generic two-layer system as an example, where layer 1 is a transparent dielectric and layer 2 is electrically conductive, Figure 36 shows the principal of the measurement of either thickness or refractive index of the dielectric. When the THz pulse is incident on the insulator's open surface, it is partially reflected at the air/dielectric boundary – due to the discontinuity in the group refractive index – and then totally reflected at the dielectric/metal interface. The time delay Δt between two pulses is given by

$$\Delta t = \frac{2 n_g d}{c \cos \varphi} \tag{79}$$

where n_g is the group refractive index of the dielectric in the THz region, d is the thickness of the dielectric layer, c is the velocity of light in vacuum and φ is the reflection angle at the metallic layer. According to Equation 79, the time delay can be used to determine the insulator-coating refractive index, if its thickness is known, or the layer thickness if one has knowledge of its refractive index. Using this time delay calculation, the ceramic sample in Figure 31(a) is being used for subsurface defects detection.

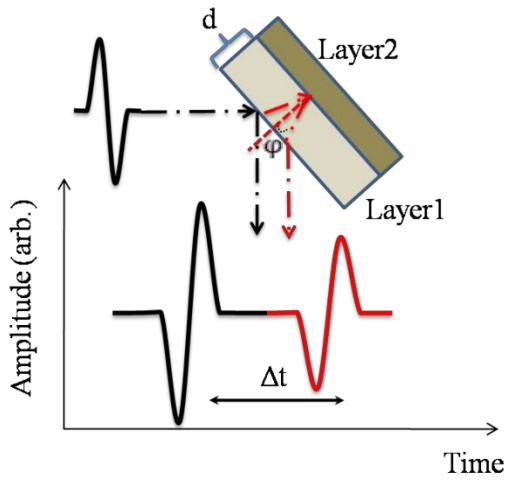

Figure 36 Principal of the thickness and group refractive index measurement via THz-TDR.

5.1 Background on thermal barrier coatings

Many organic, high explosive, polymer, and other materials interact with air, moisture, or heat during fabrication, storage, use, or shipping. This potentially leads to hardening, weakening, corrosion, or even failure. One critical material system that happens to degrade over time due to operation is the thermally insulating so-called Thermal Barrier Coating (TBC), a heat-protection layer that coats metal blades and other turbine components found in aircraft engines and power-generation equipment. This coating enhances the temperature differential between the air and the alloy, thus reducing the oxidation and corrosion of the alloy and protecting the physical integrity of the turbine blade, as well as increasing the lifetime, efficiency and reliability of turbine engines.

Common TBC structures usually contain three layers: a ceramic oxide, such as Yttria-stabilized Zirconia (YSZ), a bond coat (BC), and a Ni-alloy bulk substrate, as shown in

Figure 37. The BC deposited at the ceramic/Ni-alloy interface, typically containing Al and other elements, is used to promote YSZ adhesion to the Ni-alloy turbine parts. During operation, the YSZ layer, intentionally created to be slightly porous to maintain its integrity during thermal expansion and contraction, is penetrated by air, creating a thermally-grown oxide (TGO) of alumina, and consequently internal stress, between the BC and the YSZ. Stress levels are further increased during thermal cycling of the TBCs due to thermal mismatches among the bond coat, TGO, and YSZ. This mismatch creates voids in the YSZ coating and would eventually lead to delamination of the YSZ and failure of the coating and part [64-67], if the part was not taken out of service and re-coated. The failure of thermal-barrier coatings is taken very seriously due to the potential for performance degradation and the catastrophic threat to safe operating conditions. To address this potentially dangerous situation, reliable diagnostic tools to identify the severity and location of degradations within thermal-barrier coatings are vigorously pursued [68-70].

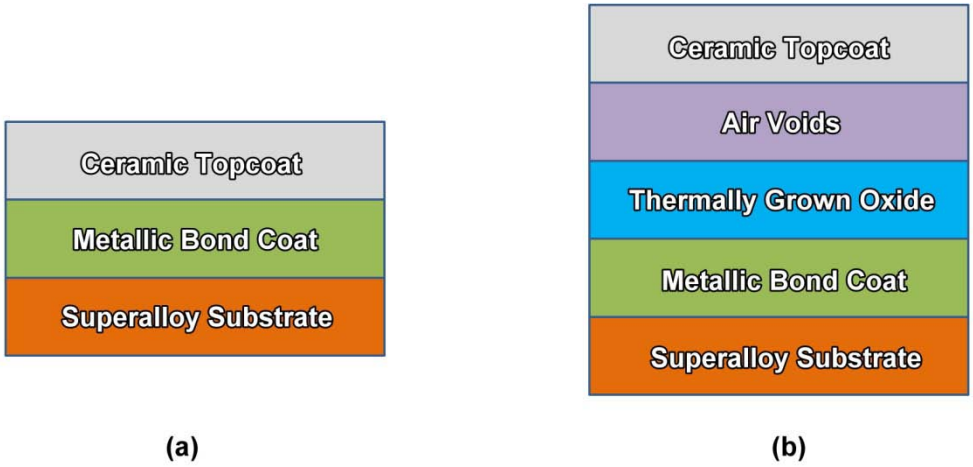

Figure 37 A block diagram of typical TBC structures (a) before and (b) after operating in an environment with high temperature.

Given that TBCs are relatively transparent to far-infrared radiation, THz-TDR was chosen to investigate the non-destructive inspection of the condition of the ceramic/metal interface during a variety of simulated service times at an appropriate elevated temperature [71, 72]. Compared to other nondestructive evaluation methods, THz-TDR utilizes pulses that penetrate better and are scattered less within typical TBC layers, such

as the one investigated here that was air-plasma-sprayed onto a rough surface of grit-blasted bond coat.

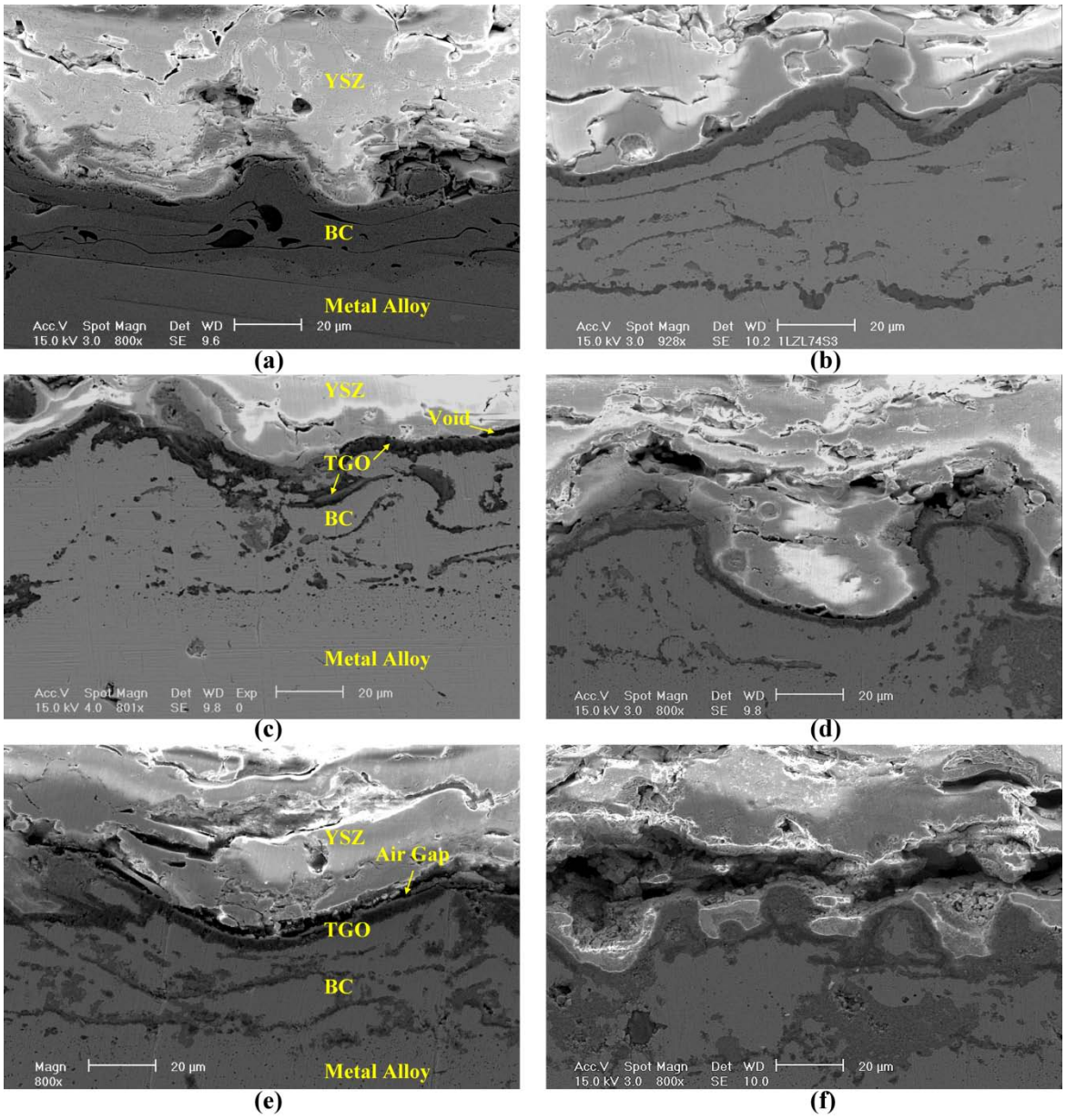

Figure 38 SEM images of the YSZ interface (a) before thermal cycling and oxidation, (b) after 100 hours, (c) after 348 hours, (d) after 790 hours, (e) after 1100 hours and (f) after 1350 hours at 1100 ºC. Each SEM image is taken at a different location along the cross-section of the multi-layer-sample material system.

In this chapter, time-of-flight terahertz measurements have been found to reveal the presence and growth of the thermally-grown oxide layer with a resolution on the order of

a single micrometer. This sensitivity to intermediate layers of various refractive index can then be used to monitor the progression of the buried air voids that ultimately lead to TBC failure. In Figure 37(a), which depicts a material system that has yet to undergo thermal cycling, the top layer is the YSZ ceramic and is transparent to the THz pulse, while the middle layer is the metallic bond coat, which totally reflects the THz pulse. The alumina TGO and the voids, as shown in Figure 37(b), would be additional intermediate layers appearing between YSZ and BC during thermal cycling.

The interface of the TBC sample is shown before oxidation in a scanning-electron-microscope (SEM) image in Figure 38(a). The air-plasma-sprayed TBC has a thickness of 300±50 μm, and the BC layer is 50±25 μm, where the thickness variations are local and frequent – around an average value within the area of the THz beam spot on the sample – and are not due to measurement uncertainty. Given the relatively large spot size of the THz beam, it is believed that the measurements yield information that is averaged over the thickness variations of the various material components. The YSZ/BC interface is very rough due to the fact that air-plasma-sprayed TBC samples require such a surface to reduce strain and premature delamination.

In order to monitor the oxidation process, the sample was heated in a tube furnace at 1100ºC for 1350 hours to simulate operational service time. Since spallation is the continuous evolution of damage in the TBC, with the BC oxidation process playing a key role in the formation and growth of microcracks, the sample was removed periodically to conduct the THz measurements and to cut a small piece from the edge of the TBC sample for the SEM interface inspection. After continuous thermal exposure for 100 hours, the TGO, which is the dark grey layer between the YSZ and BC, was formed as shown in Figure 38(b). The average TGO thickness, as suggested by Figure 38(c), rapidly increased with thermalization time to about 5 μm within the first 348 hours of exposure, before the rate of growth slowed. Infrequent small voids were initially observed in the sample that was thermally exposed for 348 hours and were typically found at positions where the TGO was non-planar, causing the YSZ to experience larger internal stress. The voids increased in number and size with the thermal exposure, as seen in particular in Figure 38(e). The air voids coalesced to form more uniform, nearly continuous gaps in the YSZ layer after 1100 hours in the tube furnace. After 1350 hours, the edge of the

YSZ layer seen in Figure 38(f) delaminated (where the delamination was not in view of the SEM). Due to polishing artifacts such as "pull-out" and chipping, and also as a result of epoxy-mount shrinkage that weakens interfaces, the void and interface gap sizes shown particularly in Figures 38(e) and 38(f) appear exaggerated beyond what would actually be present in the specimen before cross-section preparation.

5.2 Multilayer simulation

The SEM images show that the average thickness of the TGO and the air gap are on the order of several micrometers. According to equation 79, the time delay Δt between reflected THz pulses for a few-micrometer thickness should be less than 1 picosecond at the YSZ/Air, Air/TGO, and TGO/BC interfaces. Compared to the original THz pulse width of ~3 ps, the time-domain signal is thus expected to be a single pulse, comprised of a superposition of multiple reflected pulses, as compared to a series of distinct, consecutive pulses in the time-domain.

In order to better interpret the reflected THz-pulse behavior, a time-domain simulation of the multilayer conditions observed in the SEM images was conducted using a Fresnel-reflection analysis with lossless, non-dispersive layers and a realistic THz incident transient, which had a frequency content ranging from 0.2 to 1.5 THz [14]. A digitized version of a measured THz input pulse was used as the input to the Fresnel-reflection algorithm. With the initial reflected THz pulses from the air/YSZ interface aligned so that they were always coincident in time, the positions and shapes of the second reflected THz pulse from the internal multilayers for different interface-layer-thickness conditions were computed (Figure 39). The simulation assumed idealized dielectric layers of uniform thickness. The red line in Figure 39 represents the THz signal with no interface oxidation (or additional interface layers), the black line is the THz signal reflected from the YSZ/TGO and TGO/BC interface system, and the blue and green lines simulate the interface with additional air gaps between the YSZ and TGO. Multiple reflections within the relevant surfaces were observed to delay and either narrow or broaden the THz interface reflection, due to the superposition of numerous round-trip THz signals, some which experience π-phase shifts upon reflection and some that do not.

Inclusion of the internal reflections from the larger air-filled voids also appears to damp out the last noticeable oscillation in the interface reflection of the THz signal.

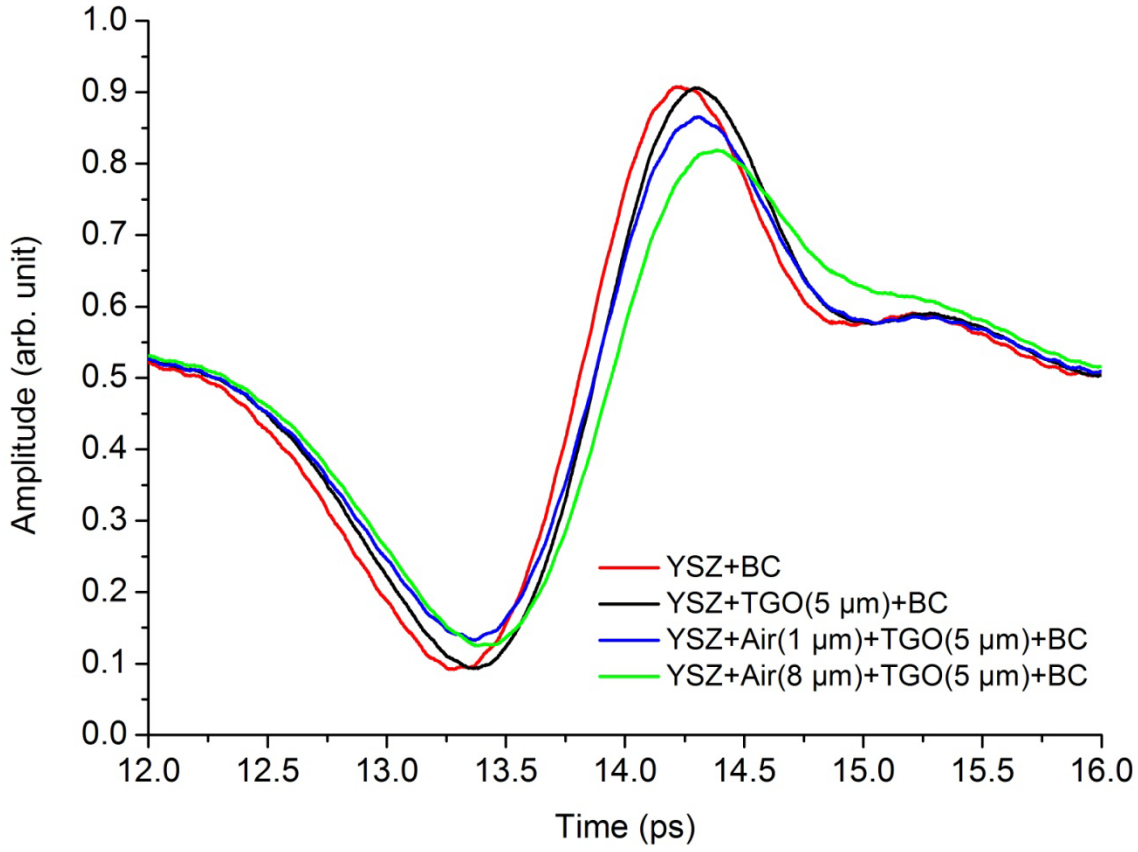

Figure 39 Simulation results of the reflection of a THz-pulse from the TBC/BC interface for different interface conditions.

The delay between the YSZ front-face reflection and the internal-interface compound reflection was quantified by considering both the negative-valley-to-negative-valley time difference for the two reflections, as well as their positive-peak-to-positive-peak time difference. The time delays of these components from the second THz-pulse reflections, simulated from the idealized interfaces in Figure 39, were thus reduced and plotted against the hypothesized accumulated sample heating times in Figure 40. Four data points for both the pulses' negative and positive peak shifts are given for four different sample conditions: YSZ+BC, YSZ+TGO(5μm)+BC, YSZ+Air-Gap(1μm)+TGO(5μm)+BC, and YSZ+Air-Gap (8 μm)+TGO (5μm)+BC, corresponding to increasingly long thermal exposure times. The delays of the negative and positive

components both increase together as the TGO becomes thicker, up until the voids begin to appear at the 348 hour mark. This is plausible, considering the fact that the refractive indices of the YSZ and the TGO are similar, so that the largest reflections should arise at the YSZ front face and at the TGO/BC interface. (The refractive index for YSZ is 4.5, as shown in the next section, and the refractive index for TGO is expected to be 3.5 for frequencies between 0-3 THz [73].) Thus, as the TGO grows, the two dielectric layers of YSZ and TGO act basically as one continuously thickening layer, and the entire THz-pulse reflection is delayed with respect to the reflection from the front-face.

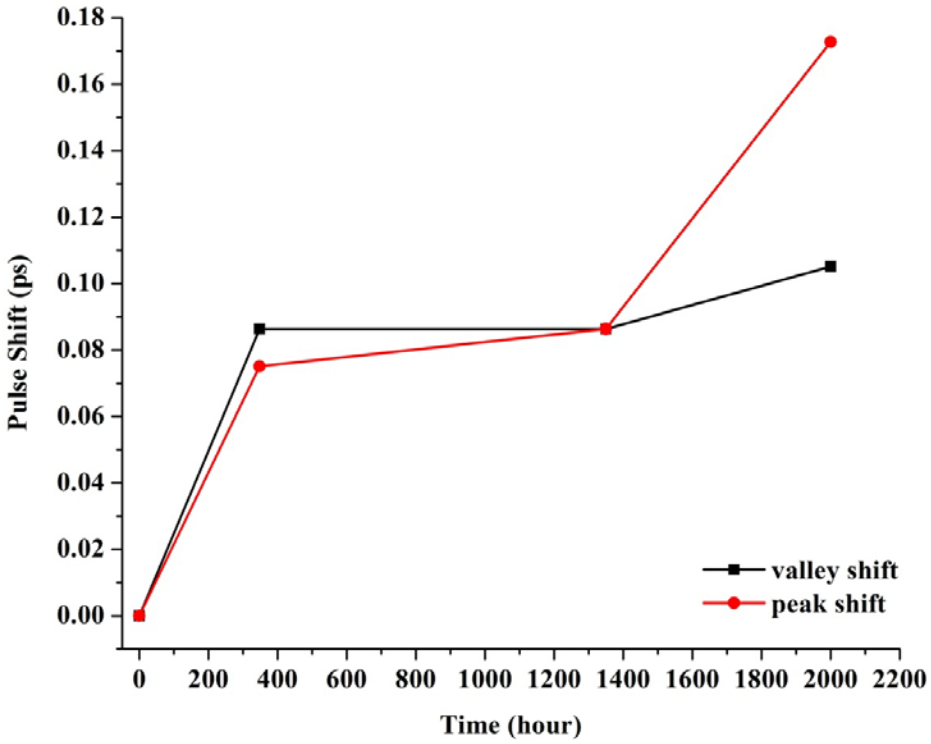

Figure 40 The delay time of the second reflected THz pulse from simulation versus the heating time in furnace.

The TGO growth rate slows as the voids begin to form, although it mostly still increases with thermal exposure as observed in the SEM images. In this range, despite the increasing thickness of the TGO/void layers and the eventual formation of uniform air gaps, the delays of the THz-pulse negative and positive peaks essentially cease increasing. It appears that this happens due to a trade-off that develops between competing mechanisms. One is an increasing THz-pulse delay from the increasing thickness of the

total interface-layer. The other is that multiple reflections at the multi-dielectric interface, some of which are π-phase-shifted with respect to each other (due to the refractive indices present), become superimposed when they contribute to the overall THz-pulse reflection from the internal-interface. That is, when all the THz-pulse reflections, phase shifts, and time delays are taken into account by the simulation algorithm, both the negative and positive peaks exhibit very small shifts with respect to each other, up until the point where the air gaps become very large (and delamination occurs). The simulation results also show that the multilayer system with the large, delamination-like air gap broadens the pulse width dramatically (with the positive part of the pulse delayed from the incident pulse more than the negative part), and the contrast ratio between the peak and valley of the combined reflected THz pulse is reduced because of the deconstructive interference. As the air gap increases in thickness, the THz-pulse reflection from the YSZ/air-gap interface is separated from the other multiple reflections, and the increasing separation of the multiple reflections causes the time-domain tail of the THz pulse to rise (as seen in Figure 39).

5.3 Thermally-grown-oxide monitoring

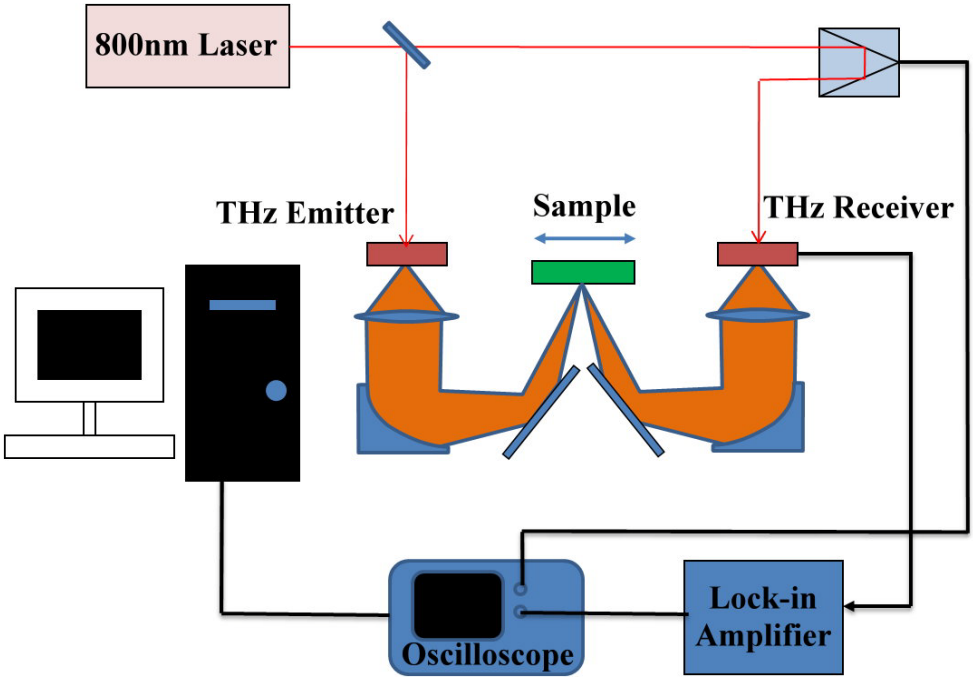

Figure 41 THz-TDR experimental schematic.

For the THz-TDR experiments, a conventional THz-imaging system as shown in Figure 41 was employed, utilizing low-temperature-grown GaAs emitter and receiver elements driven by 80 fs laser pulses (800 nm wavelength) at an 80-MHz repetition rate. The TBC sample was placed on a motorized translation stage to perform line scans and investigate sample uniformity using THz pulses with bandwidth between 0.2 and 1.5 THz.

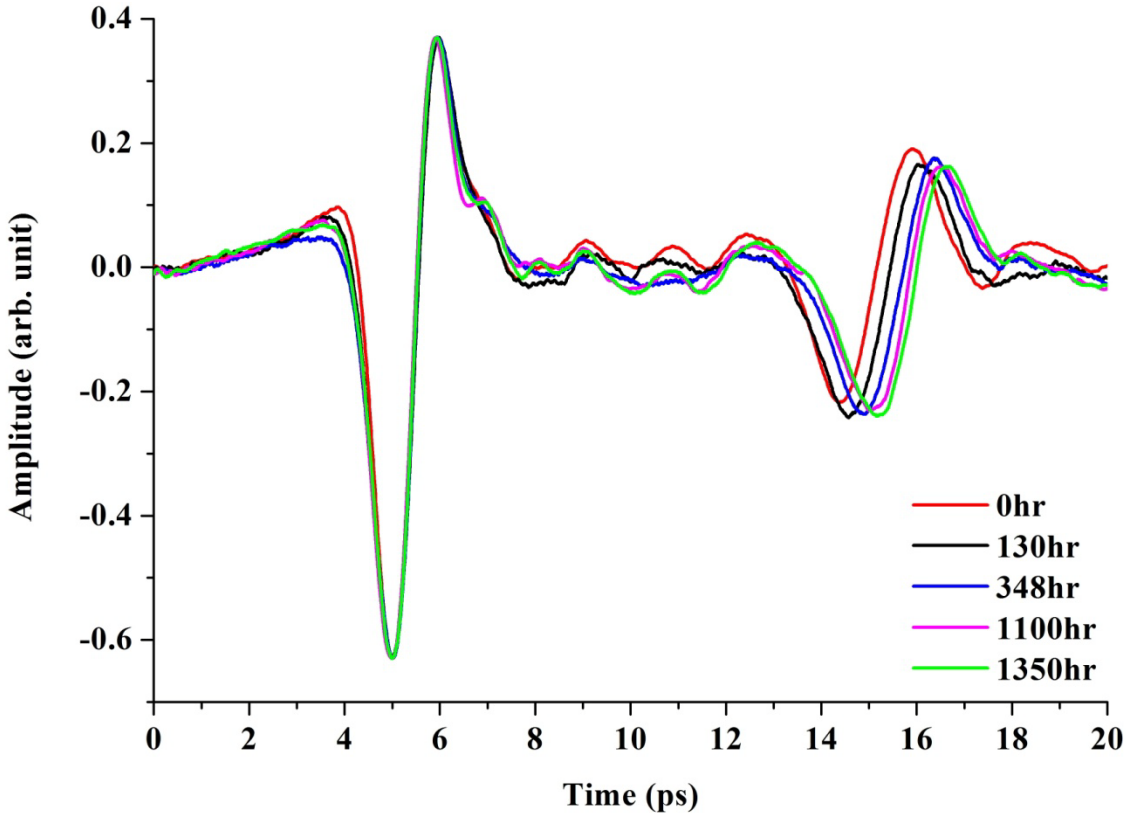

Figure 42 Experimental reflected THz transients for a sample heated at 1100 ºC for five different accumulated thermal-exposure times between 0-1350 hours.

The TGO and void formation were detected by comparing the delay of the second THz-pulse peak, reflected from the internal interface, with the initial THz reflection from the TBC top surface, as shown in Figure 42. The red line represents the THz signal before the BC on the TBC sample was oxidized, with the delay of the second THz pulse being caused only by the extra optical path inside the YSZ layer. Up until the voids were observed at 348 hours, the interface-reflection transition (*i.e.*, falling) edges starting at about the 13 ps point in time of Figure 42 are all virtually aligned, as one would expect for a TBC-layer thickness that did not change with thermal exposure. The virtually

aligned falling edge was observed in multiple samples for as many as five occasions of thermal cycling up to the 348-hour exposure point, although only one thermal cycling time, 130 hours, is shown in Figure 42. However, when the THz pulse encounters the TGO "etalon," the remaining elements of the THz transient, starting at about 14 ps, are delayed. Furthermore, the additional etalon formed by the voids for heating times in excess of 348 hours leads to a delay even in the transition edge, as shown in Figure 6, for the longer thermal-exposure times. The rate of the pulse delay-time increase began to slow after 620 hours, corresponding to the average enhancement of the TGO thickness also exhibiting a decreased rate.

The YSZ thickness is 310 ± 30 μm, which is provided by the manufacturer, Mound Laser and Photonic Center, and confirmed with the thickness measurement from SEM images. Substituting the YSZ thickness into Equation 79, the refractive index of YSZ was calculated to be 4.5±0.4 from the delay of 9.37 picoseconds in the 0.2-1.5 THz range where the incident angle is only 5 degrees, and hence the cosine value is close to 1.

The THz-TDR experimental results indicate a larger pulse delay in time compared to the simulations in Figure 39. This is likely due to the assumptions inherent in the simulation of ideal conditions, *i.e.,* the simulation considered neither scattering effects inside the porous ceramic oxide nor the roughness of the interfaces across the whole layer. However, the experimental results qualitatively follow the simulation in its time-delay trends and the changes in pulse shape. Comparing the purple and green lines of the experimental results in Figure 42 with the green curve of the simulation data in Figure 39, the gradually damped oscillation becomes more obvious with the increasing time spent by the sample in the furnace. Based on the simulation results, the damped oscillation originates from the separation of the multiply-reflected THz pulses, the results indicating that the air gap or the TGO thickness is large enough to cause a separation in the internal reflection at the YSZ/air-gap and air-gap/ TGO interfaces.

The delays in the negative valleys and positive peaks of the second THz pulse after the round-trip through the TBC sample of the THz pulse are plotted against the accumulated sample heating times and presented in Figure 43. The differences in the valley-to-valley and peak-to-peak delay times demonstrate that the second reflected THz pulse appears to narrow after 348 hours. Additional pulse narrowing, which can also be confirmed from

the change in the slope of the negative-to-positive transition in the THz transient as shown in Figure 42, occurs with the increasing thermalization time up to 1100 hours. The pulse narrowing effect is hinted at by the simulations, but not at all to the degree seen in the experiments. However, the uniform THz-pulse delays observed during the air-void and then air-gap formation did appear to change dramatically, as suggested by the simulation, after 1100 hours exposure time, due to the air gap being large enough to separate the reflected pulse at the YSZ/air-gap boundary from the other internally reflected pulses. This pulse separation can also be confirmed from the experimental THz time-domain signal of Figure 42, where the damped-out oscillation of the green curve has only two small peaks at the end of the trace. The increasing delay time with thermal exposure and TGO/void growth was confirmed for multiple TBC samples.

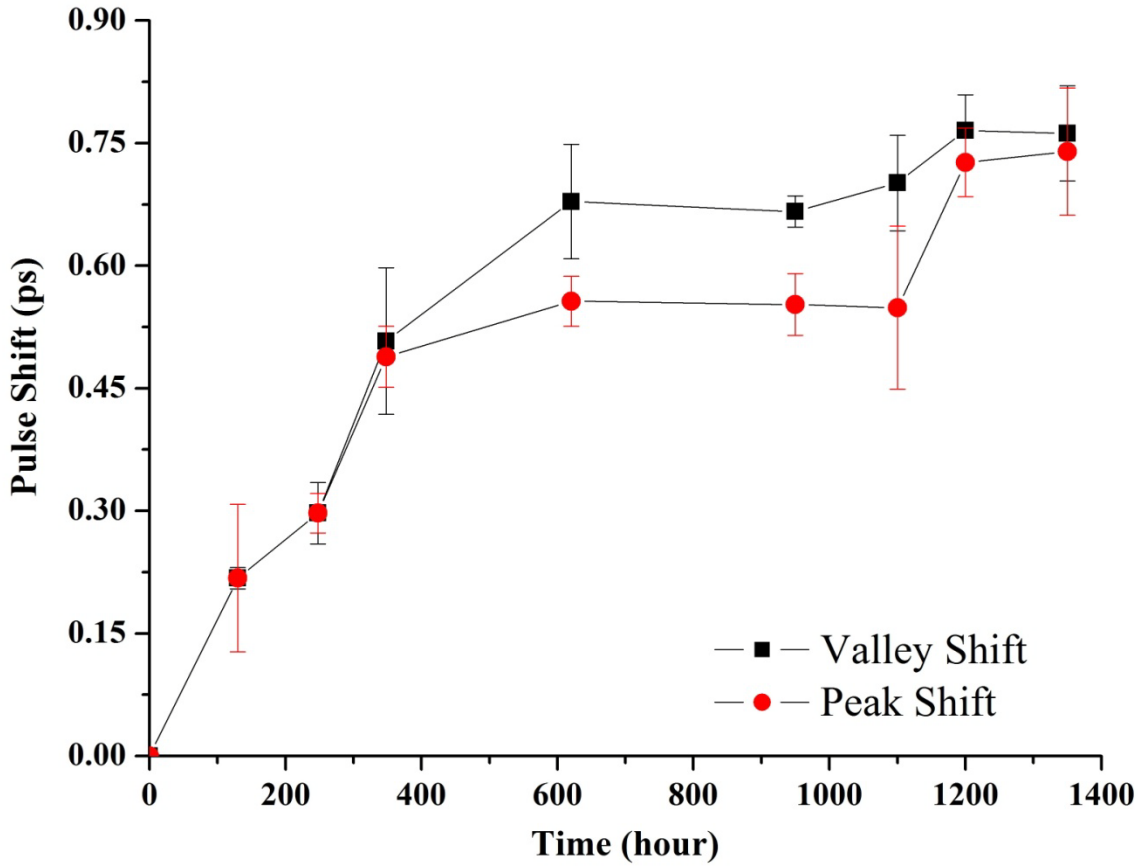

Figure 43 The delay time of the second reflected THz pulse versus the heating time in the furnace.

Finally, Figure 44 compares the average TGO thickness obtained by SEM measurements with the delay time of the reflected THz pulse (negative-peak-to-negative-peak). The delay time of the THz pulse rapidly increased for thermal-exposure times up to 348 hours, and the SEM images confirmed that the TGO thickness was increased from 0 to 5 micrometers within the first 348 hours. The average TGO thickness had increased to 9 micrometers by 1300 hours of exposure, although, the variation of the TGO thickness was much greater than during the first 348 hours. Overall, the trend in the delay time of the THz pulse matches the average TGO thickness obtained from the SEM measurements.

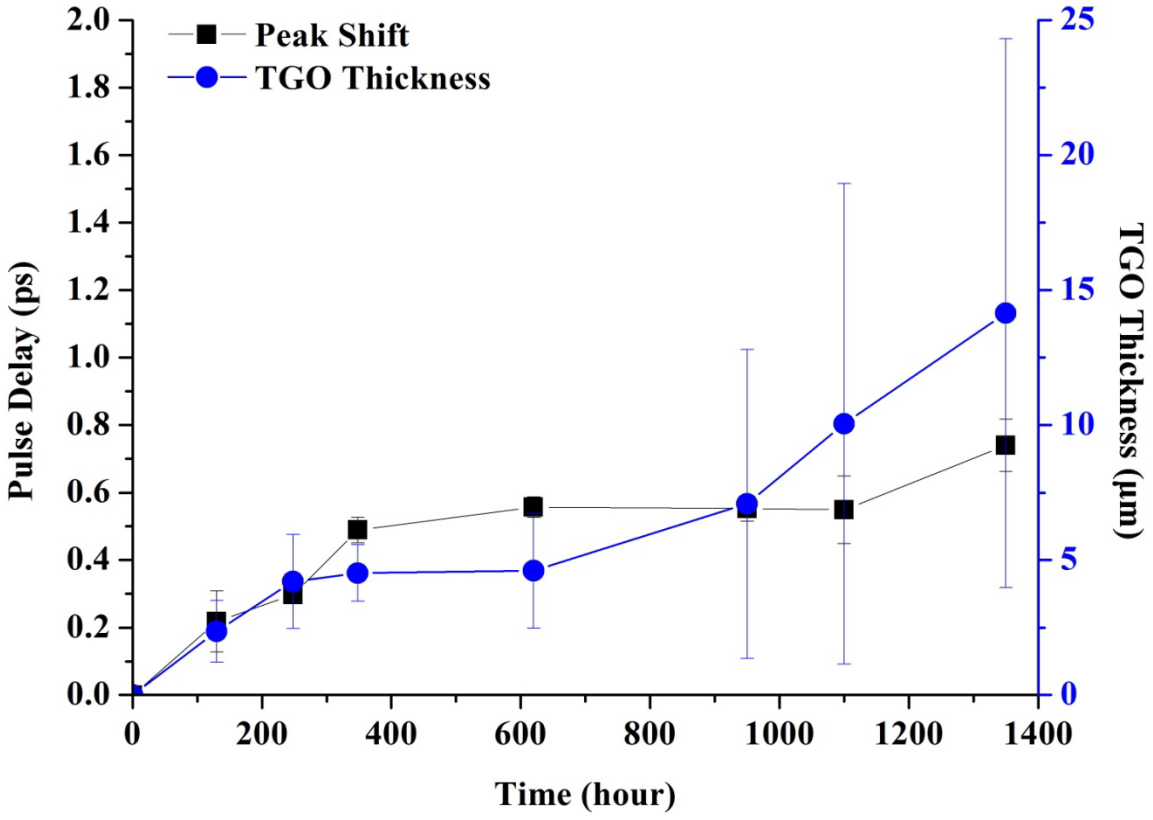

Figure 44 Comparison between average TGO thickness from SEM measurements and the delay time of THz pulse.

Overall, three unique features in the experimental THz time-domain signal can be used to monitor the TBC health condition. First, the increasing delay time of the second reflected THz pulse with respect to the YSZ front-surface reflection corresponds to the

TGO growth. Second, the constant delay time of the second reflected THz pulse indicates that air voids were formed inside the YSZ layer. Third, the broadening of the THz internal-interface reflection and the damped-out oscillation in the tail of this THz pulse suggests a warning that delamination is likely imminent.

5.4 Conclusions

The use of THz-TDR to nondestructively study multilayered, ceramic thermal-protection systems is novel, sensitive, and readily conceivable, although it is still a process that is under development. In this chapter, THz-TDR experimental results have demonstrated the ability to monitor the evolution of thermally-induced oxide layers and voids – embedded at a ceramic/metal interface – that are on the order of a single micrometer in thickness. This was accomplished through the observation of THz pulse time delays and changes in the width and shape of the THz pulses. The experimental data also qualitatively follow Fresnel-reflection-based time-domain simulations of THz pulses in etalons. A comparison with SEM images further shows that the average TGO thickness matches the trend in the delay time of the initial and interface THz pulse reflections. Refinement of the technique presented here could lead to diagnostics that predict the failure of turbine-blade coatings. This would allow TBC replacement to be based on THz assessment rather than on a fixed timetable, although since changes in delay times are analyzed rather than the delay times themselves, the technique will only be effective if a history of pulsed reflectometry measurements is maintained.

Chapter 6
Conclusions

6.1 Summary

Nondestructive evaluation is common in science and industry to evaluate the properties of a material, component or system without causing damage. Because nondestructive evaluation does not permanently alter the DUT being inspected, it is a highly-valuable technique that can save both money and time in product evaluation, troubleshooting, and research. In this thesis, optical nondestructive evaluation tools are developed using a diluted magnetic semiconductor, CMT. A single <110> CMT crystal was employed as a sensing crystal in both microwave and THz electromagnetic wave regions.

This thesis began by describing the physics of the multiple birefringences in a CMT crystal. The induced linear birefringence of a CMT crystal is inherent from its host semiconductor, CdTe, and the induced circular birefringence is generated from the strong exchange interaction between the d spins of the manganese ions and electrons in CMT crystal. Utilizing this multiple birefringence characteristic, CMT can be used to measure the electric field via an EOS technique and the magnetic field via an MOS technique.

In order to demonstrate the potential for using a CMT crystal to make independent measurements of electric and magnetic fields, both theoretical calculation and experimental work were presented. The mathematical representation in the matrix form of a crystal with multiple birefringences was derived from the basic Maxwell equations. Utilizing this matrix, the power transfer functions of the optical probe beam for EO and MO sensing was calculated. The calculated results show that if the linearly polarized incident light is made parallel to one of the CMT principal axes, then CMT measures only magnetic fields. However, if a quarter-waveplate with its slow axis oriented 45 degrees relative to a crossed input polarizer and output analyzer is used, then CMT measures only electric fields. When the polarization of the probe beam is not controlled,

the electromagnetic field pattern measured by CMT becomes a mixture of electric and magnetic effects.

The theoretical calculation was compared to experimental work by measuring the electromagnetic-wave field pattern of a single microstrip transmission line. The experiment started by rotating the linear polarization angle of the incident laser pulses with an optical setup for MO sensing. In this setup, the measured field patterns, which are compared with the reference EO and MO crystals, appear to be a mixture of electric and magnetic field. The comparison proves that the CMT crystal possesses both induced circular and linear birefringence and can be used for independent measurement of both electric and magnetic fields.

After confirming the multiple birefringence characteristic, a noninvasive Poynting vector sensor was developed. A <110>-oriented CMT crystal with a high-reflection coating on one side was employed as a Poynting vector sensor. Proper mounting of the CMT crystal allowed for the measurement of all components of both an electric and a magnetic field. When all of the components of the electric and magnetic field are obtained, the energy flow of an EM wave can be subsequently mapped out based on the definition of the Poynting vector with no transformational calculations. Two different energy flow cases of a 50-Ω microstrip transmission line, an open termination and a matched load, were successfully mapped out. The open-termination case shows no energy flow according to both amplitude and phase information, while the matched load case shows the energy flow along the microstrip transmission line. Refinement of this technique can be used for the near-field measurement of any device that radiates energy.

Besides utilizing CMT in the microwave electromagnetic wave region, CMT is also a suitable EO crystal for THz sensing at low THz frequencies, because it has no phonon resonance below 2 THz. Applying the induced linear birefringence characteristic of CMT, the <110>-oriented CMT crystal was employed as an EO sensing medium in a THz-TDR system to nondestructively study multilayered TBC. The TBC samples have different machined slot widths and varying depths. The narrowest slot width was 50 μm and was resolvable even though it was smaller than the diffraction limit of 1 THz, which is close to the center frequency, 0.8 THz, of the THz pulse. The surface flatness of the TBC can

be examined when a narrow time-domain window at data post processing is selected for the THz reflection at the surface. Moreover, the amplitude of the THz reflection at the surface can be used as an indicator for the slot depth since a deeper depth shows less reflection.

An analysis of the time-domain THz signal can reveal both surface and subsurface defects. THz-TDR experimental results have demonstrated the ability to monitor the evolution of thermally-induced oxide layers and voids – embedded at a ceramic/metal interface – that are on the order of a single micrometer in thickness. This was accomplished through the observation of THz pulse time delays and changes in the width and shape of the THz pulses. The experimental data also qualitatively follow Fresnel-reflection-based time-domain simulations of THz pulses in etalons. A comparison with SEM images further shows that the average TGO thickness matches the trend in the delay time of the initial and interface THz pulse reflections. Refinement of the technique presented here could lead to diagnostics that predict the failure of TBCs. This would allow TBC replacement to be based on THz assessment rather than on a fixed timetable, which not only conserve significant resources for the government and the airlines, but also prevent tragedy caused by delamination and engine failure.

6.2 Future work

Fiber-based EO and MO probes have been used to accomplish microwave electric and magnetic field mapping over the last decade. [74, 75] On the other hand, most THz experiments that have used EOS or MOS detection techniques were still conducted in free space. Therefore, building a fiber-based probe with a <110>-oriented CMT can achieve on-site nondestructive evaluation of TBC systems, as well as measurement of the Poynting vector of electronic devices.

In practice, nonlinear crystals are dispersive at both optical and THz frequencies: the refractive index $n(\omega)$ is a function of frequency. As a result, the group velocity differs from the phase velocity at most frequencies. Consequently, velocity matching in a dispersive medium can be achieved only for a certain THz frequency when the optical-pulse envelope travels at the phase velocity of the monochromatic THz wave. The optimal velocity-matching condition for a broadband THz pulse occurs when the group

velocity of the optical probe pulse is the same as the phase velocity at the central frequency of the THz spectrum. If the product of the sensing crystal thickness and group velocity mismatch between optical probe pulse and THz beam is comparable or longer than the THz pulse duration, the EO signal will have a time-averaging effect. Therefore, if the optical beam is at 800-nm wavelength, different crystals need to have different thicknesses in order to improve the velocity-mismatching condition and hence increase the detection sensitivity and temporal resolution.

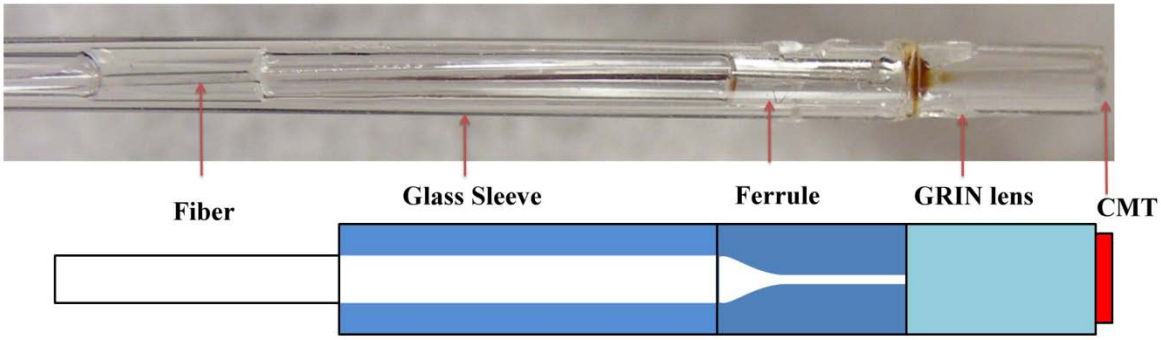

Figure 45 Proposed fiber-based EO/MO probe.

Figure 45 shows a proposed fiber-based probe structure for use in a THz reflectometry imaging system. A single mode fiber will first be inserted into a glass sleeve to produce a rigid support during the scanning. A ferrule will be attached at the end of the glass sleeve to protect the bare fiber and to maintain the optical alignment. The guided probe beam diameter is then expanded to increase the interaction area with the measured fields by using a quarter pitch GRIN lens. At the output of the GRIN lens, the collimated probe beam will be transmitted into the EO/MO crystal and then reflected back into the system by a high reflection coating on the output side of the crystal surface. The polarization-control elements in Figure 1 may also be converted into fiber-based components in order to streamline the system and make it more stable. The dispersion in the fiber is expected to have a relatively small effect on the laser pulse width here, because the SMF will be shorter than 2 meters. If the fiber dispersion severely degrades the optical signal, a prism or grating-based dispersion-compensation optical network at the input to the fiber will be implemented.

Bibliography

1. C.-C. Chen, D.-J. Lee, T. Pollock, and J. F. Whitaker, "Pulsed-terahertz reflectometry for health monitoring of ceramic thermal barrier coatings," Opt. Express 18, 3477-3486.
2. K. Yang, G. David, S. V. Robertson, J. F. Whitaker, and L. P. B. Katehi, "Electrooptic mapping of near-field distributions in integrated microwave circuits," Microwave Theory and Techniques, IEEE Transactions on 46, 2338-2343 (1998).
3. Y. Kyoung, G. David, Y. Jong-Gwan, I. Papapolymerou, L. P. B. Katehi, and J. F. Whitaker, "Electrooptic mapping and finite-element modeling of the near-field pattern of a microstrip patch antenna," Microwave Theory and Techniques, IEEE Transactions on 48, 288-294 (2000).
4. N. S. H. Togo, and T. Nagatsuma "Near-Field Mapping System Using Fiber-Based Electro-Optic Probe for Specific Absorption Rate Measurement " IEICE Trans. Electron E90-C 436-442 (2007).
5. R. M. Reano, Y. Kyoung, L. P. B. Katehi, and J. F. Whitaker, "Simultaneous measurements of electric and thermal fields utilizing an electrooptic semiconductor probe," Microwave Theory and Techniques, IEEE Transactions on 49, 2523-2531 (2001).
6. S. Wakana, T. Ohara, M. Abe, E. Yamazaki, M. Kishi, and M. Tsuchiya, "Fiber-edge electrooptic/magnetooptic probe for spectral-domain analysis of electromagnetic field," Microwave Theory and Techniques, IEEE Transactions on 48, 2611-2616 (2000).
7. K. Yang, T. Marshall, M. Forman, J. Hubert, L. Mirth, Z. Popovic, L. P. B. Katehi, and J. F. Whitaker, "Active-amplifier-array diagnostics using high-resolution electrooptic field mapping," Microwave Theory and Techniques, IEEE Transactions on 49, 849-857 (2001).
8. J. A. Riordan, F. G. Sun, Z. G. Lu, and X. C. Zhang, "Free-space transient magneto-optic sampling," Applied Physics Letters 71, 1452-1454 (1997).
9. A. Y. Elezzabi, and M. R. Freeman, "Ultrafast magneto-optic sampling of picosecond current pulses," Applied Physics Letters 68, 3546-3548 (1996).

10. J. Valdmanis, and G. Mourou, "Subpicosecond electrooptic sampling: Principles and applications," Quantum Electronics, IEEE Journal of 22, 69-78 (1986).
11. J. Valdmanis, G. Mourou, and C. Gabel, "Subpicosecond electrical sampling," Quantum Electronics, IEEE Journal of 19, 664-667 (1983).
12. Z. Jiang, F. G. Sun, Q. Chen, and X.-C. Zhang, "Electro-optic sampling near zero optical transmission point," Applied Physics Letters 74, 1191-1193 (1999).
13. P. U. Jepsen, C. Winnewisser, M. Schall, V. Schyja, S. R. Keiding, and H. Helm, "Detection of THz pulses by phase retardation in lithium tantalate," Physical Review E 53, R3052 (1996).
14. J. A. Valdmanis, and G. Mourou, "Subpicosecond electrooptic sampling: principles and applications," IEEE J. Quant. Electron. ; Vol/Issue: QE-22:1, Pages: vp (1986).
15. P. C. M. Planken, H.-K. Nienhuys, H. J. Bakker, and T. Wenckebach, "Measurement and calculation of the orientation dependence of terahertz pulse detection in ZnTe," J. Opt. Soc. Am. B 18, 313-317 (2001).
16. E. Bocchi, A. Milani, A. Zappettini, S. M. Pietralunga, and M. Martinelli, "Determination of ionic and pure electronic contributions to the electro-optic coefficient of cadmium telluride and gallium arsenide single crystals," Synthetic Metals 124, 257-259 (2001).
17. J. E. Kiefer, and A. Yariv, "Electro-optic characteristic of CdTe at 3.39 and 10.6 mu," Applied Physics Letters 15, 26-27 (1969).
18. G. Babonas, R. R. Galazka, G. Pukinskas, and A. Scaronileika, "Crystal Structure and Magnetooptical Properties of $Cd_{1-x}Mn_xTe$ with High Mn Concentrations," physica status solidi (b) 154, 389-395 (1989).
19. D. G. Thomas, "Excitons and Band Splitting Produced by Uniaxial Stress in CdTe," Journal of Applied Physics 32, 2298-2304 (1961).
20. P. B. Dayal, B. R. Mehta, and P. D. Paulson, "Spin-orbit splitting and critical point energy at Gamma and L points of cubic CdTe nanoparticles: Effect of size and nonspherical shape," Physical Review B 72, 115413 (2005).
21. V. Zayets, M. C. Debnath, and K. Ando, "Complete magneto-optical waveguide mode conversion in $Cd_{1-x}Mn_xTe$ waveguide on GaAs substrate," Applied Physics Letters 84, 565-567 (2004).

22. J. K. Furdyna, and N. Samarth, "Magnetic properties of diluted magnetic semiconductors: A review (invited)," Journal of Applied Physics 61, 3526-3531 (1987).
23. R. G. Wheeler, and J. O. Dimmock, "Exciton Structure and Zeeman Effects in Cadmium Selenide," Physical Review 125, 1805 (1962).
24. K. Ando, H. Saito, V. Zayets, and M. C. Debnath, "Optical properties and functions of dilute magnetic semiconductors," Journal of Physics: Condensed Matter 16, S5541-S5548 (2004).
25. B. Krichevtsov, "Anisotropy of the linear and quadratic magnetic birefringence in rare-earth semiconductors (γ-Ln2S3 (Ln=Dy^{3+}, Pr^{3+}, Gd^{3+}, La^{3+})," Journal of Experimental and Theoretical Physics 92, 830-839 (2001).
26. P. S. Pershan, "Magneto-Optical Effects," Journal of Applied Physics 38, 1482-1490 (1967).
27. A. Y. P. Yeh, "Optical waves in crystals," John Wiley & Sons, Inc (1984).
28. K. S. Lee, "New compensation method for bulk optical sensors with multiple birefringences," Applied Optics 28, 2001 (1989).
29. R. Rey-de-Castro, D. Wang, X. Zheng, A. Verevkin, R. Sobolewski, M. Mikulics, R. Adam, P. Kordos, and A. Mycielski, "Subpicosecond Faraday effect in $Cd_{1-x}Mn_xTe$ and its application in magneto-optical sampling," Applied Physics Letters 85, 3806-3808 (2004).
30. N. Fang, and X. Zhang, "Imaging properties of a metamaterial superlens," Applied Physics Letters 82, 161-163 (2003).
31. D. Schurig, J. J. Mock, B. J. Justice, S. A. Cummer, J. B. Pendry, A. F. Starr, and D. R. Smith, "Metamaterial Electromagnetic Cloak at Microwave Frequencies," Science 314, 977-980 (2006).
32. R. S. Schechter, and S. T. Chun, "Large finite-difference time domain simulations of a left-handed metamaterial lens with wires and resonators," Applied Physics Letters 91, 154102 (2007).
33. M. Sigalov, E. O. Kamenetskii, and R. Shavit, "Effective chiral magnetic currents, topological magnetic charges, and microwave vortices in a cavity with an enclosed ferrite disk," Physics Letters A 372, 91-97 (2008).

34. C.-L. Zou, Y. Yang, Y.-F. Xiao, C.-H. Dong, Z.-F. Han, and G.-C. Guo, "Accurately calculating high quality factor of whispering-gallery modes with boundary element method," J. Opt. Soc. Am. B 26, 2050-2053 (2009).
35. S. Diziain, J. Amet, F. I. Baida, and M.-P. Bernal, "Optical far-field and near-field observations of the strong angular dispersion in a lithium niobate photonic crystal superprism designed for double (passive and active) demultiplexer applications," Applied Physics Letters 93, 261103 (2008).
36. F. Sumiyoshi, A. Kawagoe, M. Tokuda, and S. Kaminohara, "A Quench Monitoring System of Superconducting Coils by Using the Poynting Vector Method," Applied Superconductivity, IEEE Transactions on 19, 2341-2344 (2009).
37. M. A. Seo, A. J. L. Adam, J. H. Kang, J. W. Lee, S. C. Jeoung, Q. H. Park, P. C. M. Planken, and D. S. Kim, "Fourier-transform terahertz near-field imaging of one-dimensional slit arrays: mapping of electric-field-, magnetic-field-, and Poynting vectors," Opt. Express 15, 11781-11789 (2007).
38. H. Hirayama, H. Kondo, N. Kikuma, and K. Sakakibara, "Visualization of emission from bend of a transmission line with Poynting vector and wave-number vector," in Electromagnetic Compatibility - EMC Europe, 2008 International Symposium on(2008), pp. 1-4.
39. E. Suzuki, S. Arakawa, M. Takahashi, H. Ota, K. I. Arai, and R. Sato, "Visualization of Poynting Vectors by Using Electro-Optic Probes for Electromagnetic Fields," Instrumentation and Measurement, IEEE Transactions on 57, 1014-1022 (2008).
40. C.-C. Chen, and J. F. Whitaker, "Combined nonlinear-optical electric and magnetic field response in a cadmium manganese telluride crystal," Applied Physics Letters 92, 101119-101113 (2008).
41. D. K. Cheng, "Field and Wave Electromagnetics, 2nd Edition," (1989).
42. Q. Zhan, "Magnetic field distribution of a highly focused radially-polarized light beam: comment," Opt. Express 18, 765-766 (2010).
43. R. A. Cheville, M. T. Reiten, J. O'Hara, and D. R. Grischkowsky, "THz time domain sensing and imaging," R. J. Hwu, and L. W. Dwight, eds. (SPIE, 2004), pp. 196-206.
44. D. M. Mittleman, R. H. Jacobsen, and M. C. Nuss, "T-ray imaging," Selected Topics in Quantum Electronics, IEEE Journal of 2, 679-692 (1996).

45. L. Duvillaret, F. Garet, and J.-L. Coutaz, "Highly Precise Determination of Optical Constants and Sample Thickness in Terahertz Time-Domain Spectroscopy," Appl. Opt. 38, 409-415 (1999).
46. T. Yasui, T. Yasuda, K.-i. Sawanaka, and T. Araki, "Terahertz paintmeter for noncontact monitoring of thickness and drying progress in paint film," Appl. Opt. 44, 6849-6856 (2005).
47. D. L. Woolard, R. Brown, M. Pepper, and M. Kemp, "Terahertz Frequency Sensing and Imaging: A Time of Reckoning Future Applications?," Proceedings of the IEEE 93, 1722-1743 (2005).
48. E. Pickwell, and V. P. Wallace, "Biomedical applications of terahertz technology," Journal of Physics D: Applied Physics 39, R301 (2006).
49. J. F. Federici, B. Schulkin, F. Huang, D. Gary, R. Barat, F. Oliveira, and D. Zimdars, "THz imaging and sensing for security applications—explosives, weapons and drugs," Semiconductor Science and Technology 20, S266-S280 (2005).
50. J. A. Zeitler, P. F. Taday, D. A. Newnham, M. Pepper, K. C. Gordon, and T. Rades, "Terahertz pulsed spectroscopy and imaging in the pharmaceutical setting a review," Journal of Pharmacy and Pharmacology 59, 209-223 (2007).
51. A. J. Fitzgerald, B. E. Cole, and P. F. Taday, "Nondestructive analysis of tablet coating thicknesses using terahertz pulsed imaging," Journal of Pharmaceutical Sciences 94, 177-183 (2005).
52. Y.-C. Shen, P. F. Taday, D. A. Newnham, M. C. Kemp, and M. Pepper, "3D chemical mapping using terahertz pulsed imaging," R. J. Hwu, and J. L. Kurt, eds. (SPIE, 2005), pp. 24-31.
53. V. P. Wallace, A. J. Fitzgerald, S. Shankar, N. Flanagan, R. Pye, J. Cluff, and D. D. Arnone, "Terahertz pulsed imaging of basal cell carcinoma ex vivo and in vivo," British Journal of Dermatology 151, 424-432 (2004).
54. C. M. Ciesla, D. D. Arnone, A. Corchia, D. A. Crawley, C. Longbottom, E. H. Linfield, and M. Pepper, "Biomedical applications of terahertz pulse imaging," N. Joseph, and K. R. Murray, eds. (SPIE, 2000), pp. 73-81.

55. A. Rice, Y. Jin, X. F. Ma, X.-C. Zhang, D. Bliss, J. Larkin, and M. Alexander, "Terahertz optical rectification from <110> zinc-blende crystals," Applied Physics Letters 64, 1324-1326 (1994).
56. H. Hamster, A. Sullivan, S. Gordon, W. White, and R. W. Falcone, "Subpicosecond, electromagnetic pulses from intense laser-plasma interaction," Physical Review Letters 71, 2725 (1993).
57. T. Bartel, P. Gaal, K. Reimann, M. Woerner, and T. Elsaesser, "Generation of single-cycle THz transients with high electric-field amplitudes," Opt. Lett. 30, 2805-2807 (2005).
58. H. Zhong, N. Karpowicz, and X.-C. Zhang, "Terahertz emission profile from laser-induced air plasma," Applied Physics Letters 88, 261103 (2006).
59. Z. Piao, M. Tani, and K. Sakai, "Carrier Dynamics and Terahertz Radiation in Photoconductive Antennas," Japanese Journal of Applied Physics 39, 96-100 (2000).
60. T. Masahiko, and et al., "Generation and detection of terahertz pulsed radiation with photoconductive antennas and its application to imaging," Measurement Science and Technology 13, 1739 (2002).
61. A. Dreyhaupt, S. Winnerl, T. Dekorsy, and M. Helm, "High-intensity terahertz radiation from a microstructured large-area photoconductor," Applied Physics Letters 86, 121114 (2005).
62. C. Winnewisser, P. U. Jepsen, M. Schall, V. Schyja, and H. Helm, "Electro-optic detection of THz radiation in $LiTaO_3$, $LiNbO_3$ and ZnTe," Applied Physics Letters 70, 3069-3071 (1997).
63. J. A. Riordan, F. G. Sun, Z. G. Lu, and X.-C. Zhang, "Free-space transient magneto-optic sampling," Applied Physics Letters 71, 1452-1454 (1997).
64. O. Trunova, T. Beck, R. Herzog, R. W. Steinbrech, and L. Singheiser, "Damage mechanisms and lifetime behavior of plasma sprayed thermal barrier coating systems for gas turbines--Part I: Experiments," Surface and Coatings Technology 202, 5027-5032 (2008).
65. V. K. Tolpygo, and D. R. Clarke, "The effect of oxidation pre-treatment on the cyclic life of EB-PVD thermal barrier coatings with platinum-aluminide bond coats," Surface and Coatings Technology 200, 1276-1281 (2005).

66. S. R. Choi, D. Zhu, and R. A. Miller, "Database of Plasma-Sprayed ZrO_2-8wt% Y_2O_3 Thermal Barrier Coatings," The International Journal of Applied Ceramic Technology 1, 330-342 (2004).
67. M. Y. He, J. W. Hutchinson, and A. G. Evans, "Simulation of stresses and delamination in a plasma-sprayed thermal barrier system upon thermal cycling," Materials Science and Engineering A 345, 172-178 (2003).
68. W. A. Ellingson, R. J. Visher, R. S. Lipanovich, and C. M. Deemer, "Optical NDT Methods for Ceramic Thermal Barrier Coatings," Materials Evaluation 64, 45-51 (2006).
69. S. Song, and P. Xiao, "An impedance spectroscopy study of high-temperature oxidation of thermal barrier coatings," Materials Science and Engineering B 97, 46-53 (2003).
70. K. W. Schlichting, K. Vaidyanathan, Y. H. Sohn, E. H. Jordan, M. Gell, and N. P. Padture, "Application of Cr^{3+} photoluminescence piezo-spectroscopy to plasma-sprayed thermal barrier coatings for residual stress measurement," Materials Science and Engineering A 291, 68-77 (2000).
71. L. Hess, and R. A. Cheville, "Nondestructive evaluation of ceramic bearings using THz impulse ranging," in Lasers and Electro-Optics, 2004. (CLEO), p. 2 pp. vol.1.
72. J. I. Eldridge, and T. J. Bencic, "Monitoring delamination of plasma-sprayed thermal barrier coatings by reflectance-enhanced luminescence," Surface and Coatings Technology 201, 3926-3930 (2006).
73. N. Matsumoto, T. Nakagawa, A. Ando, Y. Sakabe, S. Kirihara, and Y. Miyamoto, "Study of Multilayer Ceramic Photonic Crystals in THz Region," Japanese Journal of Applied Physics 44, 7111 (2005).
74. F. Cecelja, and W. Balachandran, "Electrooptic sensor for near-field measurement," Instrumentation and Measurement, IEEE Transactions on 48, 650-653 (1999).
75. S. Wakana, E. Yamazaki, S. Mitani, H. Park, M. Iwanami, S. Hoshino, M. Kishi, and M. Tsuchiya, "Performance evaluation of fiber-edge magnetooptic probe," Lightwave Technology, Journal of 21, 3292-3299 (2003).